UNIVERSITÀ DEGLI STUDI DI PADOVA

FACOLTÀ DI SCIENZE MM. FF. NN.
DIPARTIMENTO DI SCIENZE CHIMICHE

SCUOLA DI DOTTORATO IN SCIENZE MOLECOLARI
INDIRIZZO SCIENZE CHIMICHE
XXIII CICLO

Nanostructured Materials Based on ZnO for Catalytic, Optical and Magnetic Applications

DIRETTORE DELLA SCUOLA: CHIAR.MO PROF. MAURIZIO CASARIN
SUPERVISORE: CHIAR.MO PROF. EUGENIO TONDELLO
CO-SUPERVISORE: DOTT.ESSA LIDIA ARMELAO

DOTTORANDA: LAURA BOVO

TRIENNIO 2008-2010

Abstract

ZnO based materials, such as $Zn_{1-x}TM_xO$ (TM = Mn, Co, Cu) nanopowders, were synthesised by a *Sol gel* route to investigate their properties in three fields: catalysis, optics and magnetism. These materials were characterised by complementary techniques such as *X-ray Diffraction* (XRD)*, Scanning Electron Microscopy* (SEM)*, X-ray Photoelectron Spectroscopy* (XPS) and *UV-Vis Spectroscopy*. The fine structure and electronic properties of these nanomaterials were studied by *X-ray Absorption Spectroscopy* (XAS) and *Electron Paramagnetic Resonance* (EPR). These techniques give site, element and chemical specific measurements which allow a better understanding of the interplay and role of each element in the functionality of the system.

The catalytic performance of undoped and Cu-doped ZnO nanosystems were tested with respect to the *Methanol Steam Reforming* (MSR) reaction. Contrary to what is generally accepted in literature, the results obtained in this study demonstrate that ZnO also plays a prominent role in this catalytic process. The structure–activity relationship of ZnO and copper-doped ZnO catalysts described in this work give an insight into the effective function of each component which is vital to enable the rational design of improved catalysts.

The luminescence properties of the doped $Zn_{1-x}TM_xO$ nanopowders were investigated with *X-ray Excited Optical Luminescence* (XEOL) techniques: these experiments provided a better understanding of the relationship between the electronic structure of the systems and their properties. Results showed how it is possible to manipulate the luminescence of ZnO grown by *Sol gel* by modifying synthesis

conditions – i.e. the annealing temperature and the nature and concentration of the transition metal ion.

Finally, preliminary results were presented on the materials' magnetic properties, obtained by SQUID (*Superconducting Quantum Interference Devices*) magnetometry, where the coexistence of different contributions has been detected. Even though further characterisation is still needed, this study is a step towards the determination of the nature of magnetic interactions in such systems, of which there has been considerable debate in the scientific community.

KEYWORDS: ZnO, semiconductor, nanomaterial, nanopowder, ZnO:Mn, ZnO:Co, ZnO:Cu, sol gel synthesis, catalysis, Methanol Steam Reforming (MSR), optical property, luminescence, diluted magnetic semiconductor (DMS), spintronics, magnetism, paramagnetism, ferromagnetism, X-ray Photoelectron Spectroscopy (XPS), Electron Paramagnetic Resonance (EPR), X-ray absorption spectroscopy (XAS), X-ray excited optical luminescence (XEOL), Superconducting Quantum Interference Devices (SQUID).

Abstract

Materiali a base di ZnO, in particolare nano-polveri di $Zn_{1-x}TM_xO$ (TM = Mn, Co, Cu), sono stati sintetizzati via *Sol gel* per studiarne le proprietà in tre diversi campi applicativi quali la catalisi, l'ottica ed il magnetismo. Tali materiali sono stati caratterizzati utilizzando diverse tecniche, complementari tra loro, quali *X-ray Diffraction* (XRD)*, Scanning Electron Microscopy* (SEM)*, X-ray Photoelectron Spectroscopy* (XPS) e *UV-Vis Spectroscopy*. *X-ray Absorption Spectroscopy* (XAS) ed *Electron Paramagnetic Resonance* (EPR) vengono invece impiegate per studiare le proprietà elettroniche e di struttura fine delle nano-polveri. Tali caratterizzazioni si sono dimostrate fondamentali per la comprensione delle proprietà del sistema ed, in particolare, per cercare di identificare le interazioni sussistenti tra struttura, composizione, morfologia dei materiali e la loro capacità di espletare una determinata funzionalità.

Nano-polveri di ZnO tal quali e drogate con ioni rame vengono testate come catalizzatori nella reazione di *Steam Reforming* del metanolo. I risultati ottenuti in questo studio dimostrano il ruolo attivo dell'ossido di zinco nel processo catalitico, contrariamente a quanto solitamente accettato in letteratura. La relazione sussistente tra struttura-attività nei catalizzatori a base di ZnO permette di ottenere informazioni circa l'effettiva funzione di ogni componente, aspetto di estrema importanza per la progettazione razionale di catalizzatori con elevate performance.

Le proprietà di luminescenza dei sistemi drogati $Zn_{1-x}TM_xO$ vengono studiate mediante spettroscopia *X-ray Excited Optical Luminescence* (XEOL); tali esperimenti forniscono una migliore comprensione del rapporto che sussiste tra la struttura elettronica dei sistemi in esame e le loro proprietà di emissione. I risultati mostrano come sia possibile modulare la luminescenza di ZnO prodotto via *Sol gel* modificando

le condizioni di sintesi – i.e. temperatura di trattamento, natura e concentrazione del metallo di transizione utilizzato come drogante.

Infine, risultati preliminari sulle proprietà magnetiche dei materiali ottenuti mediante *SQUID magnetometer* (*Superconducting Quantum Interference Devices*) hanno rivelato la coesistenza di diversi contributi magnetici. Nonostante ulteriori caratterizzazioni siano sicuramente necessarie, questo studio si è rivelato un passo avanti verso una comprensione della natura delle interazioni magnetiche in tali sistemi, da tempo causa di vivace dibattito nella comunità scientifica.

KEYWORDS: ZnO, semiconductor, nanomaterial, nanopowder, ZnO:Mn, ZnO:Co, ZnO:Cu, Sol gel synthesis, catalysis, Methanol Steam Reforming (MSR), optical property, luminescence, Diluted Magnetic Semiconductor (DMS), spintronics, magnetism, paramagnetism, ferromagnetism, X-ray Photoelectron Spectroscopy (XPS), Electron Paramagnetic Resonance (EPR), X-ray Absorption Spectroscopy (XAS), X-ray Excited Optical Luminescence (XEOL), Superconducting Quantum Interference Devices (SQUID).

Co-Authorship Statement

The following thesis contains material resulting from some scientific collaborations with national and international groups; people involved in such teamworks are mentioned below.

Prof. Eugenio Tondello and Dr. Lidia Armelao were responsible for the supervision of Laura Bovo during her Ph.D. studies.

Prof. Gabriel Aeppli and Dr. Yeong-Ah Soh supervised the period of about one year that Laura Bovo spent abroad at the *London Centre of Nanotechnology,* LCN, in London (UK). All the magnetic measurements were performed at the research centre.

The study on the catalytic activity of undoped and Cu-doped ZnO, described in chapter 4, is a result of the collaboration with Prof. Antonella Glisenti and Dr. Marta Maria Natile from the *University of Padua* (IT).

X-ray Absorption Spectroscopy (XAS) and *X-ray Excited Optical Luminescence* (XEOL) results spring from the international cooperation with Prof. Tsun-Kong Sham and Dr. Michael Wayne Murphy from the *University of Western Ontario London*, Ontario, Canada.

Electron Paramagnetic Resonance (EPR) measurements were performed by Dr. Lorenzo Sorace within the collaboration project with the group of Prof. Dante Gatteschi *from the University of Florence* (IT).

Finally, *Scanning Electron Microscopy* (SEM) images were taken by Dr. Chiara Maccato from the *University of Padua* (IT).

Un’era è giunta al termine,
Il quartetto si scioglie: Mi mancherete….

“All meaningful and lasting change starts first in your imagination
and then works its way out.
Imagination is more important than knowledge.„
Albert Einstein

Acknowledgements

Al Prof. Eugenio Tondello, mio supervisore, per aver sempre avuto grande fiducia nelle mie capacità; per aver creduto in me e nel mio lavoro. Senza la sua disponibilità ed il suo appoggio la "persona di scienza" che sono oggi ed i risultati fin qui da me ottenuti difficilmente si sarebbero realizzati.

Alla Dr.essa Lidia Armelao, credo una delle migliori guide che avessi potuto sperare di incontrare: molto attenta, sempre presente ma allo stesso tempo discreta. Ha saputo fidarsi della mia indipendenza, mi ha lasciata camminare "con le mie gambe" con i miei errori e le mie conquiste, ma sempre pronta ad aiutare nel momento del bisogno.

Al Dr. Gregorio Bottaro, perché che so che su di lui semplicemente posso sempre contare, sia sul lavoro che davanti ad una bella pinta di birra.

It has been a year now since I first moved to London and, to be honest, this city has changed my life…

It has been an honour to work with Prof. Gabriel Aeppli and Dr. Yeong-Ah Soh and I really want to thank them both for welcoming in their group. Their enthusiasm and passion for this work have really inspired me. Under their guidance I've learnt so much and lots of new prospects have opened up.

I also want to thank all co-authors that have in some way collaborated towards the completion of this project: your contributions have been vital in bringing about the results that we have achieved.

Last, to who helped me the most during the editing and the revising of this thesis I just want to say: GRAZIE, for everything….

Contents

Abbreviations and Symbols

β_e	Electronic Bohr magneton
β_{hkl}	Full width at half maximum (FWHM) of the diffraction peak
β_N	Nucleus Bohr magneton
γ_N	Nuclear gyromagnetic ratio
Δ_{SO}	Spin-Orbit Splitting
θ	Incident angle
Θ	Weiss constant
Φ	Average size of crystallites
λ	Wavelength
ν	Frequency
μ	Magnetic moment

χ	Susceptibility
ψ_I	Wave function
3D	Three Dimensional
2D	Two Dimensional
1D	One Dimensional
A	Hyperfine tensor
APS	Advanced Photon Source
$B_S(x)$	Brillouin function
BE	Binding Energy
BET	Acronym for Brunauer, Emmett and Teller, theory of gas adsorption on solid surfaces
BM	Bending Magnet
BSE	Back Scattering Electron
c	Speed of light
C	Curie constant
CA	Citric Acid
CB	Conducting Band
CLS	Canadian Light Source

d_{hkl}	Spacing between atomic planes
DC	Direct Current
DMS	Diluted Magnetic Semiconductor
DOSs	Densities Of States
EPR	Electron Paramagnetic Resonance
ESCA	Electron Spectroscopy for Chemical Analysis
ESR	Electron Spin Resonance
EXAFS	Extended X-ray Absorption Fine Structure
FE-SEM	Field Emission-Scanning Electron Microscopy
FLY	Fluorescent Yield
FM	Ferromagnetism
FTIR	Fourier Transform Infrared Spectroscope
FWHM	Full Width at Half Maximum
H	Applied magnetic field
hcp	Hexagonal close packing
hkl	Miller's indices for the single reflection
$h\nu$	Photon Energy

Hc	Coercitive field
ICSD	Inorganic Crystal Structure Database
IR	Infra Red
J	Exchange Integral, its sign defined the nature of the magnetic interaction between spins
JCPDS	Joint Committee on Powder Diffraction Standards
$\boldsymbol{K_B}$	*Boltzmann's constant*
KE	Kinetic Energy
$\mathbf{m_e}$	Electron mass
$\boldsymbol{m_N}$	Nucleus mass
M	Magnetisation
$\boldsymbol{M_R}$	Remanence
$\boldsymbol{M_S}$	Saturation magnetisation
MAUD	Material Analysis Using Diffraction
MS	Magnetometer-Susceptometer
MSR	Methanol Steam Reforming
$\boldsymbol{N_J}$	Population of the J^{th} state
NEXAF	Near-Edge X-ray Absorption Fine Structure

NRTL	Non-Random Two Liquid
ODMR	Optically Detected Magnetic Resonance
PEM	Polymer Electrolyte Membrane
PhD	Doctor of Philosophy **(**from the latin *Philosophiae Doctor*)
PL	Photo Luminescence
PNC-XOR	Pacific Northwest Consortium X-ray Operation Research
QMS	Quadrupole Mass Spectrometer
RSO	Reciprocating Sample Option
S	Angular spin momentum
SE	Secondary Electron
SEM	Scanning Electron Microscopy
SGM	Spherical Grating Monochromator
SN_2	Bimolecular Nucleophilic Substitution
SSA	Specific Surface Area
SQUID	Superconducting Quantum Interference Devices
T_C	Curie temperature
TEY	Total Electron Yield

TM	Transition Metal
UV	Ultra Violet
V_O	Oxygen Vacancy
V_{Zn}	Zinc Vacancy
VB	Valence Band
Vis	Visible
XANES	X-ray Absorption Near-Edge Structure
XAS	X-ray Absorption Spectroscopy
XEOL	X-ray Excited Optical Luminescence
XMCD	X-ray Magnetic Circular Dichroism
XPS	X-ray Photoelectron Spectroscopy
XRD	X-ray Diffraction
WHSV	Weight Hourly Space Velocity

Chapter 1
Introduction

1.1 Objective of the Thesis

Among inorganic materials, metal oxides such as ZnO play a fundamental role in developing new devices as they present a considerable variety of structures, stoichiometries and chemical and physical properties that can be tailored to exploit a variety of suitable synthesis techniques. A wide range of possible optical, catalytic, magnetic and electrical properties[1] can be designed into innovative functional systems thanks to the ability to manipulate their nano-scale structure[2].

Zinc oxide, an important II-IV semiconductor with direct band gap (3.2 eV[3-5]) and large exciton binding energy (60 meV[3-5]), has become one of the most attractive materials in research due to its wide application in fields ranging from optoelectronics[6], (photo)- catalysis[7-10] and optics[11,12] to biology[13,14] together with its uncommon properties of good stability, bio-compatibility and non-toxicity. Due to its wide spectrum of outstanding properties, ZnO is one of the most important and versatile functional materials; moreover its properties can be easily tailored by adding appropriate dopants[3-5].

Great progress has been made in synthesis methods and device applications of ZnO nanostructures[3-5,15], however there are still unanswered questions concerning fundamental properties of this material, in particular those related to defects, visible emissions and magnetic properties. In spite of many decades of investigation even some of the basic properties of ZnO still remain unclear. There are three fields in which scientific debate is particularly lively: catalysis, optics and magnetism.

Concerning the field of catalysis, the lack of agreement arises from the fact that similar catalysts prepared through different routes can present distinct catalytic properties[9-10,16-21]. Nowadays hydrogen production via catalytic steam reforming of alcohols is one of the most promising and suitable technologies. Copper-based ZnO catalysts are those most commonly used for the *Methanol Steam Reforming* reaction (MSR) due to their high activity and selectivity[9-10,16-21]. The MSR reaction mechanism with Cu-based ZnO catalysts has been discussed at length in the literature. Several mechanisms have been proposed, but there is little agreement about which is the most accurate[9-10,16-21]. One of the biggest controversies concerning these types of systems is the proper ascription of the role of the individual components of the catalyst and the mechanism that underlies the function of these materials. A detailed knowledge of the relationships between catalytic activity and surface and bulk structure is required to prepare new and improved catalysts utilising a knowledge-based (rational) catalyst design process. Unfortunately, for the majority of heterogeneous catalysts the required structure–activity relationships are not sufficiently well known.

Turning ones attention to the optical properties, despite the fact that ZnO is very promising for many applications, there is no general agreement over which of the intrinsic and extrinsic point defects are responsible for the radiative properties of this material[3-5,22-24]. A required consensus is currently lacking of the origin of the well-known green band in the ZnO luminescence spectra occurring as a broad peak around 500–530 nm, observed in nearly all samples regardless of growth conditions[3-5,22-24]. Many different hypotheses have been proposed to explain the visible emission of ZnO[3,5,22-24]: typically this assignment is based on the agreement between theoretical calculations and emission band positions, but in general this is not sufficient to conclusively make such a claim, especially since different calculations differ in their predictions[25-27].

Finally, the II-VI *Diluted Magnetic Semiconductors* (DMS) have attracted considerable attention because the spin-dependent magnetic phenomena can be manipulated in these low-dimensional tailored magnetic nanosystems for various spin-based devices to achieve unprecedented capabilities[28]. Recent theoretical calculations[29-31] have predicted that transition metal ion (TM) doped ZnO is one of the most promising candidates for room-temperature ferromagnetism. These theoretical predictions started an experimental race which soon revealed that some TM-doped ZnO systems exhibited room temperature ferromagnetism although the exact origin and mechanism of the

ferromagnetic (FM) ordering is still disputed[3,4]. Moreover, other magnetic behaviours have been detected in these systems, such as paramagnetism or antiferromagnetic coupling. In short, the origin of magnetic properties in diluted magnetic semiconductors, such as TM-doped ZnO, is not yet clear. Part of this controversy could stem from the lack of detailed micro-structural characterisation, i.e., whether the resulting material is indeed an alloy of transition metal elements within the host material or whether it remains as the matrix material with clusters, precipitates or second phases that are responsible for the observed magnetic properties.

For the reasons discussed so far, this PhD thesis mainly covers the development and optimisation of *Sol gel* synthesis to obtain $Zn_{1-x}TM_xO$ (TM = Mn, Co, Cu) nanostructures, in particular nanopowders, for catalytic, optical and magnetic applications. An extended characterisation with complementary techniques was then undertaken to study the composition, structure and morphology of these systems as well as to determine their local geometry and electronic properties. Finally, other properties of TM-doped ZnO were investigated in order to understand the structure-property relationships in these systems. The optical luminescence and magnetic behaviour of $Zn_{1-x}TM_xO$ (TM = Mn, Co, Cu) were examined and the catalytic performance of undoped ZnO together with $Zn_{1-x}Cu_xO$ systems was tested with respect to the *Methanol Steam Reforming* reaction.

1.2 Arrangement of the Thesis

As mentioned in the previous section, there are three main objectives in this thesis. First, to synthesise II-VI semiconducting nanostructures, specifically, ZnO nanoparticles doped with transition metal ions (TM) such as manganese (Mn), cobalt (Co) and copper (Cu).

The second is to characterise the composition, size, crystal structure, and morphology of these nanostructures with complementary conventional techniques such as *X-ray Diffraction* (XRD), *Scanning Electron Microscopy* (SEM), *X-ray Photoelectron Spectroscopy* (XPS) and UV-Vis spectroscopy. Also, to study the fine structure – i.e. the local geometry – and the electronic structure using *X-ray Absorption Spectroscopy* (XAS) and *Electron Paramagnetic Resonance* (EPR).

The third is to examine different properties of $Zn_{1-x}TM_xO$ (TM = Mn, Co, Cu) systems: in particular their optical and magnetic properties have been studied. Furthermore, the reactivity towards the *Methanol Steam Reforming* reaction (MRS) of undoped and Cu-doped ZnO has been investigated.

The information collected by carrying out these objectives will hopefully provide an insight into how to manipulate and modify the physical, chemical, catalytic, optical and magnetic properties of $Zn_{1-x}TM_xO$ (TM = Mn, Co, Cu) nanostructures for future device applications.

The layout of this thesis is as follows. Chapter 1 provides a brief description of the reasons that led to the realisation of this project. Chapter 2 will describe the synthesis and standard characterisation of $Zn_{1-x}TM_xO$ (TM = Mn, Co, Cu) nanopowders. Chapter 3 will examine the XAS and EPR results of the samples. Chapter 4 will discuss the catalytic activity towards MSR of the undoped and Cu-doped ZnO. Chapter 5 and 6 will describe, respectively, the optical and the magnetic properties of $Zn_{1-x}TM_xO$ (TM = Mn, Co, Cu). Finally, Chapter 7 will summarise the general conclusions of the thesis and future works which may be undertaken.

References:

[1] V.E. Henrich, P.A. Cox, *The Surface Science of Metal Oxides*, Cambridge University Press, Cambridge, UK, (1994)

[2] K.E. Drexler, *Nanosystems: Molecular, Machinery, Manufacturing and Computation* J. Wiley & Sons, New York, (1992)

[3] C. Jagadish, S.J. Pearton *Zinc Oxide Bulk, Thin Film and Nanostructures*, Eds. Elsevier, Amsterdam (2006)

[4] H. Morkoc, U. Ozgur, *Zinc Oxide: Fundamentals, Materials and Devices Technology*, WHILEY-VCH, Verlag GmbH & Co. KGaA Weinheim (2009)

[5] A.B. Djurisˇic', A.M.C. Ng, X.Y. Chen, *Progress in Quantum Electronics* **34** (2010) 191

[6] J.C. Johnson H. Yan, R.D. Schaller, L.H. Haber, R.J. Saykally, P. Yang, *Phys. Chem. B* **105** (2001) 11387

[7] M.R. Hoffman, S.T. Martin, W. Choi, D.W. Bahneman, *Chem. Rev.* **95** (1995) 69

[8] O. Legrini, E. Oliveros, A.M. Braun, *Chem. Rev.* **93** (1993) 671

[9] K. Kähler, M.C. Holz, M. Rohe, J. Strunk, M. Muhler, *Chem. Phys. Chem.* **11** (12) (2010) 2458

[10] S. Sá, H. Silva, L. Brandão, J.M. Sousa, A. Mendes, *Applied Catalysis B: Environmental* **99** (2010) 43

[11] N. Saito, H. Haneda, K. Koumoto, *Adv. Mater.* **14** (2002) 418

[12] J. Liquianga Q. Yichun, W. Baiqi, L. Shudan, J. Baojiang, Y. Libin, F. Wei, F. Honggang, S. Jiazhong, *Solar Energy Materials & Solar Cells* **90** (2006) 1773

[13] A. Dorfan, N. Kumar, J-in Hahm, *Langmuir* **22** (2006) 4890

[14] L. Armelao, M. Pascolini, E. Biasiolo, E. Tondello, G. Bottaro, M. Dalle Carbonare, A. D'Arrigo, A. Leon, *Inorganica Chimica Acta* **361** (2008) 3603

[15] L. Schmidt-Mende, J.L. MacManus-Driscoll, *Materials Today* **10** (5) (2007) 41

[16] J. Papavasiliou, G. Avgouropoulos, T. Ioannides, *Appl. Catal. B* **88** (2009) 490

[17] P. H. Matter, D.J. Braden, U.S. Ozkan *Journal of Catalysis* **223** (2004) 340

[18] J. Agrell, M. Boutonnet, J.L.G. Fierro, *Appl. Catal. A* **253** (2003) 213

[19] S.D. Jones, L.M. Neal, H.E. Hagelin-Weaver, *Appl. Catal. B* **84** (2008) 631

[20] H. Purnama, T. Ressler, R.E. Jentoft, H. Soerijanto, R. Schlogl, R. Schomacker, *Appl. Catal. A* **259** (2004) 83

[21] T. Valdes-Solis, G. Marban, A.B. Fuertes, *Catalysis Today* **116** (2006) 354

[22] T.K. Sham, D. Jiang, I. Coulthard, J.W. Lorimer, H.X. Feng, K.H. Tan, S.P. Frigo, R.A. Rosenberg, D.C. Houghton, B. Bryskiewicz, B. *Nature **363*** (1993) 331

[23] M. Anpo, Y.J. Kubokawa, *J. Phys. Chem.* **88** (1984) 5556

[24] M. Ghosh, A.K. Raychaudhuri, *Nanotechnology* **19** (2008) 445704

[25] C. Richard, A. Catlow, S.A. French, A.A. Sokol, A.A. Al-Sunaidi, S.M. Woodley, *J Comput. Chem.* **29** (2008) 2234

[26] F. Oba, A. Togo, I. Tanaka, J. Paier, G. Kresse, *Phys. Rev. B* **77** (24) (2008) 245202

[27] N.H. Nickel, E. Terukov, *Zinc Oxide—A Material for Micro- and Optoelectronic Applications*, Springer, Dodrecht, The Netherlands (2005) pp 69

[28] C. Weisbuch, B. Vinter, *Quantum Semiconductor Structures Academic*, San Diego, (1991)

[29] T. Dietl, H. Ohno, F. Matsukura, J. Cibert, D. Ferrand, *Science* **287** (2000) 1019

[30] G.A. Prinz *Science* **282** (1998) 1660

[31] H. Dery, P. Dalal, L. Cywinski, L.J. Sham, *Nature* **447** (2007) 573

Chapter 2

$Zn_{1-x}TM_xO$ (TM = Mn, Co, Cu): Sol gel Synthesis and Characterisation

A considerable part of the PhD project was dedicated to the optimisation of the synthetic conditions to obtain nanopowders with controlled compositions, structure and morphology.

The approach used is *Sol gel* synthesis, a wet-chemical technique which allows the fabrication of materials, typically metal oxides, starting from a chemical solution (or *sol*) that acts as the precursor for an integrated network (or *gel*) of either discrete particles or an extended chained network.

The obtained nanostructured ZnO based powders are then characterised with different techniques to determine the evolution of the system whilst manipulating the synthetic conditions. Doping with transition metal ions, such as manganese, cobalt and copper, also offers an effective method to adjust the electrical, magnetic, and optical properties of zinc oxide.

It is very important to first, accurately establish the characteristics of zinc oxide based materials, to better understand their catalytic, optical or magnetic properties. To define relationships between structure-composition and properties is, in fact, the ultimate goal of this project.

2.1 Introduction

Control over the size and morphology of nanometer- or micrometer-scale ZnO crystals represents a great challenge in realising the design of novel functional devices. This is because the magnetic and electronic properties of ZnO crystals, which determine their practical applications, can be easily modified by varying their size and morphology.

Different methods such as vapor-liquid-solid growth, thermal evaporation, thermal decomposition, electrochemical deposition, and solution-phase processes have been introduced to prepare ZnO nano- or microstructured materials with various morphologies. Among these methods, the solution procedure may be the most simple and effective way to prepare large-scale and well-crystallised materials at a relatively low temperature.

2.1.1 *Sol gel* Method

The *Sol gel* process[1-4], developed in the 70s, is a synthetic technique that has aroused great interest. This is particularly important because it allows the production of ceramic or glassy materials with a low processing temperature, i.e. compared with conventional methods such as melting[1,5].

The most common materials synthesised by *Sol gel* are single or multi component oxides. It is also possible to tailor the dimensionality of the final materials on going from bulk to nanostructured systems, forming nanopowders (3D), nanorods (1D) or thin films (2D). In more recent years, procedures to obtain other ceramic materials such as nitrides, hybrid materials (organic / inorganic) and materials based on fluorides have been optimised[6].

The starting point, in a typical *Sol gel* process, is the preparation of a precursor solution, generally alkoxides. Due to hydrolysis and condensation reactions, the solution turns first in a *sol*, i.e. a colloidal suspension of particles in a liquid; subsequently, it forms a *gel* consisting of a solid skeleton containing a liquid phase. The *gel* obtained is subjected to a mild heat treatment slightly above room temperature during which, by liquid loss, it is transformed into a *xerogel*. The last stage of the process is an annealing at higher temperature (a few hundred degrees) to consolidate and form the final product.

The *Sol gel* process can be separated in to three main phases: i) preparation of the precursor solution, ii) *gel* formation, iii) densification and formation of the final material.

Regarding the precursor solution, the choice of each component is a crucial step: usually it is formed by one or more molecular precursors, a solvent (usually an alcohol), water, a catalyst (an acid or base) and any additives that can stabilise the precursors towards the hydrolysis such as, for example, chelating agents[7]. Even the order in which reagents are added and their relative ratios can have a remarkable influence. All these parameters need to be optimised carefully for each different system.

Hydrolysis and polycondensation are the reactions which take place in the precursor solution and which form the *gel* (the so called *Sol gel* transition). A scheme of those reactions is reported below[1]:

a) Hydrolysis:

$$\text{M-OR} + H_2O \rightleftharpoons \text{M-OH} + \text{ROH}$$

b) Condensation:

$$\text{M-OX} + X^I\text{-OM} \rightleftharpoons \text{M-O-M} + XOX^I \qquad (X, X^I = H, R)$$

The reactions (a) and (b) are competitive: they are triggered by the composition of precursor solution and they are difficult to study individually. They lead to the formation of a *gel* structure that is an oxo-bridge based polymer, containing some of the solvent and water in the network. The microstructure and morphology of the final material will depend on the relative speed of the two processes as the polymeric chains will grow with different degrees of branching. In addition, for a multi-component based synthesis, changing process conditions can promote the homo-condensation reactions (M-O-M) over hetero-condensation (M-O-M') with predictable consequences on the composition and homogeneity of the final product. This stage is a key step in the synthetic approach because it has the ability to target the system towards the desired characteristics, if well controlled.

The final step in a *Sol gel* process is a more severe heat treatment that, depending on the conditions used, could tailor various properties of the final material such as composition, compactness and whether the structure is amorphous, polycrystalline or a nanocomposite. During the gradual increase of the temperature, from ambient levels to that of densification, several processes occur such as desorption of water and alcohol,

volumetric shrinkage, a decrease of surface area and porosity and possible oxidation or reduction of organic compounds.

A *Sol gel* material before the final consolidating treatment is typically amorphous. Its transformation into a crystalline, glassy or nanostructured system depends not only on the nature of the initial system, but also on the conditions chosen for the annealing process (i.e. temperature, heating and cooling rates and reaction atmosphere).

2.1.1.1 ZnO Synthesised by *Sol gel*

Solution-borne ZnO nanoparticles and their aggregates represent an increasingly popular class of nanomaterials currently explored worldwide in basic structural and applied physical-chemical studies[8-11]. Among the preparation techniques available for these systems, the *Sol gel* route is very attractive for the reasons discussed previously.

In a *Sol gel* synthesis of zinc oxide the reactions must be performed at a high pH to ensure insoluble $Zn(OH)_2$ species do not form (figure 1).

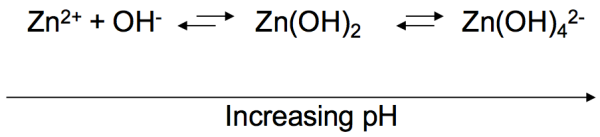

Figure 1: Zn hydroxide species as a function of solution pH.

Zinc alkoxides are very reactive with water, even in the absence of catalysts, due to the presence of highly electronegative OR groups that stabilize the Zn in its 2+ oxidation state[12]. This in turn makes the zinc very susceptible to nucleophilic attack through the SN_2 reaction.

In order to better control and slow down the rate of reaction, anionic "protective" ligands, less susceptible to hydrolysis, are added to the solution. They are usually bi- or poly-dentate chelating ligands, which have a higher binding affinity (to the Zn ions) than the alkoxide or acetate groups, decreasing the chance of a nucleophilic attack.

For the synthesis of single oxide nanoparticles with a unimodal size distribution, which is the aim of this work, precipitation during gelation is not allowed since different phases decompose at different temperatures, resulting in different particle shapes and sizes. The optimal conditions for the gelation process (pH, complexing agents…) and the thermal treatment of the precursor are therefore determined in order to produce

nanosized ZnO particles with a well-controlled particle size and a unimodal size distribution.

Finally, another advantage of an aqueous method, such as *Sol gel*, is the fact that dopants can easily be introduced: this synthesis, in fact, ensures excellent stoichiometric homogeneity throughout the final material.

2.1.2 *X-ray Diffraction*, XRD

X-ray Diffraction (XRD) is based on the coherent elastic scattering that an X-ray photon undergoes due to its interaction with the electrons of the material and the resulting interference patterns between scattered rays.

The simplest and the most common description of X-ray diffraction is undoubtedly the one given by Bragg's model[13]. The phenomenon is described as the selective reflection of monochromatic radiation due to the presence of crystallographic atomic planes, as shown in figure 2.

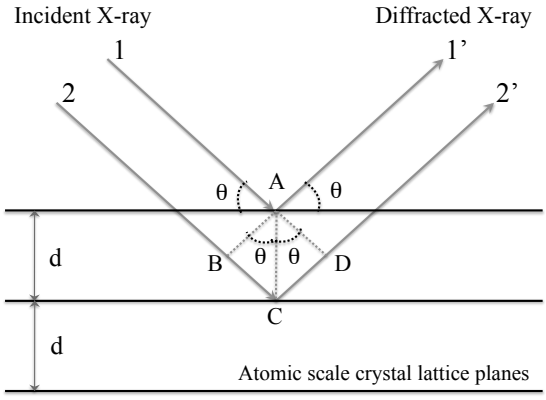

Figure 2: Bragg's law diagram.

The condition for constructive interference of an X-ray photon scattered from parallel atomic planes is described by Bragg's equation:

$$n\lambda = 2d_{hkl} \cdot sen\theta$$

where λ is the wavelength of the incident beam, d_{hkl} is the spacing between atomic planes that generate the reflection (*hkl* are Miller's indices for the single reflection), θ is the incident angle between the X-ray beam and the lattice plane and *n* represents the diffraction order.

During diffraction measurements the sample being analysed (thin film, powder or crystal) is irradiated with a collimated monochromatic X-ray beam; the diffracted rays from the sample are then collected with an appropriate detector. The diffraction signal

can be taken at different incident angles or collected angles, depending on the geometry adopted between source-sample-detector.

The XRD pattern contains all the structural information of a crystalline sample, which can be deduced from the angular position and the intensity of peaks. In particular, the angular position is used to determine the inter-planar distances (*d*) and the crystallographic cell parameter, so to indentify the crystalline phase. The intensity, on the other hand, contains information about the degree of crystallinity of the material.

In general, the width of a peak is inversely proportional to the average size of crystallites *Φ* along the direction normal to the plane *hkl* which gives rise to that specific reflection[14]. This can be expressed by Scherrer's equation:

$$\beta_{hkl} = \frac{K\lambda}{\Phi \cos\theta}$$

where β_{hkl} is the full width at half maximum (FWHM) of the peak and *K* is a constant which depends on the shape of the crystallite and whose value ranges from 0.7 to 1.4, but it can be set at 1 within a good approximation.

2.1.2.1 Experimental

X-ray diffraction (XRD) spectra are collected with a Bruker D8 Advance diffractometer with Bragg–Brentano geometry operating at 40 kV and 40 mA with Cu Kα radiation (λ = 0.154 nm).

Intensity data was collected every 0.03° with a count time of 10 s per step in the (*2θ*) range of 20° to 80°.

The various crystalline phases are identified by the search-match method using the JCPDS (*Joint Committee on Powder Diffraction Standards*) database. The phase composition and crystallite size of the powders are determined with great accuracy by Rietveld's powder structure refinement analysis of XRD data, using the MAUD (*Material Analysis Using Diffraction)* software[15]. The required crystallographic data are taken from ICSD[16] (*Inorganic Crystal Structure Database*).

2.1.3 *Scanning Electron Microscopy,* SEM

Scanning Electron Microscopy, SEM, provides information on the texture and surface morphology of materials. The resolution of this technique is of the order of nanometers and, if coupled with an analytical probe, allows analysis of the material's local composition[17-19].

When an electron beam interacts with a material different types of signal are generated (which can be roughly grouped as elastic and inelastic scattering events between the beam and the sample); the image of the sample is reconstructed by the electronics of the detectors that collect the out-coming signals.

The signals most commonly used to generate images are *secondary electrons* (SE) and *backscattered electrons* (BSE). Secondary electrons are generated from inelastic scattering between the primary electrons (of the in-coming beam) and electrons (from the core or the outer shells) of atoms in the sample. Such electrons have relatively low energies (< 50 eV). On the contrary, all electrons with energies above 50 eV are classified as backscattered, that is, generated as a result of elastic scattering. Increasing the atomic number Z of the atoms in the sample, the contribution of backscattered electrons is strongly favoured over the inelastically scattered ones.

A system of electromagnetic lenses focuses the incoming electrons on the sample so that the beam spot has variable size from a few nm to tens of nm. The area of analysis is then raster scanned and the out-coming signals are recorded as a function of the beam position to generate the image.

Secondary electrons are usually used in morphological investigation, because their emission yield is highly sensitive to the orientation of the surface with the primary beam as well as the presence of electric fields and/or magnetic fields at local level. Moreover, as they have low energy (between 0 and 50 eV), it is possible to reveal only those generated in the outer layers of the material.

The success of the SEM technique is mainly due to the fact that images are easily interpretable thanks to their three-dimensionality; furthermore the procedure to prepare samples, especially inorganic materials, is very simple.

2.1.3.1 Experimental

Field Emission-Scanning Electron Microscopy (FE-SEM) measurements are performed at primary beam acceleration voltages between 10 and 20 kV by a Zeiss SUPRA 40 VP instrument.

The microscope is equipped with a high performance Schottky field emitted source (ZrO/W), an electron accelerator (beam booster), which maintains the high energy level of the beam along the column minimizing the effects of broadening of the beam, and finally, a secondary electron detector (in-lens) with very high sensitivity.

2.1.4 *X-ray Photoelectron Spectroscopy,* XPS

X-ray Photoelectron Spectroscopy, XPS (also known as ESCA, *Electron Spectroscopy for Chemical Analysis*) exploits the photoelectric effect to obtain information on the composition and on the chemical "nature" of material surfaces[20].

When electromagnetic radiation hits a sample, the photons interact with the atoms in the material. If those photons have enough energy, they can provoke the emission of one or more electrons. The equation which describes this phenomenon is:

$$KE = h\nu - BE$$

where KE is the kinetic energy of the photo-emitted electron, $h\nu$ is the energy of the incident photon and BE is the binding energy of the photo-emitted electron[20]. During an XPS experiment the kinetic energy of the photo-emitted electron is measured, $h\nu$ is known and so the binding energy can be calculated, providing an estimate of the bound energy of that particular electron. In this way, the kinetic energy of an electron emitted from a core shell will provide information regarding the type of atom from which the electron was emitted and its chemical environment.

X-ray Photoelectron Spectroscopy is a surface sensitive analysis technique because only electrons from the outer layers of a solid material can escape without significant loss of energy. The electrons that come from layers below the surface (> 50 Å) lose most of their energy due to inelastic collision and are therefore either not able to escape the surface or their kinetic energy is so low once they do that they will only contribute to the background of the spectrum[20].

In an XPS analysis, the sample is placed in an ultra high vacuum chamber, i.e. a typical pressure of less than 10^{-8} Pa. The sample is then irradiated with a monochromatic low-energy beam that induces photoemission from the electron shells of the material's constituent atoms. These electrons have an energy that is characteristic not only of each single atom but also of the specific atomic orbital from which they originated.

The photo-emitted electrons are then detected as a function of their energy. Counting the number of electrons measured for each value of kinetic energy ($KE < hv$), a spectrum characterised by the presence of characteristic peaks for each emitting atoms can be generated. The area of these peaks is proportional to the amount (expressed as atomic percentage) of each element while the position of each peak (expressed in binding energy, *BE*) provides information on the chemical environment of the related atoms[20].

2.1.4.1 Experimental

X-ray photoelectron spectra are recorded using a Perkin-Elmer PHI 5600 ci spectrometer with standard AlK_α radiation (1486.6 eV), operating at 300 W.

The working pressure is less than 7×10^{-8} Pa. The spectrometer is calibrated by assuming the binding energy (*BE*) of the Au $4f_{7/2}$ line to be 84.0 eV with respect to the Fermi level.

Extended spectra (*survey*) are collected in the range 0 - 1350 eV (187.85 eV pass energy, 0.5 eV step, 0.025 $s\times step^{-1}$). Detailed spectra (*multiplex)* are recorded for specific peaks of interest relative to each element detected in the extended scan (11.75 eV pass energy, 0.1 eV step, 0.1 $s\times step^{-1}$).

The reported binding energies (*BE*s, standard deviation ± 0.2 eV) are corrected for charging effects, assigning the adventitious *C1s* line at *BE* of 284.8 eV[20]. The atomic percentage, after a Shirley type background subtraction[21], is evaluated by using the PHI sensitivity factors[22].

2.2 $Zn_{1-x}TM_xO$ (TM = Mn, Co, Cu): Sol gel Synthesis

As described above, *Sol gel* synthesis is a method with numerous parameters, which, if properly manipulated, can help to obtain materials with targeted characteristics in terms of composition, structure and morphology. On the other hand, the large number of variables makes the process difficult to control precisely; consequently the optimisation of the synthesis conditions is a process that requires high precision and is not easy to implement.

The choice of the molecular precursors, the catalyst and the solvent has to be carried out wisely, taking into consideration many different aspects. First of all, it is important to control the reactivity of the system. Furthermore, it is important to achieve a very "clean" process, i.e. to avoid contamination by any species that would not be eliminated during the calcination process[10].

For these reasons, zinc acetate di-hydrate ($Zn(OOCCH_3)_2 \cdot 2H_2O$, Fluka 99%) is used as molecular precursor in the presence of a basic catalyst such as NH_4OH solution.

NH_3 as the pH regulator is preferred because it can be completely removed upon calcination, not leaving any impurities behind. Furthermore, according to Narendar and Messing[23], ammonia itself has a structural influence on the *gel* as well: ammonium carboxylate bonds also exhibit a cross linking or a bridging character, thereby raising the viscosity of the solution and preventing long-range ordering.

The acetate salt of Zn^{2+} is chosen because the organic counter-ion will also be completely removed upon calcination. For the same reason, all the metal precursors for the various dopants are acetate salts: specifically manganese(II) acetate tetra-hydrate ($Mn(OOCCH_3)_2 \cdot 4H_2O$, Aldrich 99.99%), cobalt(II) acetate tetra-hydrate ($Co(OOCCH_3)_2 \cdot 4H_2O$, Sigma-Aldrich 99.99%) and copper(II) acetate mono-hydrate ($Cu(OOCCH_3)_2 \cdot H_2O$, Aldrich 99.99%).

In order to prevent early precipitation during the *Sol gel* synthesis, the optimal gelation conditions have to be determined. Citric acid ($C_6H_8O_7$), from many that were tested, turned out to be an excellent complexing agent in preventing such precipitation.

The pH of the precursor solution is kept at 11 to assure a complete deprotonation of citric acid (pK_{a3} = 6.4), necessary for a maximum coordination of Zn^{2+}. Furthermore, this prevent the precipitation of the insoluble $Zn(OH)_2$ species.

The monophasic character of the amorphous gel seems to be a necessary requirement for simultaneous particle formation upon calcination, which has the consequence of forming the desired unimodal particle size distribution.

Different samples were prepared using different parameters (i.e. varying the pH, ratio between reagents…) to determine the best set of conditions to control the growth of the ZnO nanoparticles. The final optimised set of synthetic conditions will be presented in the next section.

2.2.1 *Experimental*

The undoped ZnO nanosystem is prepared from aqueous solutions of the precursor compound (Zn : H_2O = 1 : 500). The *Sol gel* reactions occurred under basic conditions by adding concentrate ammonia solution (28%) to the precursor solution to reach pH ~ 11. To better control and stabilise the system during the aging process, citric acid (CA) is added (Zn : CA = 1 : 1). The solution is stirred at room temperature for 7 h before evaporation of solvent in an oven at 90°C to get uniform *gel* formation. To obtain white powder the *gel* is successively annealed for 3 h in air between 400 and 800°C.

In the case of transition metal ion doped systems, $Zn_{1-x}TM_xO$ (with TM = Mn, Co and Cu), the same synthetic conditions are adopted: the composition of precursor solutions is kept as M : H_2O = 1 : 500 (where M = Zn + TM, representing the sum of the zinc and the transition metal ion concentrations), the pH is adjusted around 11 and the stabiliser is added to maintain M : CA = 1 : 1. For each dopant, different concentrations are used, the concentration of the metal ion was varied from 1% atomic up to 10% atomic (which correspond to x = 0.01, 0.03 and 0.10 in $Zn_{1-x}TM_xO$).

Each sample from each TM-doped ZnO series is treated at different temperatures to study the influence of this parameter on the final product in terms of microstructure, composition and morphology.

Different transition metal ions, such as manganese, cobalt and copper, are introduced in ZnO to determine the influence of the nature of the dopant in modifying the physical-chemical properties of the final system. Changing their concentration, will also allow study of the evolution of the composition of the materials, in particular the formation of possible secondary phases that can alter the properties of doped ZnO nanoparticles.

2.3 $Zn_{1-x}TM_xO$ (TM = Mn, Co, Cu): Characterisation

In this section conventional characterisation of ZnO based nanoparticles will be presented. In particular, the structure, composition and morphology of the materials will be discussed on the basis of the results obtained through complementary techniques such as XRD, SEM and XPS.

It is important to define the characteristics of the systems under investigation, as a function of the different synthetic conditions, in order to fully understand the influence of these factors on the catalytic, optical and magnetic properties.

2.3.1 Undoped ZnO

Results regarding undoped ZnO will be discussed in terms of processing temperature: as will be presented, different annealing treatments are able to modify the crystallinity of the systems, as well as the average particle size, the presence of defects and in particular the hydroxyl residues (which derives from an incomplete reticulation of metal centres during the *Sol gel* synthesis).

2.3.1.1 *X-ray Diffraction,* XRD

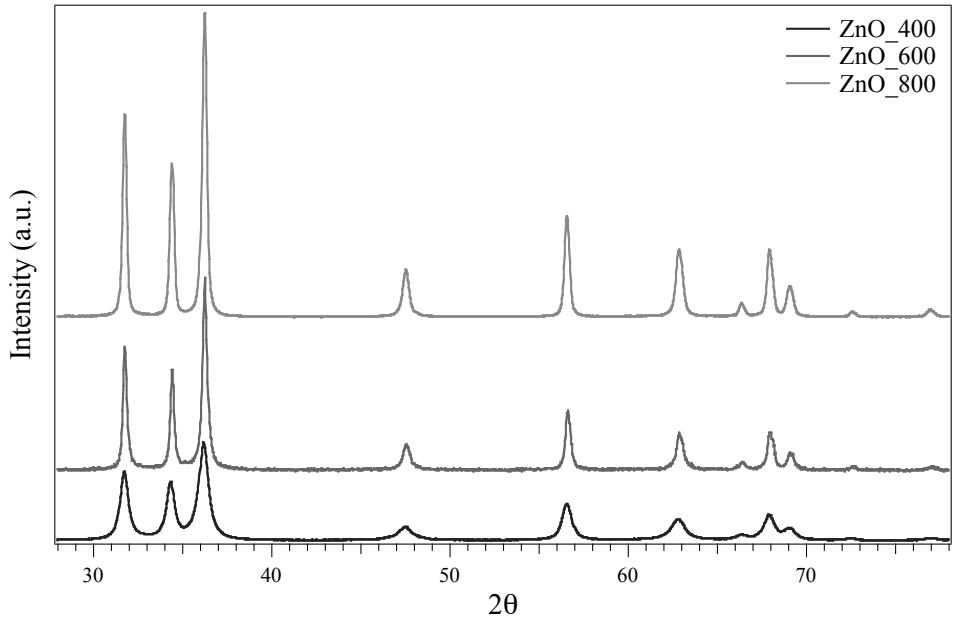

Figure 3: XRD spectra of undoped ZnO treated at different temperature.

The structural evolution of undoped ZnO is investigated by XRD analysis as shown in figure 3. ZnO_400, which is annealed at the lowest temperature, shows the presence of a single crystalline phase.
More severe treatment conditions, up to 800°C, did not induce further modifications to the powder microstructure, and the wurtzite crystalline phase is retained.

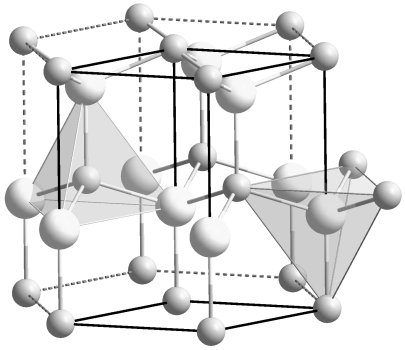

Figure 4: Wurtzite crystal structure, coordination polyhedra are shown.

Accordingly, the diffraction pattern of the ZnO_800 (figure 5) showed several reflections whose position and relative intensity identified the hexagonal wurtzite structure (JCPDS 00-036-1451). This structure, AX, can be described as an *hcp* array of atoms in which one half of the available tetrahedral interstices are filled by atoms A and vice versa (figure 4).

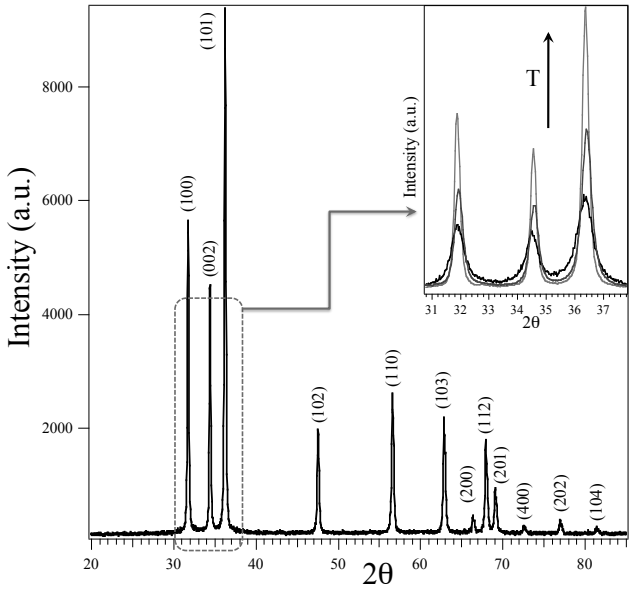

Figure 5: XRD spectrum of ZnO_800 (JCPDS n°00-036-1451).
The inset shows the increase of the signals due to increased temperature.

A higher annealing temperature results in better crystallinity of the system as seen in the intensity of diffraction lines. This effect can be easily seen in figure 3 as well as in the inset of figure 5. Raising the processing temperature results in an increase of the overall crystallinity of the materials, due to the removal of vacancies and lattice defects, which, in turn, results in higher intensity diffraction peaks.

The widths of the diffraction peaks, which are related to the average dimensions of ZnO crystallites, decrease at increasing temperatures (inset of figure 5). Stronger

annealing conditions lead to larger oxide particles: nanocrystalline ZnO with an average size of a few tens of nanometers (20 nm) are obtained at 400°C while at 800°C the average size increase up to ~ 100 nm; the main particles size of sample ZnO_600, treated at an intermediate temperature, is of about 50 nm.

2.3.1.2 *Scanning Electron Microscopy,* SEM

To obtain direct evidence of the size, shape and distribution of nanoparticles, samples are examined by SEM. In particular, ZnO nanoparticles synthesised by *Sol gel* with different annealing treatment are analysed to determine the effects that temperature has on the growth of particles.

As shown in figure 6, sample ZnO_400, synthesised at low temperature has a "sponge" like structure. Nanoparticles, spherical in shape, with an average size less than 30 nm aggregate into highly porous three-dimensional structures.

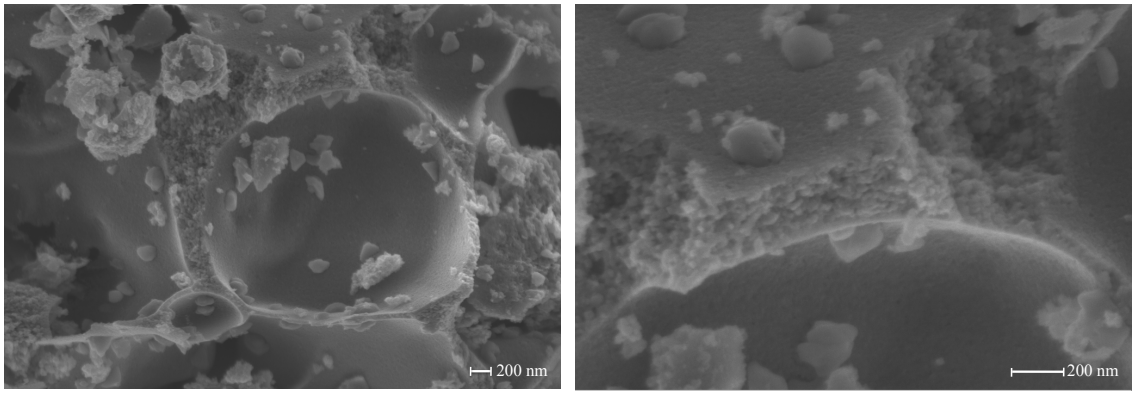

Figure 6: SEM images of ZnO_400: two different magnification if the same area, to highlight primary and secondary structure of nanopowders.

Upon increasing the calcination temperature up to 600°C, as shown in figure 7 for sample ZnO_600, there is a rise in the average particle size up to about 50 nm, while the "sponge"-like structure is maintained. In both cases, nanoparticles appear to share certain faces producing a nanoscale, 3-dimensional, porous network.

The sample treated at a higher temperature, ZnO_800, shows the same kind of arrangement of spherical shaped nanoparticles: the average size increases up to roughly 100 nm. SEM images of this sample are not shown.

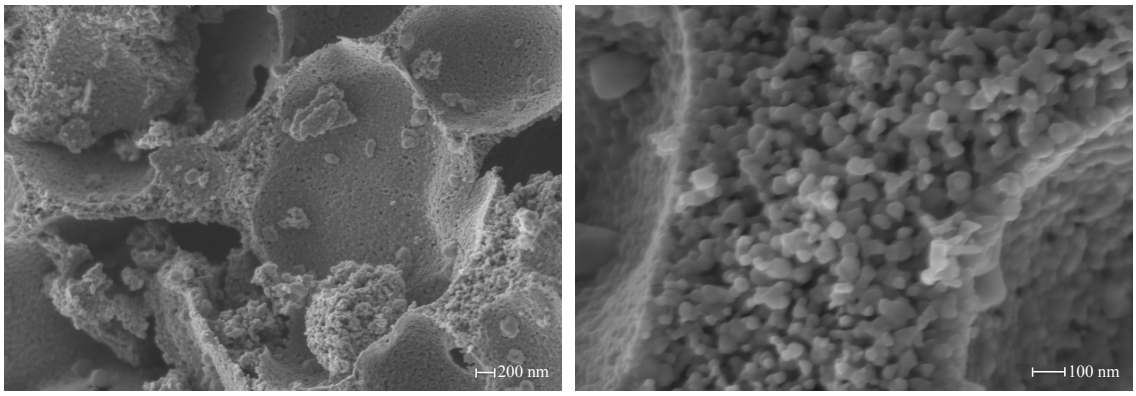

Figure 7: SEM images of ZnO_600: two different magnification if the same area, to highlight primary and secondary structure of nanopowders.

These considerations are in full agreement with the results obtained in XRD: the assumption of spherical nanoparticles is confirmed as well as the variation of the average particle size with respect to the annealing temperature. It has been proven that it is possible to effectively manipulate the morphology and the dimensionality of the semiconductor by varying the synthesis conditions.

2.3.1.3 *X-ray Photoelectron Spectroscopy,* XPS

The surface composition of undoped ZnO powders are thoroughly investigated by XPS analysis as a function of the thermal treatment. The XP extended spectra (*survey*) do not reveal the presence of any unexpected species (i.e. other than Zn, O, C); figure 8 shows, as an example, the *survey* spectrum of ZnO_400. The binding energies of the XP peaks measured for the different samples are summarised in table 1.

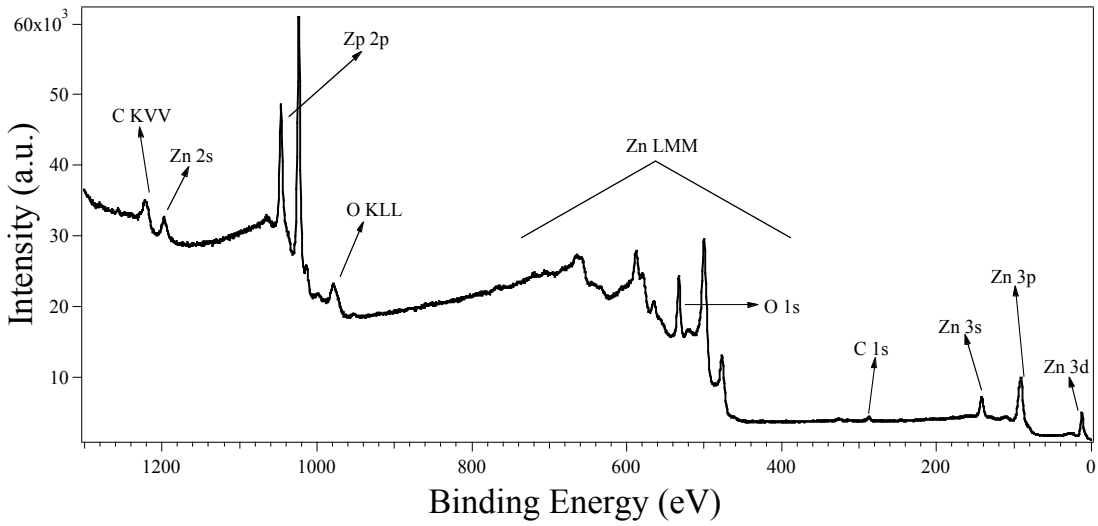

Figure 8: XP extended spectrum (*survey*) of ZnO_400.

Table 1. XPS peak positions (Binding Energy, eV) obtained for all the undoped ZnO powders.

Samples	*Zn2p$_{3/2}$*	*O1s (ret)*	*O1s (OH)*
ZnO_400	1021.4	530.3	531.7
ZnO_600	1021.2	530.2	531.8
ZnO_800	1021.1	530.1	531.6

The *BEs* measured for the *Zn2p$_{3/2}$* core level of the ZnO samples are characteristic of Zn(II) of the same environment regardless of the temperature of the thermal treatment[20,22,24] (table1). In fact the *Zn2p* photoelectron peak ($BE_{Zn2p3/2}$ = 1022.1 eV, Δ_{SO} = 23 eV) is typical of the presence of Zn(II) ions in an oxide environment[20,22,24]. As an example, the *Zn2p* XP signal relative to ZnO_400 is reported in figure 9.

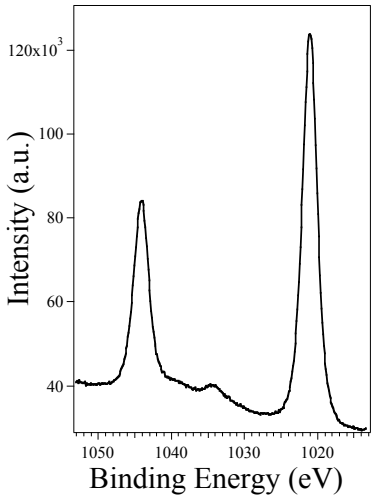

Figure 9: *Zn2p* XP signal of ZnO_400.

The *O1s* photoelectron peak showed a broad profile for all three different ZnO samples treated at different temperatures. Figure 10 shows the corresponding spectra of samples ZnO_400 (a) and ZnO_800 (b), respectively; ZnO_600 peak is not shown.

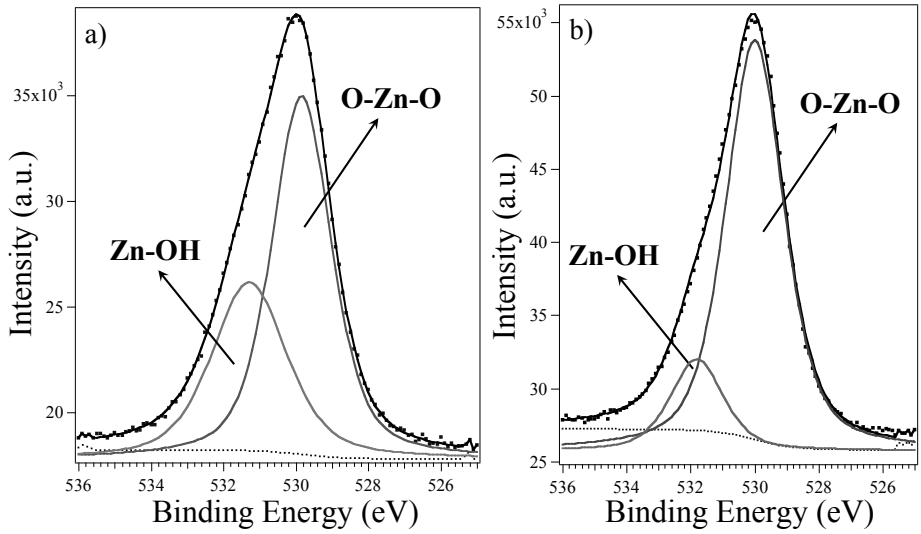

Figure 10: *O1s* XP signal of a) ZnO_400 and b) ZnO_800. The fitting of these signals is also reported.

This broadening is mainly due to the presence of two components at *BE* values of 530.1 eV and 531.9 eV attributed to the lattice oxygen in a Zn-O-Zn network and to the Zn-OH groups[20,22,24], respectively. The latter derives from the synthetic process and

confirms that a complete polymerization of the precursors into the final oxide was not fully achieved. On increasing the annealing temperature, the amount of hydroxyl groups on the surface sample decreased, resulting in a sharper *O1s* band shape but the presence of –OH groups was still detected (figure 10, table 2).

The atomic compositions obtained from XPS analyses are summarised in table 2. Regarding the oxygen composition, the two different components are taken into account and the relative intensity obtained by the fitting procedure is also reported.

Table 2. XPS compositions for all the undoped ZnO powders.

Samples	***Oxygen***		**O_{TOT}/ Zn**
	O1s (ret)	***O1s (OH)***	
ZnO_400	62%	38%	1.2
ZnO_600	72%	28%	1.4
ZnO_800	87%	13%	1.4

Taking into account the presence of two different oxygen components, the ratio between O/Zn on the surface of the material is slightly higher than expected for a ZnO with an ideal stoichiometry of 1:1, as can be seen in table 2.

As mentioned before, on increasing the processing temperature the contribution of hydroxyl groups on the surface decreases, due to a better reticulation of the metal centres. Accordingly, changing the synthetic condition it is possible to modulate the surface composition of the semiconductor, which will have consequences on some of the properties reported in the following chapters.

2.3.2 $Zn_{1-x}Mn_xO$

In this section results on the manganese doped ZnO will be presented. Data will be discussed in terms of the powder's composition (i.e. dopant concentration which varies in a range of $0.01 \leq x \leq 0.10$ in $Zn_{1-x}Mn_xO$) and the processing temperature.

2.3.2.1 *X-ray Diffraction,* XRD

Some of the XRD spectra for the different $Zn_{1-x}Mn_xO$ powders are shown in figure 11. In particular, diffractograms of the $Zn_{0.99}Mn_{0.01}O$ (figure 11a) and $Zn_{0.90}Mn_{0.10}O$ (figure 11b) series treated at different temperatures are reported.

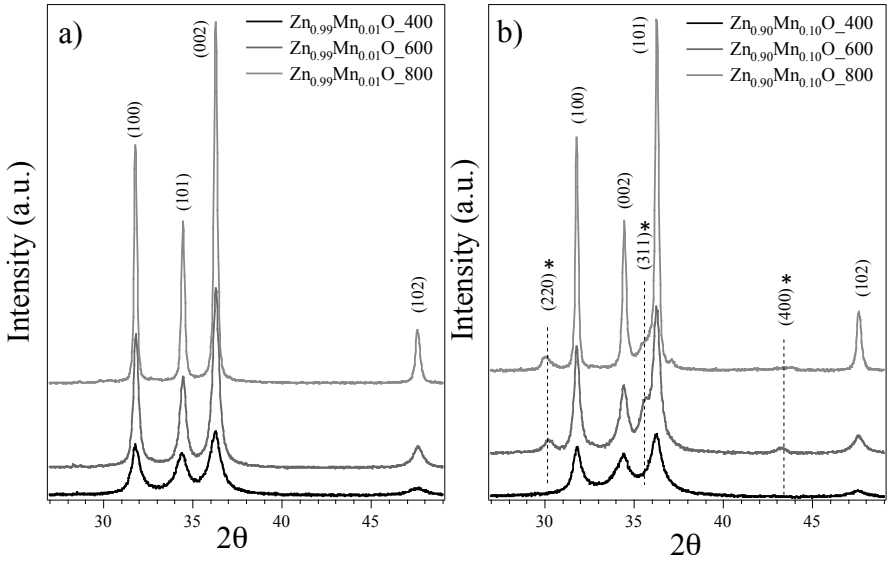

Figure 11: XRD spectra of $Zn_{1-x}Mn_xO$ treated at different temperature **a)** x = 0.01 reflexes relative to ZnO wurtzite phase are shown (JCPDS 00-036-1451) **b)** x = 0.10 reflexes relative to the ZnO wurtzite phase (JCPDS 00-036-1451) and to the $ZnMnO_3$ marked with a star (JCPDS 00-019-1461) are shown.

Mn-doped ZnO samples show different structural phases depending on the concentration of the dopant. When the manganese is present in low content (x = 0.01 figure 11a) only the ZnO wurtzite structure (JCPDS 00-036-1451) is detected for all the samples independent of the annealing temperature. The same trend is observed for samples with higher amount of dopant, $Zn_{0.97}Mn_{0.03}O$, whose spectra are not reported here. In both cases it is likely that in the specimens with low dopant content, the manganese ions are dispersed in the ZnO matrix occupying substitutional Zn sites, as will be confirm by further investigations described in the following chapters.

A second phase of $ZnMnO_3$ (JCPDS 00-019-1461), with oxidation of Mn^{2+} to Mn^{4+}, starts to be detected in samples $Zn_{0.90}Mn_{0.10}O$ (figure 11b) increasing the processing temperature. A diagram of the $ZnMnO_3$ phase, which is isostructural with Ilminite of general formula ABX_3, is shown in figure 12. Both metal ions are in octahedral coordination sites in alternating layers of atoms, A and B, aligned parallel to the (001) plane.

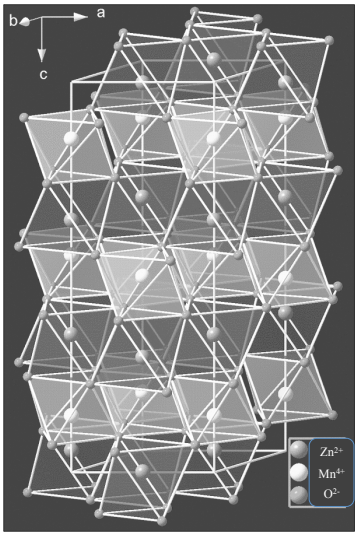

Figure 12: $ZnMnO_3$ crystal structure.

Furthermore, comparing the widths of the different diffraction peaks, the presence of manganese, as a dopant, does not seem to influence the particles' average size with respect to the undoped ZnO. The annealing temperature seems to be, accordingly, an independent parameter to control the growth of the nanoparticles from about 20 nm in size, for powders treated at 400°C, up to 100 nm when samples are processed at 800°C.

2.3.2.2 *X-ray Photoelectron Spectroscopy,* XPS

The surface chemical compositions of $Zn_{1-x}Mn_xO$ are analysed by XP spectroscopy as a function of structural evolution (i.e. annealing temperature and dopant concentration).

The XP extended spectra (*survey*) do not reveal the presence of unexpected species (i.e. other than Zn, Mn, O, C); figure 13 shows, as an example, the *survey* spectrum of $Zn_{0.90}Mn_{0.10}O$_400.

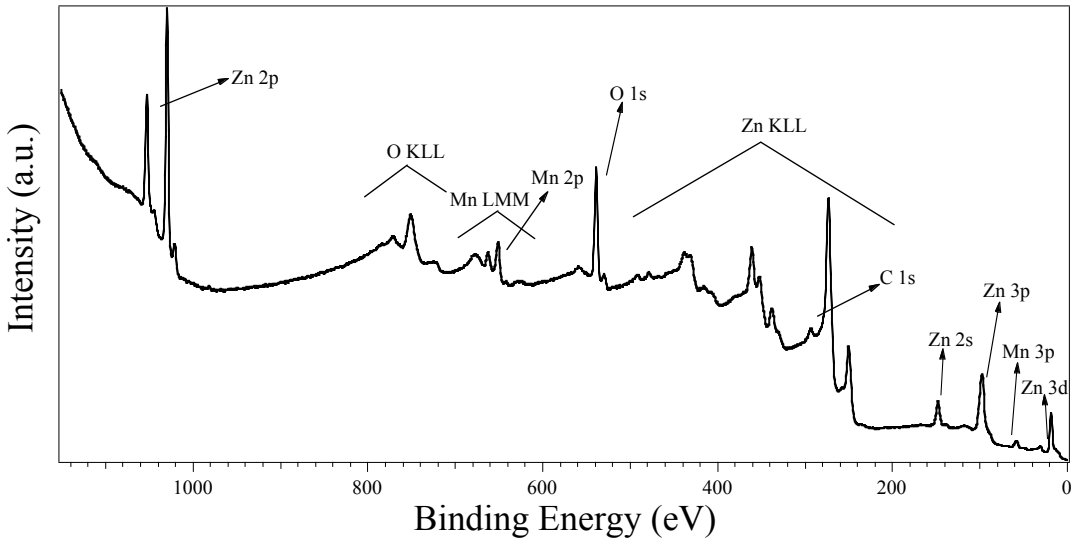

Figure 13: XP extended spectrum (*survey*) of $Zn_{0.90}Mn_{0.10}O$_400.

In general, on doping with manganese, the *Zn2p* and *O1s* signals do not undergo significant changes. This is true in particular for the two series with low concentrations of the transition metal ion, $Zn_{0.99}Mn_{0.01}O$ and $Zn_{0.97}Mn_{0.03}O$. The binding energies of the XP peaks measured for all samples are summarised in table 3. Spectra will be reported only for the series $Zn_{0.99}Mn_{0.01}O$, as an example.

Table 3. XPS peak positions (Binding Energy, eV) obtained for $Zn_{0.99}Mn_{0.01}O$ and $Zn_{0.97}Mn_{0.03}O$ powders.

Samples	*Zn2p$_{3/2}$*	*Mn2p$_{3/2}$*	*O1s (ret)*	*O1s (OH)*
$Zn_{0.99}Mn_{0.01}O$				
$Zn_{0.99}Mn_{0.01}O$_400	1021.3	641.1	530.0	531.6
$Zn_{0.99}Mn_{0.01}O$_600	1021.4	641.1	530.2	531.8
$Zn_{0.99}Mn_{0.01}O$_800	1021.2	641.3	530.1	531.9
$Zn_{0.97}Mn_{0.03}O$				
$Zn_{0.97}Mn_{0.03}O$_400	1021.1	641.3	530.1	531.8
$Zn_{0.97}Mn_{0.03}O$_600	1021.3	641.3	530.0	531.9
$Zn_{0.97}Mn_{0.03}O$_800	1021.3	641.1	530.1	531.9

The analysis of the *Zn2p* photoelectron peaks ($BE_{Zn2p3/2}$ = 1022.1 eV, Δ_{SO} = 23 eV) revealed the presence of Zn(II) ions in an oxide environment[20,22,24] in all samples. (figure 14a, table 3). This is analogous to the signal *Zn2p* detected for the undoped ZnO powders.

Regarding the *Mn2p* photoelectron peak (figure 14b, table 3), it shows the presence of Mn(II) ions in an oxide environment[20,22,24] ($BE_{Mn2p3/2}$ = 641.3 eV, Δ_{SO} = 12 eV) independent of the annealing temperature.

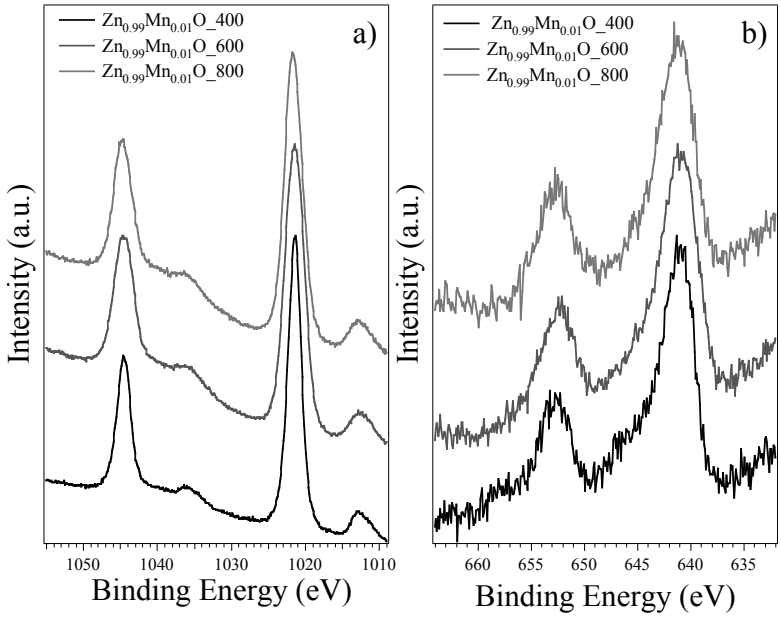

Figure 14: XP spectra of $Zn_{0.99}Mn_{0.01}O$ treated at different temperature **a)** *Zn2p* signal **b)** *Mn2p.*

The fitting procedure, not shown here, of the *O1s* XP peak of both series of compounds shows the presence of two contributions, as in the case of the undoped ZnO; also, a similar trend in function of the annealing temperature is maintained (table 4).

The atomic compositions obtained from XPS analyses are summarised in table 4.

Table 4. XPS compositions for all the $Zn_{0.99}Mn_{0.01}O$ and $Zn_{0.97}Mn_{0.03}O$ powders.

Samples	*Oxygen*		Mn/Zn	O_{TOT}/(Zn+Mn)
	O1s (ret)	*O1s (OH)*		
$Zn_{0.99}Mn_{0.01}O$				
$Zn_{0.99}Mn_{0.01}O$_400	62%	38%	0.03	1.6
$Zn_{0.99}Mn_{0.01}O$_600	74%	26%	0.04	1.8
$Zn_{0.99}Mn_{0.01}O$_800	88%	12%	0.04	1.8
$Zn_{0.97}Mn_{0.03}O$				
$Zn_{0.97}Mn_{0.03}O$_400	63%	37%	0.7	1.5
$Zn_{0.97}Mn_{0.03}O$_600	78%	22%	0.7	1.7
$Zn_{0.97}Mn_{0.03}O$_800	89%	11%	0.8	1.6

Taking into account the presence of two different oxygen components, the ratio between O/(Mn+Zn) on the surface of the material is higher than expected (ideal stoichiometry 1:1 for doped ZnO), as can be seen in table 4. The introduction of the dopant, on the other hand, does not significantly affect the O/(Mn+Zn) atomic ratio even though there is a small increase when compared with the corresponding values in the undoped system (table 2).

The XP Mn/Zn atomic ratios obtained for the two series, $Zn_{0.99}Mn_{0.01}O$ and $Zn_{0.97}Mn_{0.03}O$, are always higher than the corresponding nominal values (calculated from the weight quantities), suggesting manganese segregation on the surface.

Samples containing a higher concentration of manganese, $Zn_{0.90}Mn_{0.10}O$, showed structural changes corresponding with the change in synthesis conditions. Related XP spectra of *Zn2p* and *Mn2p* photoelectron peaks are reported in figures 15a and 15b, respectively. The same behaviour is observed for the *O1s* signal but the corresponding spectra are not reported here. Powders treated at 400°C and 600°C present the same features detected in the other two series: the binding energies of the XP peaks measured for those samples are summarised in table 5.

Table 5. XPS peak positions (Binding Energy, eV) obtained for $Zn_{0.90}Mn_{0.10}O$ powders.

Samples	*$Zn2p_{3/2}$*	*$Mn2p_{3/2}$*	*O1s (ret)*	*O1s (OH)*
$Zn_{0.99}Mn_{0.01}O$_400	1021.0	641.1	529.9	531.8
$Zn_{0.99}Mn_{0.01}O$_600	1021.2	641.0	529.8	531.9

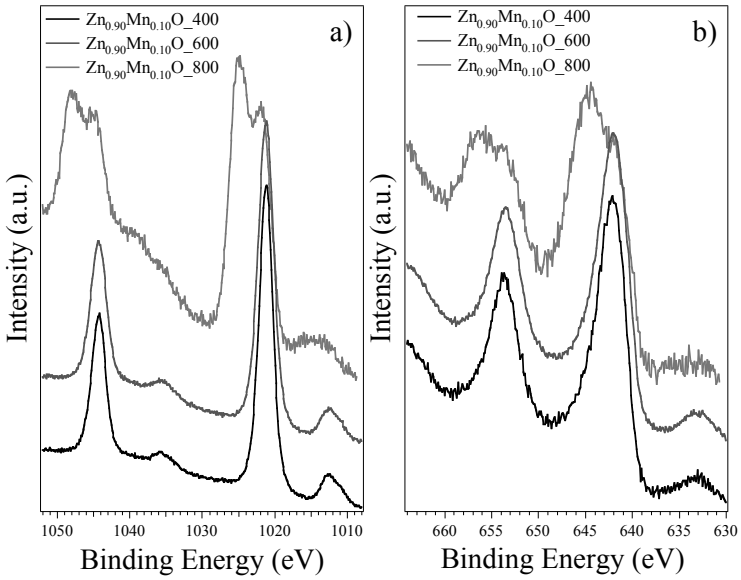

Figure 15: XP spectra of $Zn_{0.90}Mn_{0.10}O$ treated at different temperature **a)** *Zn2p* signal **b)** *Mn2p*.

Conversely, $Zn_{0.90}Mn_{0.10}O$ treated at 800°C showed completely different signals not only for *Mn2p* and *Zn2p* (figure 15) but also for the *O1s* photoelectron peak. As shown in figure 16, all three signals are fitted with two or more components due to the presence of different chemical environments.

The *Mn2p* signal (figure 16a) showed the presence of both Mn(II) ($BE_{Mn2p3/2}$ = 641.3 eV, Δ_{SO} = 12 eV) and Mn(IV) ($BE_{Mn2p3/2}$ = 643.8 eV, Δ_{SO} = 11.6 eV) in different oxide environment[20,22,24]. The latter is compatible with the existence of a $ZnMnO_3$ phase as detected with the XRD.

The *Zn2p* photoelectron peak (figure 16b) showed the presence of two different Zn(II) species ($BE_{Zn2p3/2}$ = 1022.2 eV, Δ_{SO} = 23 eV and $BE_{Zn2p3/2}$ = 1025.0 eV, Δ_{SO} = 23.1 eV), both in an oxide environment, which is compatible with the coexistence of two phases of ZnO and $ZnMnO_3$.

Finally, the *O1s* peak showed a broad profile, mainly due to the presence of four different components (figure 16c) which it is possible to attribute to the lattice oxygens and hydroxyl groups in the two different networks of zinc oxide and $ZnMnO_3$. The binding energies of the XP peaks obtained by the fitting procedures and the relative intensity of each component are summarised in table 6.

Table 6. XPS peak positions (Binding Energy, eV) obtained for $Zn_{0.90}Mn_{0.10}O$_800 sample.

	Zn2p		***Mn2p***		***O1s***			
	I	**II**	**I**	**II**	**I**	**II**	**III**	**IV**
position	1021.4	1024.9	641.3	644.8	529.5	531.0	533.0	534.8
%	46.1	53.9	45	55	22.5	25	34.5	18

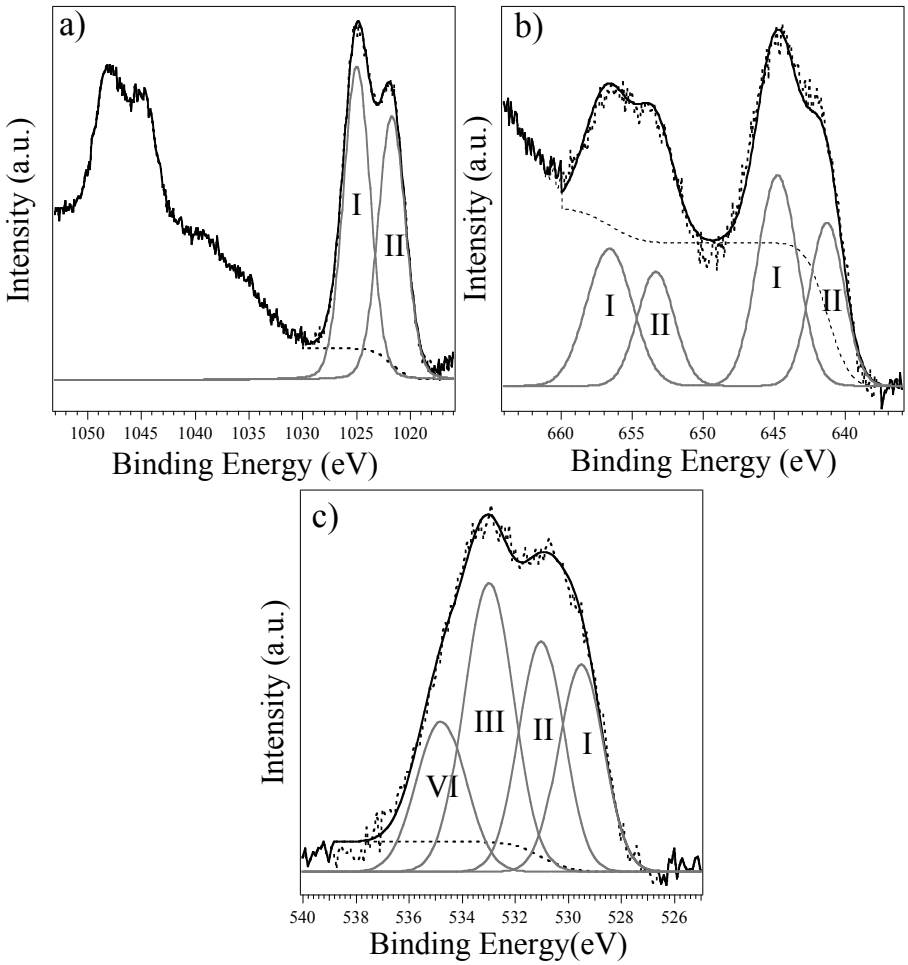

Figure 16: XP spectra of $Zn_{0.90}Mn_{0.10}O$_800 **a)** *Zn2p* signal **b)** *Mn2p* and **c)** *O1s* signal. Fitting components are also reported for all the three signals.

Table 7. XPS compositions for all the $Zn_{0.90}Mn_{0.10}O$ powders.

Samples	Mn/Zn	O_{TOT}/(Zn+Mn)
$Zn_{0.99}Mn_{0.01}O$		
$Zn_{0.99}Mn_{0.01}O$_400	17	1.8
$Zn_{0.99}Mn_{0.01}O$_600	19	1.8
$Zn_{0.99}Mn_{0.01}O$_800	35	2.8

The atomic compositions of $Zn_{0.90}Mn_{0.10}O$ series obtained from XPS analyses are summarised in table 7. Taking into account the presence of different oxygen components, the ratio between O/(Mn+Zn) in $Zn_{0.99}Mn_{0.01}O$_400 and $Zn_{0.99}Mn_{0.01}O$_600 is higher than expected for a doped ZnO with an ideal stoichiometry of 1:1. $Zn_{0.99}Mn_{0.01}O$_800 shows an even higher ratio due to the presence of the second phase of $ZnMnO_3$. Comparing these results with those of the undoped system (table 2) introduction of a dopant does not significantly affect the O/(Mn+Zn) atomic ratio even though there is a small increase in the values.

The XP Mn/Zn atomic ratios obtained for the three samples $Zn_{0.90}Mn_{0.10}O$, treated at a range of temperatures, are always higher than the corresponding nominal values (calculated from the weight quantities), suggesting manganese segregation on the surface. Finally, powder $Zn_{0.90}Mn_{0.10}O$ treated at 800°C shows a higher ratio for both Mn/Zn and O/(Zn+Mn) due to the presence of two different phases of ZnO and $ZnMnO_3$.

These results, obtained by *X-ray Photoelectron Spectroscopy*, are in good agreement with those inferred from *X-ray Diffraction*. The surface composition of $Zn_{0.90}Mn_{0.10}O$_800 revealed different contributions that could trace back to the presence of two distinct phases consistent with ZnO and $ZnMnO_3$. Samples with lower concentration of manganese show a substantial retention of the dominant structure being wurtzite, like ZnO, where the dopant should occupy substitutional sites.

Varying the annealing temperature, as in the case of undoped ZnO, provides the ability to manipulate the ratio between lattice oxygen and hydroxyl on the surface of the nanoparticles. This effect seems to remain unaffected by the presence of manganese as a dopant, as long as the formation of a second phase is avoided. In fact, the contribution of –OH groups is altered only by changing the annealing conditions: an increase in temperature decreases the hydroxyl residue on the surface.

2.3.3 $Zn_{1-x}Co_xO$

In this section results on the cobalt doped ZnO will be presented. As in the previous section, data will be discussed in terms of the powder's composition (i.e. the dopant concentration which varies in a range of $0.01 \leq x \leq 0.10$) and the processing temperature.

2.3.3.1 *X-ray Diffraction,* XRD

To understand the structural evolution of the cobalt doped system, a selection of XRD spectra for $Zn_{1-x}Co_xO$ powders are shown in figure 17. Diffractograms of the $Zn_{0.99}Co_{0.01}O$ (figure 17a) and $Zn_{0.90}Co_{0.10}O$ (figure 17b) series treated at different temperatures are reported.

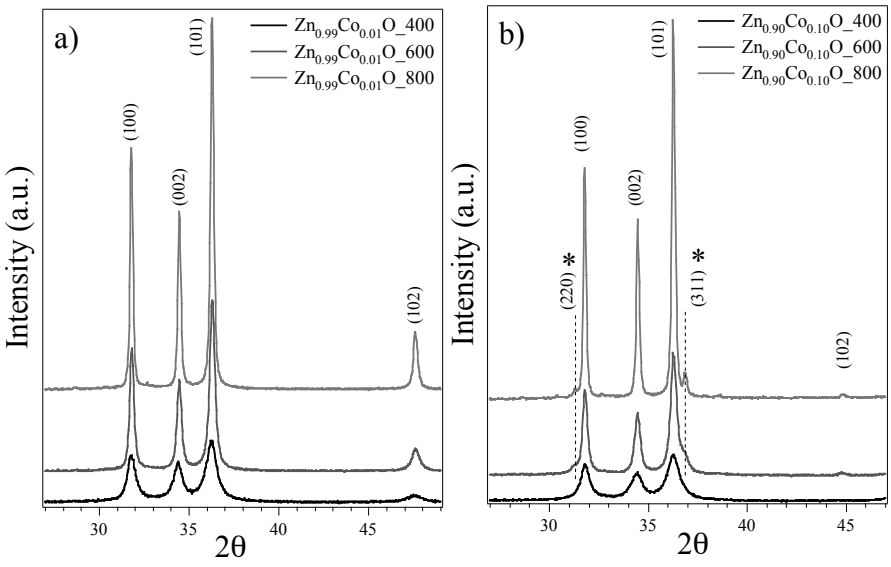

Figure 17: XRD spectra of $Zn_{1-x}Co_xO$ treated at different temperature **a)** x = 0.01 reflexes relative to ZnO wurtzite phase are shown (JCPDS 00-036-1451) **b)** x = 0.10 reflexes relative to the ZnO wurtzite phase (JCPDS 00-036-1451) and to the Co_3O_4 marked with a star (JCPDS 01-080-1532) are shown.

In perfect analogy with what has been observed in manganese-doped samples, only the ZnO wurtzite phase (JCPDS 00-036-1451) is detected when cobalt is present in low concentration (x = 0.01 figure 17a). The same trend is observed for samples with a higher dopant concentration, $Zn_{0.97}Co_{0.03}O$, whose spectra are not reported here. As for the manganese doped sample, further investigations described in the following chapters will confirm that, in samples with low dopant concentration, the cobalt ions are dispersed in the ZnO matrix occupying substitutional Zn sites.

On the other hand, it is possible to observe the segregation of a secondary phase of Co_3O_4 (JCPDS 01-080-1532), with partial oxidation of the Co^{2+} to Co^{3+}, increasing the dopant concentration as detected in the $Zn_{0.90}Co_{0.10}O$ system (figure 17b). A scheme of the crystal structure of Co_3O_4 is shown in figure 18. The mixed-valency spinel has Co^{2+} (*Td*, tetrahedral sites) and Co^{3+} (*Oh*, octahedral sites) ions simultaneously present in the lattice; both sub-lattices are highlighted in figure 18.

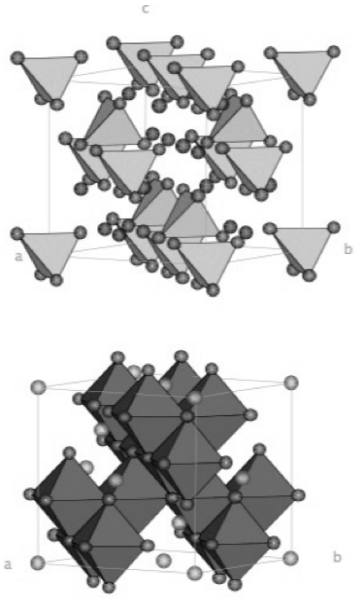

Figure 18: Co_3O_4 crystal structure. *Td* and *Oh* sites are highlighted.

Finally, by comparing the widths of the different diffraction peaks, the presence of cobalt, as in the case of manganese, does not seem to influence the particles' average size when compared with the undoped ZnO. This confirms that the annealing temperature is an independent parameter that can control the growth and the average dimensions of the nanoparticles from about 20 nm, for powders treated at 400°C, up to 100 nm when samples are processed at 800°C.

2.3.3.2 *X-ray Photoelectron Spectroscopy,* XPS

The surface chemical composition of $Zn_{1-x}Co_xO$ powders, are thoroughly investigated by XPS analysis as a function of the thermal treatment and dopant concentration.

The XP extended spectra (*survey*) do not reveal the presence of any unexpected species (i.e. other than Zn, Co, O, C); figure 19 shows, as an example, the *survey* spectrum of $Zn_{0.90}Co_{0.10}O$_400.

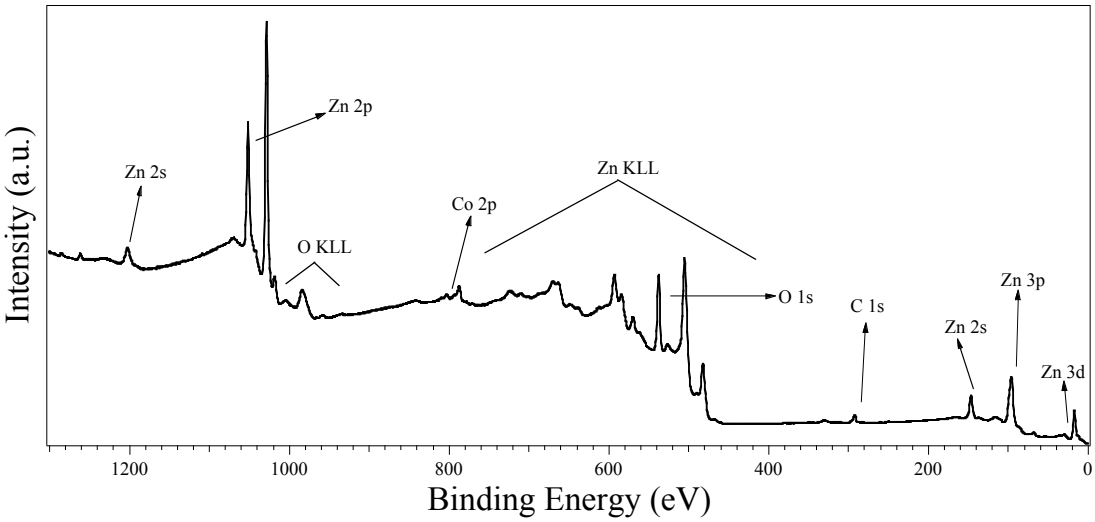

Figure 19: XP extended spectrum (*survey*) of $Zn_{0.90}Co_{0.10}O$_400.

The binding energies of the XP peaks measured for the different samples are summarised in table 9. Upon doping with cobalt, in good analogy with manganese, signals of *Zn2p* and *O1s* do not undergo significant changes in their band shapes and positions.

The *O1s* photoelectron peak showed a broad profile for all three different series of samples. As an example, figure 20 shows the relative spectra of $Zn_{0.97}Co_{0.03}O$_400 (a) and $Zn_{0.97}Co_{0.03}O$_800 (b).

Table 9. XPS peak positions (Binding Energy, eV) obtained for $Zn_{1-x}Co_xO$ system.

Samples	*Zn2p$_{3/2}$*	*Co2p$_{3/2}$*	*O1s (ret)*	*O1s (OH)*
$Zn_{0.99}Co_{0.01}O$				
$Zn_{0.99}Co_{0.01}O$_400	1021.2	780.7	530.0	531.8
$Zn_{0.99}Co_{0.01}O$_600	1021.3	780.6	530.2	531.8
$Zn_{0.99}Co_{0.01}O$_800	1021.3	780.7	530.1	531.9
$Zn_{0.97}Co_{0.03}O$				
$Zn_{0.97}Co_{0.03}O$_400	1021.2	780.6	530.2	531.8
$Zn_{0.97}Co_{0.03}O$_600	1021.3	780.6	530.0	532.0
$Zn_{0.97}Co_{0.03}O$_800	1021.4	780.7	530.1	531.8
$Zn_{0.90}Co_{0.10}O$				
$Zn_{0.90}Co_{0.10}O$_400	1021.4	780.7	530.1	531.8
$Zn_{0.90}Co_{0.10}O$_600	1021.4	780.8	530.0	531.9
$Zn_{0.90}Co_{0.10}O$_800	1021.4	780.7	530.1	531.9

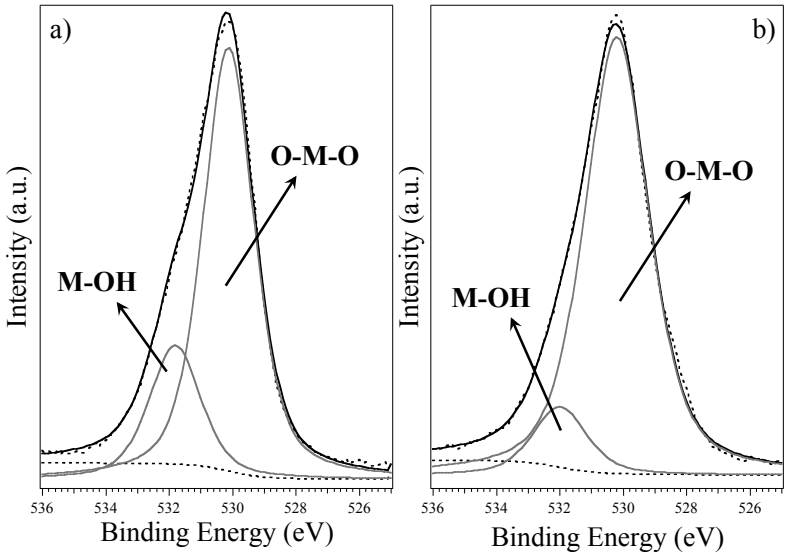

Figure 20: *O1s* XP signal of a) $Zn_{0.97}Co_{0.03}O$_400 and b) $Zn_{0.97}Co_{0.03}O$_800. The fitting of these signals is also reported.

This broadening is mainly due to the presence of two components at *BE* values of 530.1 and 531.9 eV attributed to the lattice oxygen in a M-O-M network and to the M-OH groups[20,22,24], respectively. It is worth noting that it is not possible to distinguish between the contribution of the two different metals, zinc and cobalt: as also reported in literature[20,22,24,25], typical binding energies for oxygen attributed to zinc or cobalt oxides are very similar. On increasing the annealing temperature, the amount of hydroxyl groups on the sample surface decreased, resulting in a sharper *O1s* band shape but the presence of –OH groups could still be detected (figure 20, table 10).

As an example, the *Zn2p* spectra of $Zn_{1-x}Co_xO$ samples treated at 600°C are reported in figure 21a. No variation in the shape or position of the two signals is observed indicating that the local environment has been retained. The binding energies of the XP peaks measured for the different samples are summarised in table 9.

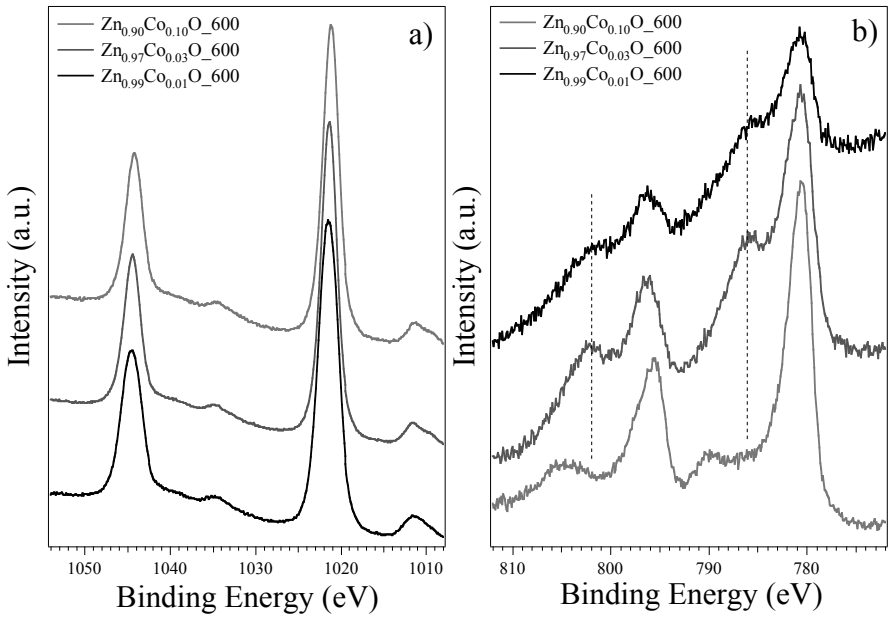

Figure 21: XP spectra of $Zn_{1-x}Co_xO$ treated at 600°C in function of cobalt concentration **a)** *Zn2p* signal **b)** *Mn2p*.

Regarding the cobalt, an example of the evolution of *Co2p* photoelectron signal in function of the dopant concentration is reported, for samples treated at 600°C, in figure 21b. All XP spectra showed the presence of Co(II) in an oxide environment[20,22,24] ($BE_{Co2p3/2}$ = 780.6 eV, table 9). Increasing the dopant concentration, the *Co2p* spin-orbit components and the corresponding shake-up satellites undergo sensible changes: the doublet separation decreases from 15.6 eV (series $Zn_{0.99}Co_{0.01}O$ and $Zn_{0.97}Co_{0.03}O$) to 15.1 eV (series $Zn_{0.90}Co_{0.10}O$) and the position of the shake-up satellite is shifted to a higher binding energy.

Those variations are consistent with the presence of, in all $Zn_{0.90}Co_{0.10}O$ powders, the mixed oxide, Co_3O_4[25]. In fact an important indicator of the mixed-valence oxide is the shape of the *Co2p* spectra. The cobalt in the two oxide forms, the first containing only Co(II) and the other being spinel-like in nature, are characterised by different intensities of the shake-up satellites[25,26]. *Co2p* spectra of $Zn_{0.90}Co_{0.10}O$ samples (figure 21b shows the sample treated at 600°C) exhibit a very low intensity satellite peaks that are typical[25,27] of the Co_3O_4.

Finally the atomic compositions of all $Zn_{1-x}Co_xO$ compounds obtained from XPS analyses are summarised in table 10.

Table 10. XPS compositions for all the $Zn_{1-x}Co_xO$ powders.

Samples	***Oxygen***		**Co/Zn**	**O_{TOT}/(Zn+Co)**
	O1s (ret)	***O1s (OH)***		
$Zn_{0.99}Co_{0.01}O$				
$Zn_{0.99}Co_{0.01}O$_400	64%	36%	0.02	1.1
$Zn_{0.99}Co_{0.01}O$_600	77%	23%	0.03	1.2
$Zn_{0.99}Co_{0.01}O$_800	82%	18%	0.02	1.2
$Zn_{0.97}Co_{0.03}O$				
$Zn_{0.97}Co_{0.03}O$_400	68%	32%	0.06	1.2
$Zn_{0.97}Co_{0.03}O$_600	78%	22%	0.06	1.2
$Zn_{0.97}Co_{0.03}O$_800	86%	14%	0.07	1.1
$Zn_{0.90}Co_{0.10}O$				
$Zn_{0.90}Co_{0.10}O$_400	66%	34%	0.14	1.2
$Zn_{0.90}Co_{0.10}O$_600	79%	21%	0.13	1.2
$Zn_{0.90}Co_{0.10}O$_800	87%	13%	0.14	1.2

The XP Co/Zn atomic ratios obtained for the all the series are always higher than the corresponding nominal values (calculated from the weight quantities), suggesting cobalt segregation on the surface. The introduction of the transition metal ions, does not significantly affect the O/(Co+Zn) atomic ratio if compared with the corresponding undoped system (table 2).

These results, obtained by XPS, are again in good agreement with those inferred from XRD. The surface composition of $Zn_{0.90}Co_{0.10}O$ treated at different temperatures, is compatible with the presence of two distinct phases consistent with ZnO and Co_3O_4. Samples with a lower concentration of cobalt instead show a substantial retention of the dominant structure of wurtzite-like ZnO with the dopant occupying substitutional sites.

The annealing temperature, as in the two previous cases, is capable of controlling the ratio of lattice oxygen to hydroxyl on the surface of the nanoparticles. This effect seems to not be affected by the presence of the dopant, in good analogy with the manganese doped samples.

2.3.4 $Zn_{1-x}Cu_xO$

In this final section, results on the copper doped ZnO will be presented. Data will be discussed in terms of the powder's composition (i.e. the dopant concentration which ranges from $0.01 \leq x \leq 0.10$) and the processing temperature.

Taking into account that those samples will be tested as catalyst in *Methanol Steam Reforming* reaction (data will be presented in chapter 4), a wider range of dopant concentrations is explored. In fact is important to understand what is the evolution of the system upon increasing copper concentration, in order to choose the best candidates to be tested as the catalyst.

2.3.4.1 *X-ray Diffraction,* XRD

A selection of XRD spectra for different $Zn_{1-x}Cu_xO$ powders is shown in figure 22. Specifically diffractograms of the $Zn_{0.99}Cu_{0.01}O$ (figure 22a) and $Zn_{0.90}Cu_{0.10}O$ (figure 22b) series treated at different temperatures are reported.

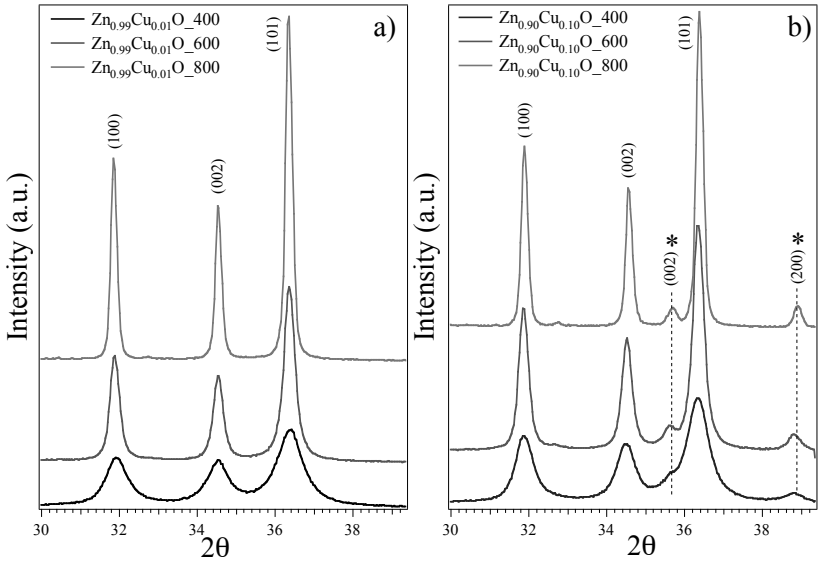

Figure 22: XRD spectra of $Zn_{1-x}Cu_xO$ treated at different temperature **a)** x = 0.01 reflexes relative to ZnO wurtzite phase are shown (JCPDS 00-036-1451) **b)** x = 0.10 reflexes relative to the ZnO wurtzite phase (JCPDS 00-036-1451) and to the CuO marked with a star (JCPDS 00-048-1648) are shown.

Doping with a small amount of copper, $Zn_{0.99}Cu_{0.01}O$ (figure 22a), does not cause significant changes in the XRD patterns. The hexagonal ZnO wurtzite structure is the only phase detected independent of the heat treatment temperature.

On the contrary, in samples doped with higher copper concentrations, starting from $Zn_{0.98}Cu_{0.02}O$ (spectra are not shown here) up to $Zn_{0.90}Cu_{0.10}O$ (figure 22b)

diffractograms also show small reflections characteristics of the monoclinic CuO phase (JCPDS 00-048-1648).

For two samples, $Zn_{0.90}Cu_{0.10}O$_400 and $Zn_{0.90}Cu_{0.10}O$_800 the weight fractions of the two phases are calculated by means of the Rietveld method as 92.0%wt (ZnO), 8.0%wt (CuO) and 91.8%wt (ZnO), 8.2%wt (CuO) respectively.

A diagram of the crystal structure of copper oxide is shown in figure 23. The copper atoms are coordinated by four oxygen atoms, in an approximately square planar configuration, forming an almost rectangular parallelogram; the oxygen coordination polyhedron has four Cu atoms at the corners of a distorted tetrahedron.

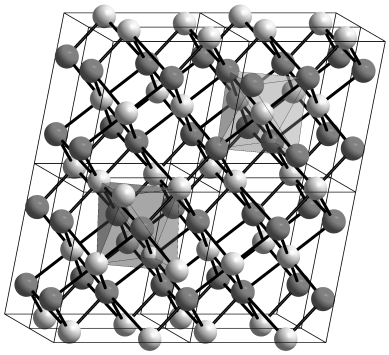

Figure 23: CuO crystal structure.

Finally, comparing the widths of the different diffraction peaks, the presence of copper, as in the case of the other two transition metal ions manganese and cobalt, does not seem to influence the particles' average size when compared with the undoped ZnO.

2.3.4.2 *X-ray Photoelectron Spectroscopy,* XPS

The surface chemical composition of $Zn_{1-x}Cu_xO$ is analysed by XP spectroscopy as a function of structural evolution (i.e. the annealing temperature and dopant concentration.

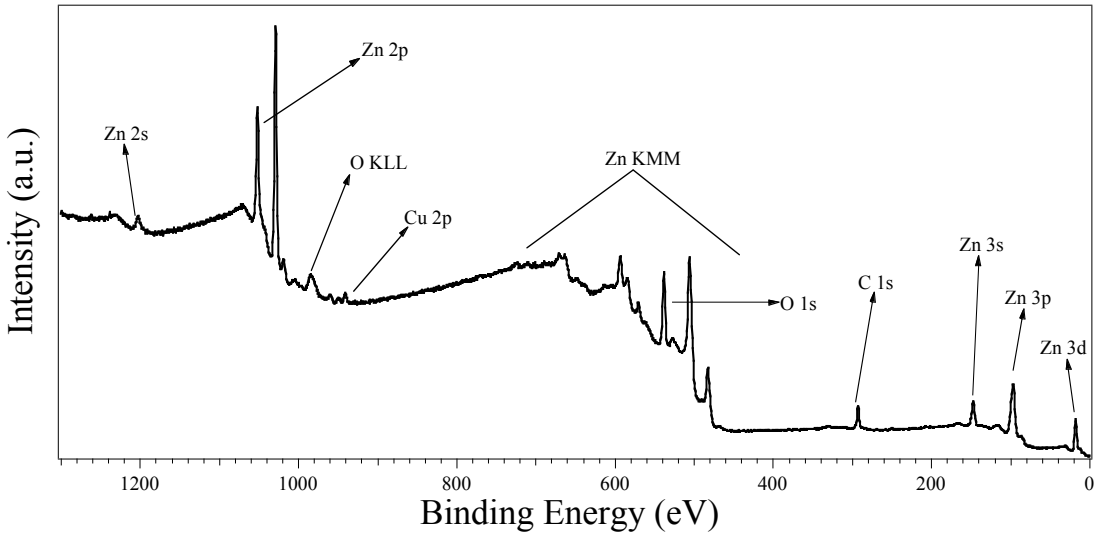

Figure 24: Extended spectrum (*survey*) of $Zn_{0.90}Co_{0.10}O$_400.

The XP extended spectra (*survey*) do not reveal the presence of any unexpected species (i.e. other than Zn, Cu, O, C); figure 24 shows, as an example, the *survey* spectrum of $Zn_{0.90}Cu_{0.10}O$_400.

Results from the two bound series, $Zn_{0.99}Cu_{0.01}O$ and $Zn_{0.90}Cu_{0.10}O$, will be presented here. In fact, analogous to what is described in the XRD section, samples with a dopant concentration higher than 1% atomic ($x > 0.01$) show the same behaviour regardless of the copper content. The binding energies of the XP peaks measured for these two series of samples are summarised in table 11.

Table 11. XPS peak positions (Binding Energy, eV) obtained for $Zn_{1-x}Cu_xO$ system.

Samples	*Zn2p$_{3/2}$*	*Cu2p$_{3/2}$*	*O1s (retI)*	*O1s (retII)*	*O1s (OH)*
$Zn_{0.99}Cu_{0.01}O$					
$Zn_{0.99}Cu_{0.01}O$_400	1022.1	933.1	530.4		531.9
$Zn_{0.99}Cu_{0.01}O$_600	1021.2	932.9	530.3		531.8
$Zn_{0.99}Cu_{0.01}O$_800	1022.1	932.9	530.4	529.6	532.0
$Zn_{0.90}Cu_{0.10}O$					
$Zn_{0.90}Cu_{0.10}O$_400	1021.4	932.9	530.1		531.8
$Zn_{0.90}Cu_{0.10}O$_600	1021.4	932.9	530.0		531.9
$Zn_{0.90}Cu_{0.10}O$_800	1021.4	933.0	530.1	529.7	531.9

Generally the introduction of copper does not cause significant changes in the *Zn2p$_{3/2}$ BE*, except for in sample $Zn_{0.99}Cu_{0.01}O$_400 (table 11, spectra are not shown here). In this sample the peak position shifts from 1021.4 eV to 1022.1 eV. This shift could be tentatively related to the more significant interaction with copper ions. A charge transfer between the zinc and copper ions could be responsible for these changes in binding energy.

The fitting procedure of the *O1s* XP peak of both series of samples treated at 400°C shows the presence of two contributions (figure 25a shows relative spectrum of $Zn_{0.99}Cu_{0.01}O$_400). The main peak at lower *BE* agrees with the expected value for lattice oxygen of ZnO in an oxide network. The contribution at higher *BE* can be attributed to surface hydroxyl groups. It is noteworthy that in both Cu-doped samples treated at 800°C a slight broadening of the *O1s* peak towards lower *BE* is indicative of the presence of another oxygen species (figure 25b shows relative spectrum of $Zn_{0.99}Cu_{0.01}O$_800). This contribution, centred at 529.6-529.7 eV (peak III figure 25b, table 11), is consistent with the lattice oxygen in CuO[28].

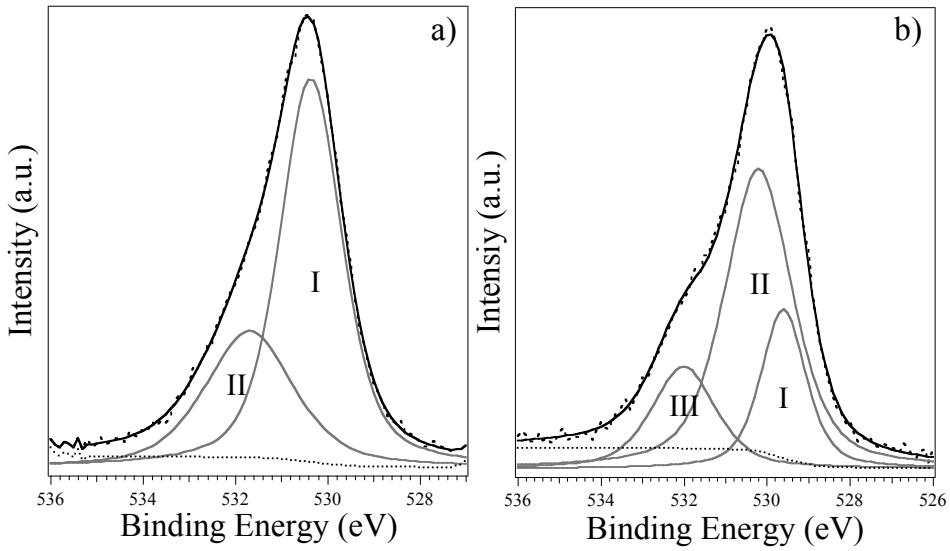

Figure 25: *O1s* XP signal of a) $Zn_{0.99}Cu_{0.01}O\_400$ and b) $Zn_{0.99}Cu_{0.01}O\_800$. The fitting of these signals is also reported.

The *Cu2p* photoelectron signal showed the presence of Cu(II) in an oxide environment[20,22,24] (BE_{Cu2p} = 932.5 eV, Δ_{SO} = 19.2 eV) independent of the dopant concentration and heating temperature. Spectra reported in figure 26 show the evolution of the copper signal with respect to the dopant concentration: on increasing the amount of copper, it is possible to detect, together with the *Cu2p* spin-orbit components, the corresponding shake-up satellite peaks.

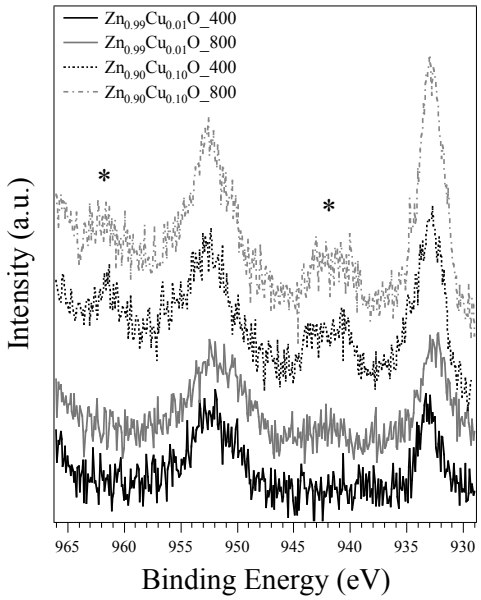

Figure 26: *Cu2p* XP signal of $Zn_{1-x}Cu_xO$ treated at different temperature. Shake up satellites are marked with a star.

Different types of Cu(II) are usually identified by analysis of the band shape profile of the *Cu2p* region. The *Cu2p* signals for Cu(II) oxide are characterised by the presence of intense shake-up satellites located at *BE* values 9 eV, higher than the main spin-orbit

split components[29,30,31,32]. Conversely, in the case of other derivatives shake-up satellites are almost undetectable[29,30,31,32].

The atomic compositions of $Zn_{1-x}Cu_xO$ compounds obtained from XPS analyses are summarised in table 12.

Table 12. XPS compositions for all the $Zn_{1-x}Cu_xO$ powders.

Samples	***Oxygen***			**Cu/Zn**	**O_{TOT}/(Zn+Cu)**
	O1s (retI)	***O1s (retII)***	***O1s (OH)***		
$Zn_{0.99}Cu_{0.01}O$					
$Zn_{0.99}Cu_{0.01}O$_400	67%		33%	0.03	1.3
$Zn_{0.99}Cu_{0.01}O$_600	77%		23%	0.03	1.4
$Zn_{0.99}Cu_{0.01}O$_800	59.8%	21%	19.2%	0.04	1.4
$Zn_{0.90}Cu_{0.10}O$					
$Zn_{0.90}Cu_{0.10}O$_400	68%		32%	0.12	1.4
$Zn_{0.90}Cu_{0.10}O$_600	79%		21%	0.12	1.4
$Zn_{0.90}Cu_{0.10}O$_800	60%	21%	20%	0.13	1.4

The XP Cu/Zn atomic ratios obtained for all series are higher than the corresponding nominal values (calculated from the weight quantities), suggesting copper segregation on the surface. The introduction of the transition metal ions, does not significantly affect the O/(Cu+Zn) atomic ratio if compared with the corresponding undoped system (table 2).

The results obtained by *X-ray Photoelectron Spectroscopy* are in good agreement with those inferred from *X-ray Diffraction*. The surface composition of $Zn_{1-x}Cu_xO$ systems with $x > 0.01$ revealed the presence of two distinct phases consistent with ZnO and CuO. Samples with a lower concentration of copper, instead, show substantial retention of the dominant wurtzite-like ZnO structure with the dopant occupying substitutional sites.

The annealing temperature, as in the all other cases, is capable of controlling the ratio between lattice oxygen and hydroxyl on the surface of the nanoparticles. This effect seems to remain unaffected by the presence of the dopant, in good analogy with the former transition metal doped samples.

2.4. Summary and Conclusion

Control of the size and morphology of nanometer- or micrometer-scale ZnO crystals represents a great challenge in realising the design of novel functional devices. This is because the magnetic and electronic properties of ZnO crystals, which determine practical applications, can be easily manipulated by varying their size and morphology.

Sol gel synthesis is a method in which the parameters involved are numerous and, if properly controlled, can actually help to obtain materials with desirable characteristics in terms of composition, structure and morphology. Doping with transition metal ions, such as manganese, cobalt and copper, also offers an effective method to adjust the electrical, magnetic, and optical properties of zinc oxide.

In this chapter, the optimised synthetic condition to obtain $Zn_{1-x}TM_xO$ (TM = Mn, Co, Cu) nanopowders with controlled composition, structure and morphology was reported. The obtained nanostructured ZnO based powders were then characterised with different techniques to determine the evolution of the system upon varying the synthesis conditions.

The annealing conditions are also a key parameter in controlling the composition, microstructure and the dimensions of the final nanoparticles. From XRD data it is possible to measure the average diameter of $Zn_{1-x}TM_xO$ powders: nanocrystallites with an average size of a few tens of nanometers (20 nm) are obtained at 400°C while at 800°C the average size increases up to ~ 100 nm; the main particle size of samples annealed at 600°C, an intermediate temperature, is of about 50 nm. These results are in good agreement with SEM images taken for undoped ZnO.

Furthermore, by varying the annealing temperature it is also possible to manipulate the ratio between lattice oxygen and hydroxyl groups on the nanoparticles. This effect can be traced back to the evolution of the *O1s* photoelectron spectra detected by XP spectroscopy and it seems to remain unaffected by the presence of the transition metal ion dopants used.

The properties of the $Zn_{1-x}TM_xO$ system change depending on the nature and the concentration of the dopant. The solubility in the ZnO-wurtzite structure of both cobalt and manganese seems to be higher than that of copper. In fact in the XRD data it is possible to correlate the formation of secondary phases with an increase in dopant concentration, which is confirmed by XPS measurements. Cobalt and manganese doped

systems show the presence of Co_3O_4 and $ZnMnO_3$ respectively in powders containing high concentrations of transition metal ions (x = 0.10). In the case of copper, however, a secondary phase of CuO is formed at lower dopant concentration (x > 0.01).

Wet chemical synthesis, such as *Sol gel*, is expected to provide good control over chemical homogeneity and morphology at an atomic level. This seems to be confirmed by the conventional characterisation described in this chapter: in $Zn_{1-x}TM_xO$ nanopowders with low dopant content the transition metal ions seem to be dispersed in the ZnO matrix occupying substitutional Zn sites. Nevertheless, investigations of the local environment of these nanoparticles, such as *X-ray Absorption Spectroscopy* that will be presented in the next chapter, will provide a better understanding and interpretation of the local structure of the $Zn_{1-x}TM_xO$ materials.

References:

[1] C.J. Brinker, G.W. Scherer, *Sol-Gel Science–The Physics and Chemistry of Sol-Gel Processing*, Academic Press, New York (1990)

[2] L.L. Hench, J.K. West, *Chem. Rev.* **90** (1990) 33

[3] L.E. Scriven, *Better Ceramics Through Chemistry III*, Brinker C.J., Clark D. E., Ulrich D. R., eds., Materials Research Society, Pittsburgh, USA (1988)

[4] D.E. Bornside, C.W. Macosko, L.E. Scriven, *J. Imaging Tech.* **13** (1987) 122

[5] K.D. Kefeer, *Better Ceramics Through Chemistry*, Brinker C.J., Clark D.E., Ulrich D.r., eds, North-Holland, New York, USA (1984)

[6] U. Schubert, Hüsing, *Synthesis of Inorganic Materials*, Wiley-VCH Verlag GmbH, (2000)

[7] E.J.A. Pope, J.D. Mackenzie, *J. Non Cryst. Solids* **87** (1986) 185

[8] L. Spanhel, *J Sol-Gel Sci Techn* **39** (2006) 7

[9] M.S. Tokumoto, S.H. Pulcinelli, C.V. Santilli, V. Briois, *J. Phys. Chem. B* **107** (2003) 568

[10] D. Mondelaers, G.Van den Rul H. Vanhoyland, D. D'Haen, M.K. Van Bael, J. Mullens, L.C. Van Poucke, *Materials Research Bulletin* **37** (2002) 901

[11] J. Li, S. Srinivasan, G.N. He, J.Y. Kanga, S.T. Wu, F.A. Ponce, *Journal of Crystal Growth* **310** (2008) 599

[12] Nedelec J. M., *J. Nanomaterials* 36392 (2007)

[13] W.L. Bragg, *The diffraction of X-rays by crystals*, Nobel lecture, September 6 (1922)

[14] H.P. Klug, L.E. Alexander, *X-ray Diffraction Procedures for Polycrystalline and Amorphous Materials*, J. Wiley & Sons, Chicester UK (1954)

[15] http://www.ing.unitn.it/~luttero/maud/

[16] Inorganic Crystal Structure Database, version 2007, Fachinformationszentrum, Karlsruhe, Germany

[17] E. Ruska, *The Development of the Electron Microscope and of Electron Microscopy*, Nobel Lecture, December 8 (1986)

[18] P.J. Goodhew, J. Humphreys, R. Beanland, *Electron Microscopy and Analysis*, 3rd edition, Taylor & Francis, London, UK (2001)

[19] J. Goldstein, D.E. Newbuty, P. Echlin, D.C. Joy, Jr A.D. Romig, C.E. Lyman, C. Fiori, E. Lifshin, *Scanning Electron Microscopy and X-ray Microanalysis*, 3rd edition, Kluwer Academic, New York, USA (2003)

[20] D. Briggs, M.P. Seah, *Practical Surface Analysis*, Wiley & Sons, Chichester, UK (1983)

[21] D.A. Shirley, *Phys. Rev. B* **5** (1972) 4709

[22] J.F. Moulder, W.F. Stickle, P.E. Sobol, K.D. Bomben, *Handbook of X-ray Photoelectron Spectroscopy*, Physical Electronics, J. Chastain (Ed.) Eden Prairie, MN (1992)

[23] Y. Narendar, G.L. Messing, Catal. Today **35** (1997) 247

[24] NIST X-ray Photoelectron Spectroscopy Database, NIST Standard Reference Database 20, Version 3.4 (2003) (Web Version: srdata.nist.gov/xps)

[25] E. Comini, A. Cusma, S. Kaciulis, S. Kandasamy, G. Padeletti, L. Pandolfi, G. Sberveglieri, A. Trinchi, W. Wlodarski, *Surf. Interface Anal.* **38** (2006) 736

[26] N.S. McIntyre, T.C Chan, In *Practical Surface Analysis* (2^{nd} ed.), vol. 1, Briggs D, Seah MP (eds) John Wiley and Sons: Chichester, (1990) pp. 504

[27] K.S. Kim, *Phys. Rev. B* **11** (1975) 2177

[28] N.S. McIntyre, M.G. Cook, *Anal. Chem.* **47** (1975) 2208

[29] H. Purnama, F. Girgsdies, T. Ressler, J.H. Schattka, R.A. Caruso, R. Schomacker, R. Schlogl, *Catal. Lett.* **94** (2004) 61

[30] P.H. Matter, D.J. Braden, U.S. Ozkan, *J. Catal.* **223** (2004) 340

[31] L. Armelao, D. Barreca, M. Bertapelle, G. Bottaro, C. Sada, E. Tondello, *Thin Solid Films* **442** (2003) 48

[32] G. Panzner, B. Egert, H.P. Schmidt, *Surf. Sci*. **151** (1985) 400

Chapter 3

Local Geometry and the Electronic Structure: X-ray Absorption Spectroscopy (XAS) Electron Paramagnetic Resonance (EPR)

PART 1. X-ray Absorption Spectroscopy (XAS)

3.1. Introduction

In the extensive field of X-ray diagnostic techniques, nowadays mostly implemented on synchrotron X-ray sources, X-ray absorption methods offer a relatively simple tool for structural analysis of materials[1-6].

The main advantages of *X-ray Absorption Spectrometry* (XAS) methods are the insensitivity to the long-range order and the sensitivity to the chemical species. XAS probes the immediate neighbourhood of the atomic species chosen by the energy of its absorption edge: the depth of probing may be somewhat greater in ordered materials but useful results are also obtained from amorphous samples. The strong sensitivity to first neighbours makes XAS the tool of choice for coordination chemistry and the chemistry of catalysts and other nanostructures.

3.1.1 Technique

X-ray Absorption Spectroscopy (XAS) concerns the study of electronic transitions from inner shells to unoccupied states. Electronic and structural information on selected absorbing sites can be obtained in complex systems by tuning the X-ray energy of the

beam incident on the sample. In this way the atomic species under investigation can be selected and its environment explored. The absorption coefficient shows a somewhat pronounced oscillatory structure as a function of the photon energy above the rising edge. This structure reflects the presence of neighbours around the absorbing atom. Because of the finite lifetime of the photoelectron in the final state the shape of the absorbing spectra depends mainly on the geometrical structure of a finite cluster of atoms around the photo-absorber. The size of this cluster changes with the systems under study, ranging from a single shell to several shells.

Below there is a brief description of how this technique can be used in the characterisation of semiconductor nanomaterials. More details can be found in the literature[1-6].

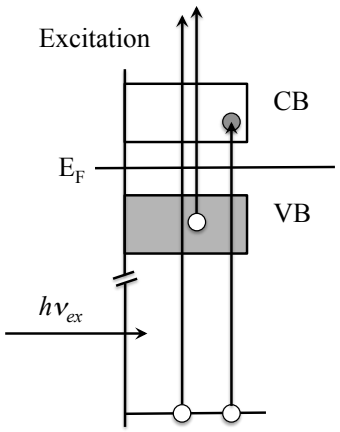

Figure 1: Schematic for XAS.

Figure 1 shows the absorption of an X-ray photon when there is sufficient energy to excite the core electron into the bottom of the conduction band (CB) via dipole transition. As the photon energy continues to increase when it is tuned across the edge core electron excitation threshold, the core electron will continue to probe the unoccupied densities of states (DOSs) in the CB and above.

These transitions are sensitive to the chemical environment of the absorbing atom band structures in solids, resulting in a change in the atomic absorption coefficient. Thus, the XANES region probes primarily the DOS of the CB in semiconductors accessible by $\Delta l = \pm 1$ selection rules (l: angular momentum, e.g., $s \rightarrow p$; $p \rightarrow s,d$; …). The absorption (μt, where μ is the linear absorption coefficient and t is the thickness) is proportional to the square of the matrix element which couples the initial state wave function ψ_i (core electron, e.g., *1s* orbital for the *K* shell) to the final state wave function ψ_f (e.g., CB state with $\Delta l = \pm 1$ character) via dipole transition. Thus within the single particle approximation, XANES probes the unoccupied DOS above the Fermi level such that (Fermi's golden rule)

$$\mu t \propto \left|\langle \psi_i | r | \psi_f \rangle\right|^2 \rho(DOS)$$

Thus, in principle, the XANES results can be compared with DOS obtained from band structure calculations.

X-ray Absorption Spectroscopy (XAS) generates a spectrum in which it is possible to identify three main regions, as shown in figure 2.

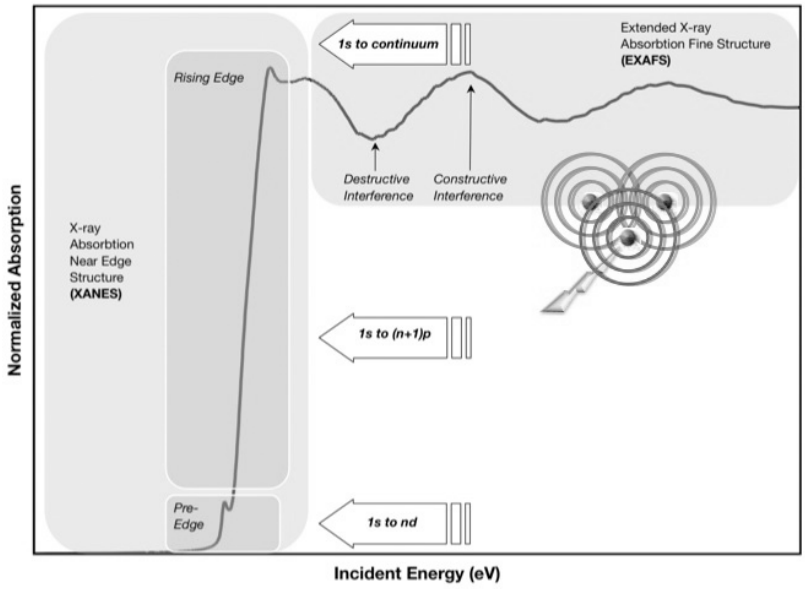

Figure 2: Schematic of a generic XAS spectrum.

The dominant feature is called the "rising edge", and is sometimes referred to as XANES (*X-ray Absorption Near-Edge Structure*) or NEXAFS (*Near-Edge X-ray Absorption Fine Structure*). The pre-edge region is at energies lower than the rising edge. The EXAFS (*Extended X-ray Absorption Fine Structure*) region encompasses energies above the rising edge, and corresponds to the scattering of the ejected photoelectron off neighbouring atoms. The combination of XANES and EXAFS is referred to as XAFS.

X-ray absorption spectra are usually produced over the range of 200 – 35,000 eV. The dominant physical process is one where the absorbed photon ejects a core photoelectron from the absorbing atom, leaving behind a core hole. The atom with the core hole is now excited. The ejected photoelectron's energy will be equal to that of the absorbed photon minus the binding energy of the initial core state. The ejected photoelectron interacts with electrons in the surrounding non-excited atoms. If the ejected photoelectron is taken to have a wave-like nature and the surrounding atoms are described as point scatterers, it is possible to imagine the backscattered electron waves interfering with the forward-propagating waves. The resulting interference pattern shows up in the measured absorption coefficient, causing the oscillation seen in the EXAFS spectra. The wavelength of the photoelectron is dependent on the energy and phase shift between the initial and scattered waves. The wavelength also changes as a

function of the energy of the incoming photon. The phase and amplitude of the backscattered wave are dependent on the type of atom doing the backscattering and the distance of the backscattering atom from the central atom. The dependence of the scattering on atomic species makes it possible to obtain information pertaining to the chemical coordination environment of the original absorbing (centrally excited) atom by analysing these EXAFS data.

3.1.2 Experimental

XAFS experiments at the O K-edge, Zn $L_{3,2}$-edge, Mn $L_{3,2}$-edge, Co $L_{3,2}$-edge and Cu $L_{3,2}$-edge were performed on the Spherical Grating Monochromator (SGM) 11ID-1 beam-line (energy: 200-1900 eV, $\Delta E/E$: $<10^{-4}$) at the Canadian Light Source (CLS), University of Saskatchewan.

XAFS at the Zn, Mn, Co and Cu K-edges were performed on the Pacific Northwest Consortium X-ray Operation Research (PNC-XOR) Bending Magnet (BM) 20-BM beam-line (energy: 2400–29 000 eV, $\Delta E/E$: 1.4 x 10^{-4}) at the Advanced Photon Source (APS), Argonne National Laboratory.

3.2. Undoped ZnO

As described above, XANES probes the local structure and bonding of the absorbing atom and can provide information on oxidation state, coordination, and symmetry of the system.

For a better understanding of different $Zn_{1-x}TM_xO$ systems, it is fundamental to first describe the structure of the undoped ZnO as a function of the processing temperature. Accordingly, in this section the XANES structures at the O *K*-edge, and Zn $L_{3,2}$-edges, will be presented.

3.2.1 O K-edge

The O *K*-edge XANES spectra (figure 3a) show the oxygen $1s \rightarrow 2p$ dipole transition.

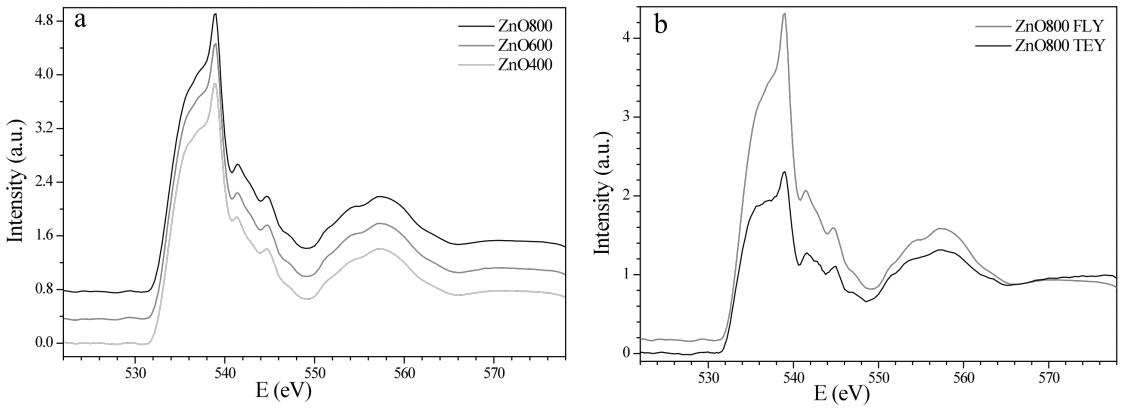

Figure 3: O K-edge XANES spectra of ZnO samples: **a)** TEY and **b)** TEY vs. FLY.

For all samples it is possible to identify an intense shoulder peak at 535 eV and main peak at 539 eV. These signals result from the $O1s \rightarrow 2p_z$ and $O1s \rightarrow 2p_{x,y}$ transitions in ZnO respectively[7]. This splitting of the transition is due to the anisotropy of the hexagonal (wurtzite) ZnO crystal structure.

Looking at the sample treated at 800°C, the increase in intensity of the 539 eV peak can be related to an increase in the crystallinity of the ZnO[8].

Figure 3b shows the difference in main peak intensities between the FLY (*Fluorescent Yield*) and TEY (*Total Electron Yield*). This is due to self-absorption of the fluorescent signal by the ZnO as the thickness of the powder is very close to the attenuation length above the O *K*-edge (~200 nm)[9]. Hereafter, when not otherwise specified, all spectra will be reported in TEY.

3.2.2 Zn $L_{3,2}$-edge

Figure 4 shows the Zn $L_{3,2}$-edge spectra involving the zinc $2p \rightarrow 4s,3d$ dipole transition.

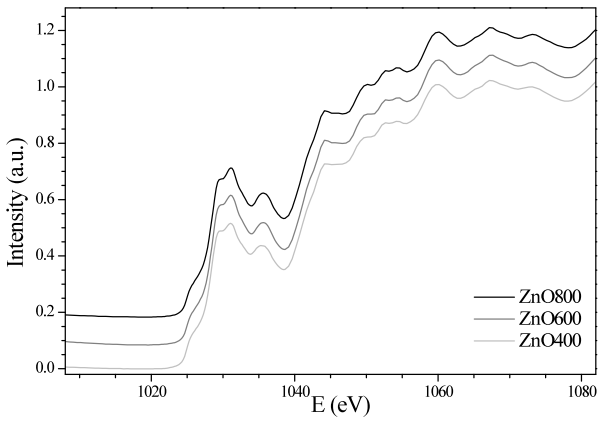

Figure 4: Zn $L_{3,2}$-edge XANES spectra of ZnO samples.

These results indicate the presence of a hexagonal (wurtzite) ZnO crystal structure (i.e. Zn in a tetrahedral coordination to O)[6,7]. The features of the three spectra are virtually identical revealing that the processing temperature does not affect the local environment of zinc. The Zn *K*-edge (not shown) confirms the presence of wurtzite phase and shows the same trend.

3.3 $Zn_{1-x}Mn_xO$

In this section XAS results for the series of nanopowders doped with manganese ($Zn_{1-x}Mn_xO$) will be reported.

This will help provide information on the electronic structure of the system as well as the oxidation state, chemical environment and coordination of the dopant. Furthermore, the spectra will be analysed in terms of manganese content and processing temperature to identify the evolution of the system upon changing the synthetic conditions.

3.3.1 O *K*-edge

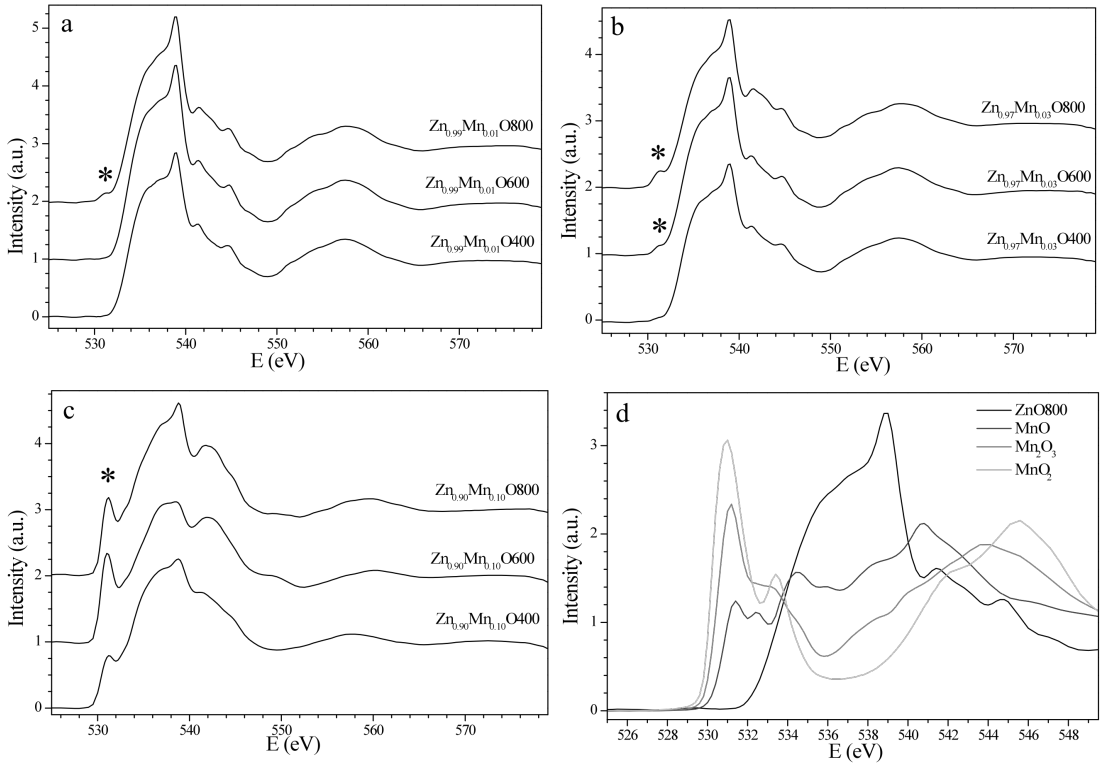

Figure 5: O *K*-edge XANES spectra of **a)** $Zn_{0.99}Mn_{0.01}O$ **b)** $Zn_{0.97}Mn_{0.03}O$ **c)** $Zn_{0.90}Mn_{0.10}O$ **d)** MnO (cubic – O_h Mn), Mn_2O_3 (spinel – O_h Mn), MnO_2 (rutile – O_h Mn) standards and ZnO800 sample.

In figure 5 (section a, b and c) O *K*-edge XANES spectra for the system $Zn_{1-x}Mn_xO$ as a function of the manganese content and the processing temperature are reported. Figure 5d shows the spectra of manganese oxides used as standards in the identification of the oxidation state and coordination of the dopant, as well as the presence of secondary phases.

$Zn_{0.99}Mn_{0.01}O$ processed at 400 ºC and 600 ºC, as well as $Zn_{0.97}Mn_{0.03}O$_400, have O *K*-edge XANES spectra with virtually identical features to that of pure ZnO. They greatly resemble the model spectrum described in literature[10], obtained with the assumption of tetrahedral Mn^{2+} substituting in Zn vacancies with compensating Zn vacancies in the crystal lattice ($Mn_{Zn}+V_{Zn}$)

The pre-edge shoulder at 532 eV (denoted with asterisks in all sections of figure 5) is present in systems where manganese no longer has a purely substitutional (Zn vacancy) role and is forming an oxide complex with a lower binding energy. That secondary phase formation can be identified in $Zn_{0.99}Mn_{0.01}O$_800, $Zn_{0.97}Mn_{0.03}O$ treated above 600°C and all $Zn_{0.90}Mn_{0.10}O$ samples.

From the location and shape of the pre-edge feature, the secondary phase could be related to the presence of oxygen bound to either Mn^{3+} or Mn^{4+} (figure 5d). The intensity of this pre-edge feature can be used as an indication of the quantity of secondary phase formed.

3.3.2 Zn $L_{3,2}$-edge

The Zn $L_{3,2}$-edge XANES spectra for all $Zn_{1-x}Mn_xO$ samples are shown in figure 6a.

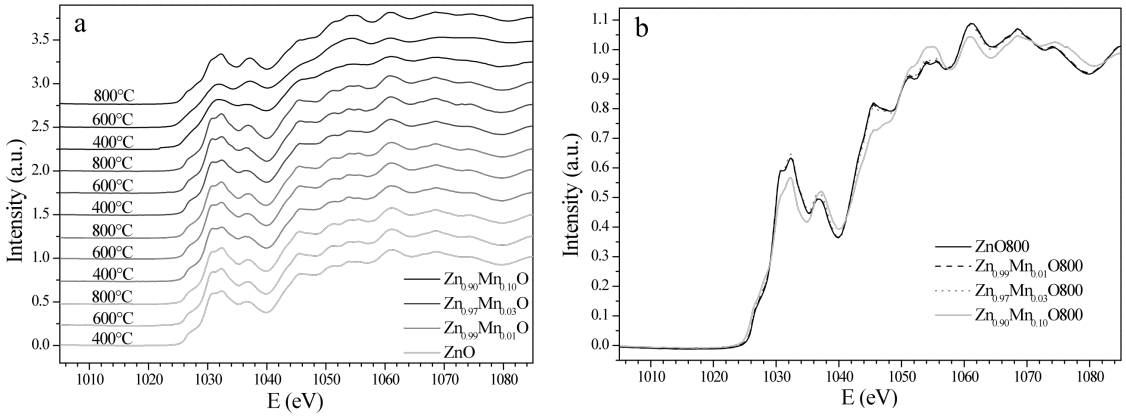

Figure 6: Zn $L_{3,2}$-edge XANES spectra of $Zn_{1-x}Mn_xO$ system.

Independent of manganese concentration and processing temperature, there is no change in the absorption edge E_o, or the location of features in the XANES spectra. This indicates that ZnO is present in all systems.

In figure 6b it can clearly be seen, however, that features in the fine structures at the Zn $L_{3,2}$-edge become smoothed with increasing manganese content ($Zn_{0.90}Mn_{0.10}O$ series). This loss of features reveals an increase in the overall disorder of the system resulting from the formation of a secondary phase in the ZnO matrix. The secondary phase contains Zn in the form of a mixed oxide Zn-O-Mn, most likely $ZnMnO_3$ as indicated by the XRD data. If this the case, the local environment of some Zn sites would change from a tetrahedral (in ZnO) to an octahedral coordination (in $ZnMnO_3$) resulting in the combinatorial Zn $L_{3,2}$-edge XANES spectra seen in figure 6b.

3.3.3 Mn *K*-edge

Figure 7a shows the Mn *K*-edge XANES spectra for all Mn doped ZnO, incorporating the dipole transition from *1s→np*.

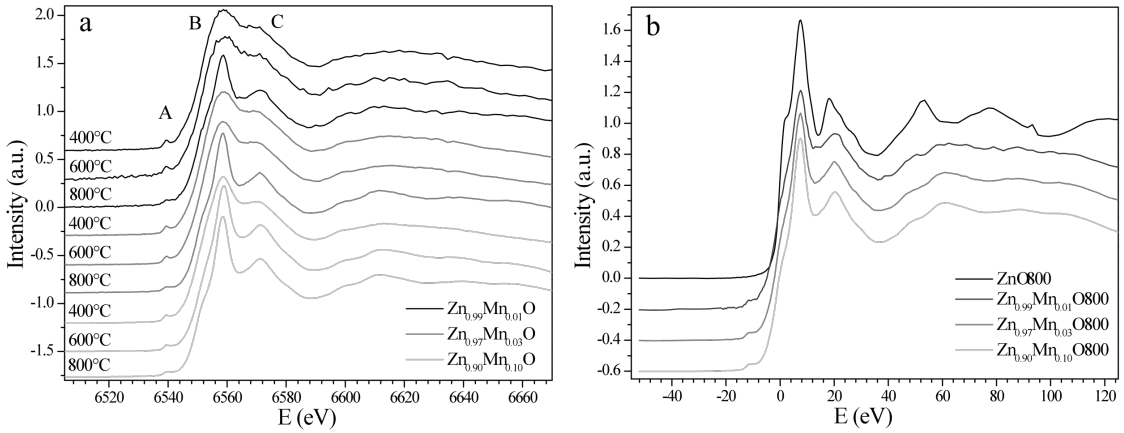

Figure 7: a) Mn K-edge XANES spectra **b)** Zn and Mn K-edge spectra at E_o=0 for $Zn_{1-x}Mn_xO$ systems.

It is possible to identify three different peaks (denoted in the figure as A, B, and C). Their position is not affected by synthetic conditions such as the content of manganese or the processing temperature. However, with increasing processing temperature the peaks do sharpen, which can be ascribed to an increase in cystallinity.[8]

All spectra resemble the Zn *K*-edge of ZnO seen in Figure 7b (only samples treated at 800 ºC are shown). The manganese is in a similar environment independent of its content and it substitutes for Zn in the ZnO lattice as $Mn_{Zn}O$. Previous studies of the Mn *K*-edge have used these results to suggest that the manganese is substitutional for the zinc and no secondary phases are present[10,11,12].

Close examination of the small pre-edge located at 6540 eV (peak A) may nevertheless reveal the presence of a secondary phase. This signal is a forbidden *s→d* quadrupole transition: dipole selection rules do not allow this kind of excitation and its observation is associated with the existence of *p-d* hybridization. This in turn is possible only if the manganese site does not contain an inversion centre, as is present in a tetrahedral configuration such as $Mn_{Zn}O$, or when there is sizeable local distortion[13]. Increasing the processing temperature up to 800°C, the intensity of this particular transition decreases: some of the manganese converts from a tetrahedral geometry to an octahedral geometry and a secondary phase, such as cubic $ZnMnO_3$, could be forming.

3.3.4 Mn $L_{3,2}$-edge

A better way of evaluating the formation of a secondary phase is by studying the Mn $L_{3,2}$-edge (figure 8) involving the *2p→nd,(n+1)s* transitions.

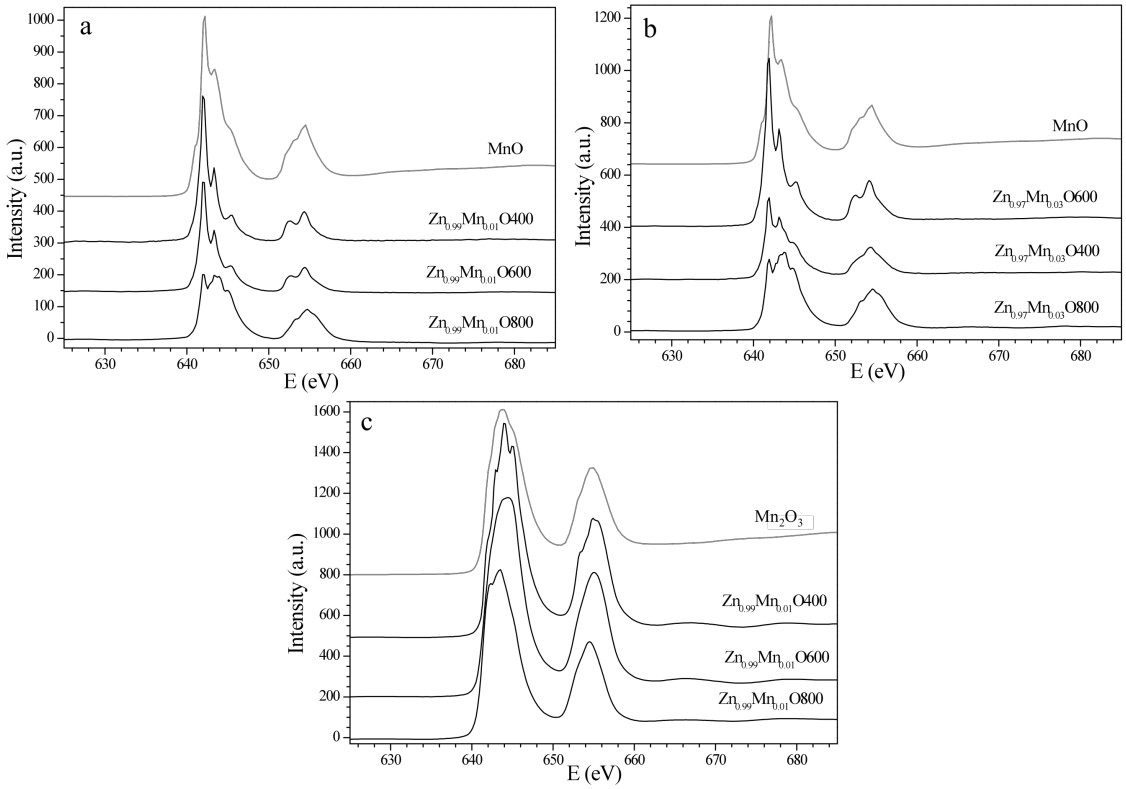

Figure 8: Mn $L_{3,2}$-edge XANES spectra of $Zn_{1-x}Mn_xO$ system.

Signs of secondary phase formation are very evident even at the lowest manganese content for the $Zn_{0.99}Mn_{0.01}O$ series (figure 8a): the phenomenon seems to be temperature dependent as samples processed at 400ºC and 600ºC do not show signs of the secondary phases present after treatment at 800ºC. A similar trend can be seen for

the $Zn_{0.97}Mn_{0.03}O$ series: this time, the secondary phase formation is evident in samples treated at 600ºC and 800ºC, but not when processed at 400ºC. Finally, all spectra of $Zn_{0.90}Mn_{0.10}O$ series (figure 8c) show the coexistence of two phases independent of the processing temperature.

The onset of secondary phase seen in the Mn $L_{3,2}$-edge XANES (figure 8) correlates well with the increase in the pre-edge peak seen in the O *K*-edge XANES (figure 5) and the decrease of the pre-edge peak seen in the Mn K-edge spectra (figure7).

Manganese is first incorporated into the ZnO wurtzite matrix as $Mn_{Zn}O$ (figure 6a-b). The oxidation state of the metal is Mn^{2+}, however its coordination is different than in MnO (high spin, coordination number of 6, O_h Mn) as shown in the relative peak intensities. It is possible to ascribe it to $Mn_{Zn}O$ (high spin, coordination number of 4, T_d Mn) as described in the literature[14].

Increasing both dopant concentration and processing temperature the manganese is oxidised to a state similar to that in Mn_2O_3 as seen in figure 6c. The change in manganese valency from 2+ to 3+ and 4+ is frequently seen in the shift to higher binding energy and a decrease in the L_3 to L_2 peak ratios[14-17]. Although it is difficult to distinguish the presence of the Mn^{4+} required for $ZnMnO_3$ and therefore to absolutely confirm the XRD data. The main trend of the XAS data is, however, in good agreement with the diffraction ones.

3.4 $Zn_{1-x}Co_xO$

In this section, in a similar fashion to the previous one, the XAS data of the Co-doped series ($Zn_{1-x}Co_xO$) will be presented.

These measurements are very useful for determining the valence state and local structure of Co in doped ZnO systems[18-22]. Since XAFS does not require long-range crystalline order, secondary phase components can be detected even if they are disordered or in small clusters[19,23-25]. Spectra will also be analysed in terms of cobalt content and processing temperature to identify the evolution of the system upon changing the synthetic conditions.

3.4.1 O *K*-edge

Figure 9 shows the O *K*-edge XANES spectra for $Zn_{1-x}Co_xO$ as well as ZnO and Co_3O_4 standards.

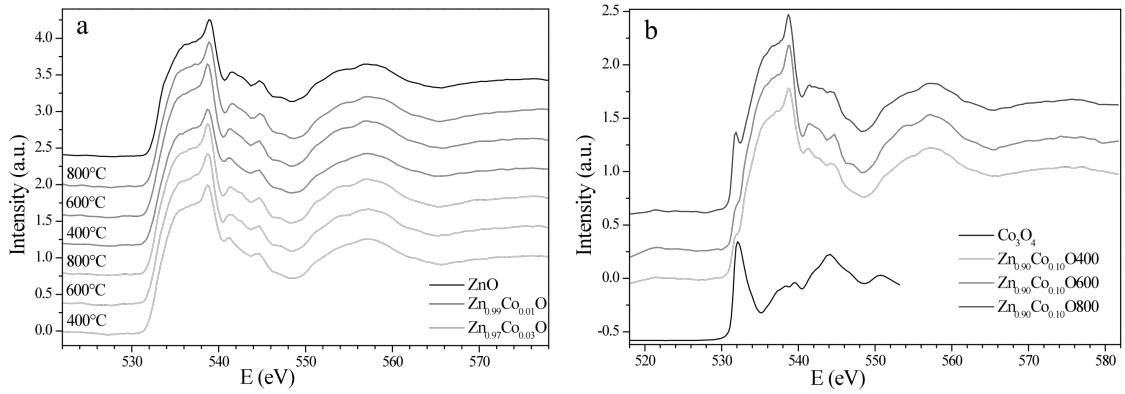

Figure 9: O K-edge XANES spectra for $Zn_{1-x}Co_xO$ series.

All samples show a well defined shoulder from 532-538 eV and an intense peak at ~539 eV which can be assigned to the transition of the *O1s* electron to the unoccupied $O2p_z$ and the $O2p_{x,y}$ states in the conduction band due to the anisotropy of the wurtzite crystal structure respectively[7]. Furthermore, transitions to the *O3p* and *O4p* states and the *O2p* states hybridised with *Zn4p* and *Co4p* states are located in the region between 540 eV and 550 eV[26].

The spectral shape of the $Zn_{1-x}Co_xO$ samples with $x < 0.1$ exhibits almost identical features to that of pure ZnO, as can be seen in figure 9a. On increasing the cobalt content (samples with $x = 0.1$, figure 9b), a strong pre-edge peak at ~532 eV is quite evident: this can be attributed to the formation of Co_3O_4 secondary phases in the system.

Yao et al.[27] have previously suggested that this pre-edge region around 532 eV arises from hybridised states in the band-gap: due to the d^{10} configuration of Zn atoms, the O *K*-edge of the undoped ZnO does not show any sharp features related to the *O2p – Zn3d* hybridised orbital. Whereas, when Co substitutes for Zn in the ZnO, the sharp pre-edge peak is attributed to the partially occupied *Co3d* states and the strong hybridization between *Co3d* states and *O2p* states[27]. If this were the case, the strong pre-edge peak would also appear in the other series with lower cobalt content.

Furthermore, as shown clearly in figure 9b, the pre-edge position is compatible with the presence of a Co_3O_4 secondary phase. Finally, increasing the processing temperature causes the intensity of this peak to increase. All these considerations are in good agreement with XRD data: the formation of the secondary phase is detectable in the series $Zn_{0.90}Co_{0.10}O$ and the phenomenon is temperature dependent.

3.4.2 Zn $L_{3,2}$-edge

The Zn $L_{3,2}$-edge XANES spectra, involving the *2p→nd,(n+1)s* dipole transition is shown in figure 10.

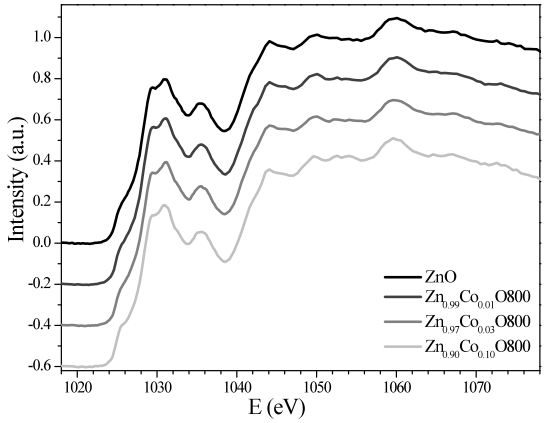

Figure 10: Zn $L_{3,2}$-edge spectra for samples $Zn_{1-x}Co_xO$_800.

The features of these spectra are mostly the same for all the $Zn_{1-x}Co_xO$ samples (powder treated below 800°C are not shown), revealing that the local environment of the zinc does not change. This is a good indication that any secondary phase which forms either does not contain Zn, as in Co_3O_4 spinel, or does not change the local environment of the zinc, which is tetrahedrally bonded to oxygen, such as in the spinel $Zn[Co_2O_4]$ structure.

3.4.3 Co *K*-edge

Figure 11a reports the Co *K*-edge XANES spectra of the $Zn_{1-x}Co_xO$ system. The whiteline peak at ~7725 eV corresponds to the dipole transition from the Co *1s→np*.

All samples, independent of cobalt content and processing temperature, display a small pre-edge peak at ~7708 eV. This can be attributed to the Co *1s→3d,4s* quadrupole transition which results from the substitution of zinc vacancies, leaving the cobalt in a tetrahedral environment. The lack of an inversion centre in the $Co_{Zn}O$ local environment allows the forbidden quadrupole transition to occur.

Samples $Zn_{1-x}Co_xO$ with $x < 0.1$ have a Co *K*-edge XANES that resembles the Zn *K*-edge in the undoped ZnO as shown in figure 11b. This indicates that cobalt and zinc share a similar local environment (i.e. tetrahedral coordination to O).

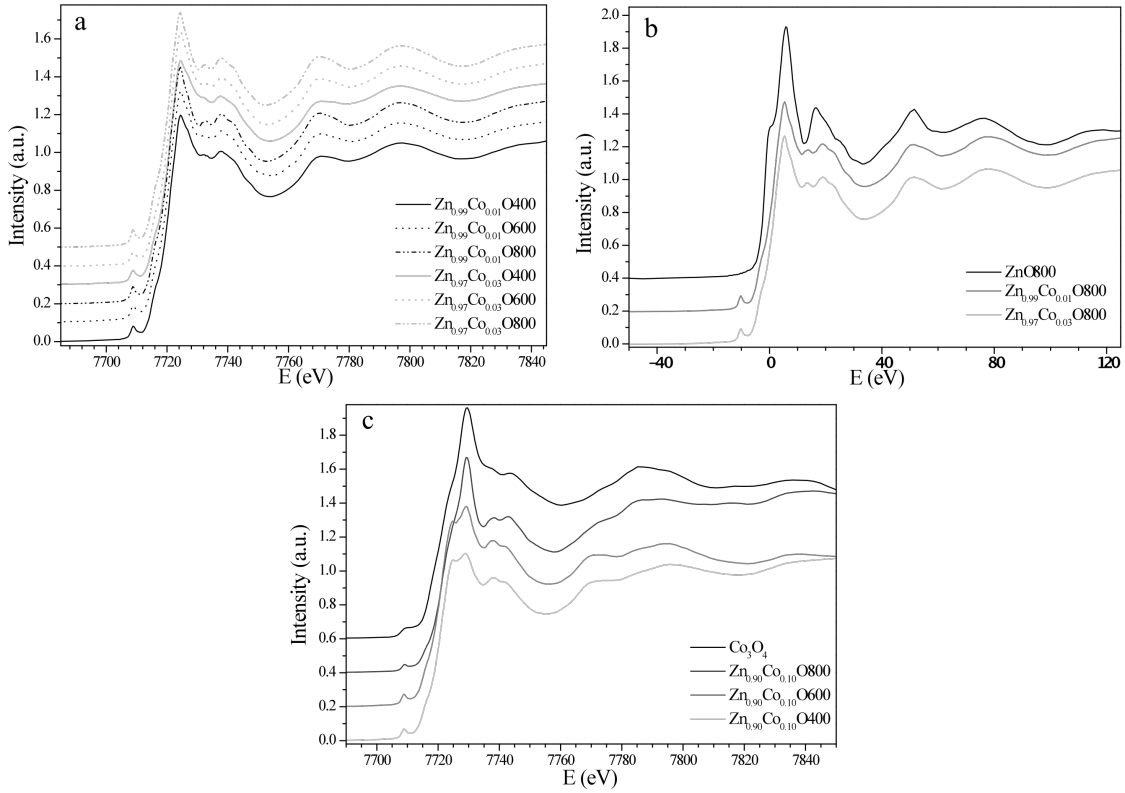

Figure 11: Co K-edge XANES spectra for $Zn_{1-x}Co_xO$ series. Section b shows Zn and Mn K-edge spectra at E_o=0.

The $Zn_{0.90}Co_{0.10}O$ series show an additional feature at ~7730 eV which corresponds to the formation of Co_3O_4 clusters in the system (figure 11c). Increasing the processing temperature, the relative intensity of this signal increases while the pre-edge peak decreases in size: the incorporation of cobalt into Co_3O_4 arises in the series with higher dopant content and is temperature dependent.

3.4.4 Co $L_{3,2}$-edge

A similar trend to that of the Co and O *K*-edge is seen at the Co $L_{3,2}$-edge: the presence of Co_3O_4 secondary phase is detectable only for the series $Zn_{0.90}Co_{0.10}O$.

Again, samples with cobalt content below 10%at. all have mostly identical XANES spectra, which are similar in peak position to that of CoO (figure 12a shows only spectra of samples treated at higher temperature). The L_3 and L_2-edges have their whiteline dipole transition from $Co2p_{3/2}$, $Co2p_{1/2}$ to unoccupied *Co3d* states at ~781 eV and ~796 eV respectively. However, the relative peak intensities are different and it is possible to relate this with a change in the crystal field from the octahedral environment of cobalt in CoO to the tetrahedral environment that it has in $Co_{Zn}O$.

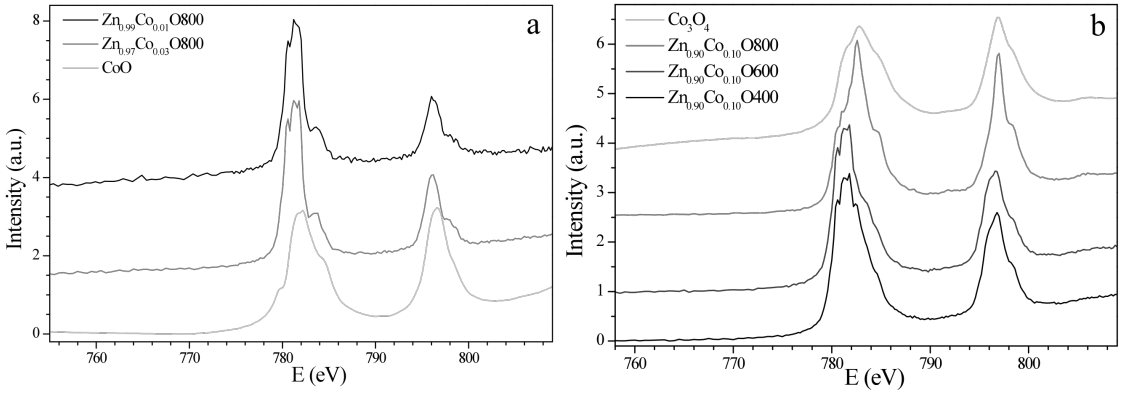

Figure 12: Co $L_{3,2}$-edge XANES spectra for $Zn_{1-x}Co_xO$ series.

The $Zn_{0.90}Co_{0.10}O$ series display Co $L_{3,2}$-edge XANES spectra which differ from those with a lower dopant concentration as shown in figure 12b. It is possible to denote a decrease in the two main peaks at ~781 eV and ~796 eV. Furthermore, two shoulders become visible at ~783 eV and ~798 eV: upon increasing processing temperature the intensities of these shoulders increase. Finally, in sample $Zn_{0.90}Co_{0.10}O\_800$, the XANES spectrum resembles that of Co_3O_4.

It is worth noticing that there is a difference in peak intensities at ~783 eV and ~798 eV between the sample and the standards. It is possible to attribute this effect to the small size of the Co_3O_4 clusters in the system: nanomaterials with smaller dimensions have been shown to have more discrete energy levels and sharper features in XANES[8].

3.5 $Zn_{1-x}Cu_xO$

XAS data of the $Zn_{1-x}Cu_xO$ (x = 0.005, 0.01, 0.05 and 0.1) series will be presented in this section. As for the other dopants, spectra will be analysed in terms of copper content and processing temperature to identify the evolution of the system with changing synthetic conditions.

As this specific system will be tested as a catalyst for the steam reforming of methanol, it is very important to be able to distinguish between bulk and surface composition. For that reason both FLY (*Fluorescent Yield*) and TEY (*Total Electron Yield*) spectra will be presented. The FLY, with the larger escape depth of X-rays, mainly contains information regarding the bulk of the compound. On the other hand, the TEY, with the shorter escape depth of electrons, mainly contains information about the surface of the system.

3.5.1 O K-edge

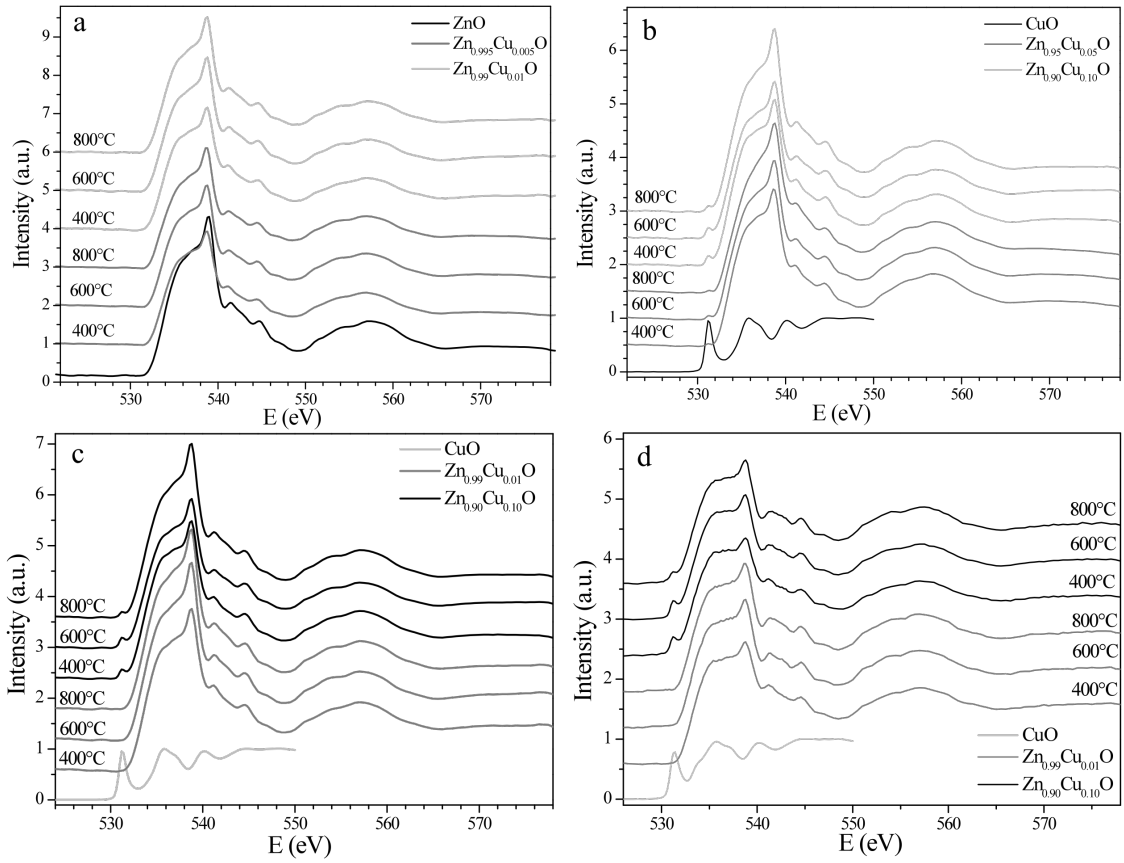

Figure 13: O K-edge of $Zn_{1-x}Cu_xO$ series of compounds **a)** TEY spectra, x = 0.005 and 0.01 **b)** TEY spectra, x = 0.05 and 0.10 **c)** TEY spectra, x = 0.01 and 0.10 **d)** FLY spectra x = 0.01 and 0.10.

The O *K*-edge XANES spectra, recorded in both TEY and FLY (figure 13) show features due to the oxygen *O1s→O2p* dipole transition.

As seen for the undoped samples, the intense shoulder peak at 535 eV and main peak at 539 eV result from the $O1s \rightarrow O2p_z$ and $O1s \rightarrow O2p_{x,y}$ in ZnO respectively[7]; increasing processing temperature, there is an increase in intensity of the 539 eV peak which can be attributed to an increase in the crystallinity of the system[8]. Finally the difference in main peak intensities between the FLY and TEY is due to self absorption of the fluorescent signal by the ZnO as the thickness of the powder is very close to the attenuation length above the O K-edge (~ 200 nm)[9].

Samples with low copper content, $Zn_{1-x}Cu_xO$ with x = 0.005 and 0.01, have an O *K*-edge XANES that resemble the one of the undoped sample, as shown in figure 13a. This indicates that the oxygen is in a very similar local environment to that in the undoped samples and the copper is incorporated in the matrix as $Cu_{Zn}O$.

Instead, the pre-edge peak at ~532 eV seen in the samples with x = 0.05 and 0.1 (figure 13b) corresponds to the *O1s → 3eg* transition in CuO[28,29]. The $3e_g$ orbital results from the hybridisation of the *O2p* and *Cu3d* states and is only partially filled due to the d^9 configuration of Cu^{2+} in CuO.

To compare bulk and surface properties of $Zn_{1-x}Cu_xO$ with x = 0.001 and 0.10 figure 13c shows the TEY spectra while figure 13d reports the FLY spectra. The FLY has a more intense pre-edge feature than the TEY indicating that the bulk has a larger CuO:ZnO ratio than the surface. This pre-edge feature decreases in intensity for the sample treated at 800ºC indicating a conversion of the second phase of CuO into $Cu_{Zn}O$.

3.5.2 Zn $L_{3,2}$-edge

The Zn $L_{3,2}$-edge spectra, shown in figure 14, involve the *Zn2p →Zn4s,3d* dipole transition. The Zn $L_{3,2}$-edge peak shows no difference between samples containing copper and the undoped ZnO. Independent of the Cu concentration and the processing temperature (only samples treated at 800°C are reported in the figure), the zinc does not change its local environment.

These results indicate that all samples contain only CuO, $Cu_{Zn}O$ and ZnO phases and no other ZnCuO complexes are formed. The Zn *K*-edge (not shown) shows the same trend.

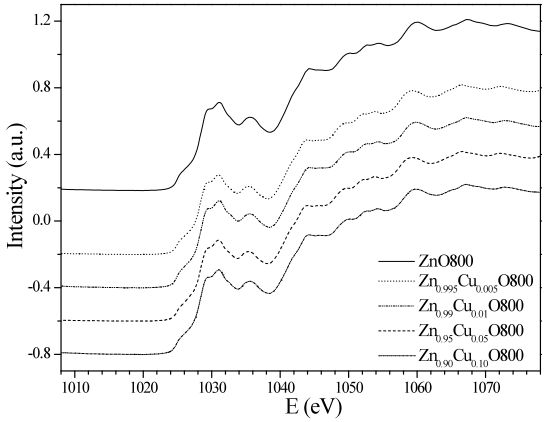

Figure 14: Zn $L_{3,2}$-edge XANES spectra of $Zn_{1-x}Cu_xO$_800 samples.

3.5.3 Cu *K*-edge

Figure 15 shows the Cu *K*-edge XANES spectra that involve the Cu *1s→4p* dipole transition.

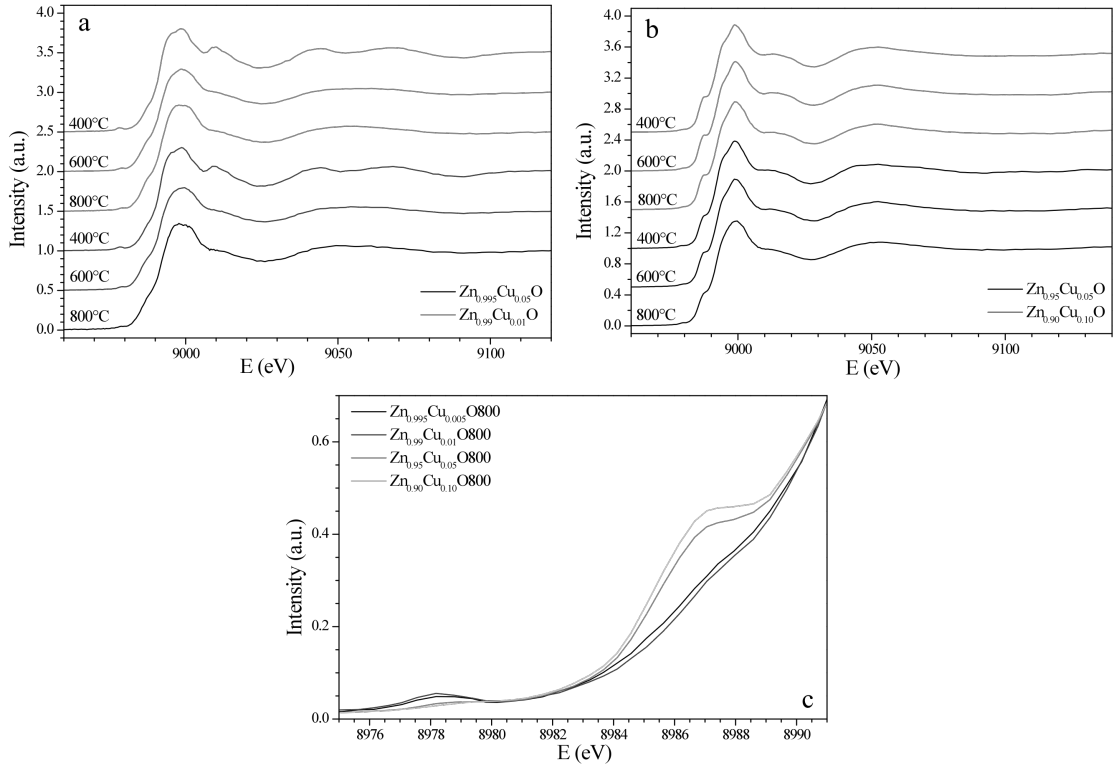

Figure 15: Cu K-edge XANES spectra of $Zn_{1-x}Cu_xO$ samples.

There is a pre-edge peak at ~8978 eV in the $Zn_{1-x}Cu_xO$ samples where $x < 0.05$ (figure 15a) and its intensity increase increasing processing temperature. This pre-edge peak is due to the forbidden Cu *1s→4d* quadrupole transition[30]: the substitution of zinc vacancies leaves the copper in a tetrahedral environment. The lack of an inversion centre in the $Cu_{Zn}O$ local environment allows the forbidden quadrupole transition to occur. Additionally, in $Zn_{1-x}Cu_xO$ samples where $x < 0.05$, processed at 800°C, the XANES spectra has features similar to that of ZnO. These two considerations indicate that the incorporation of copper into zinc vacancies forming $Cu_{Zn}O$ occurs for low dopant concentration and that it is temperature dependent.

As shown in figure 15b, samples $Zn_{1-x}Cu_xO$ containing higher concentrations of copper (with $x = 0.05$ and 0.10) do not display this pre-edge peak at ~8978 eV indicating that the copper has changed local environment. The main peak at ~8995 eV and the shoulder (shake down) peak at ~8987 eV are respectively due to $3d^9$ and $3d^{10}L$ final state electronic configurations in the presence of a core-hole (where L denotes a hole in an *O2p* orbital)[31]. The shake-down peak increases with copper concentration, as shown in figure15c, indicating the formation of a secondary phase of CuO.

Finally, looking carefully at figure 15c, it is possible to follow the formation of the secondary phase of CuO: upon increasing the amount of dopant the shake-down peak increases but at the same time the intensity of the pre-edge signal decreases.

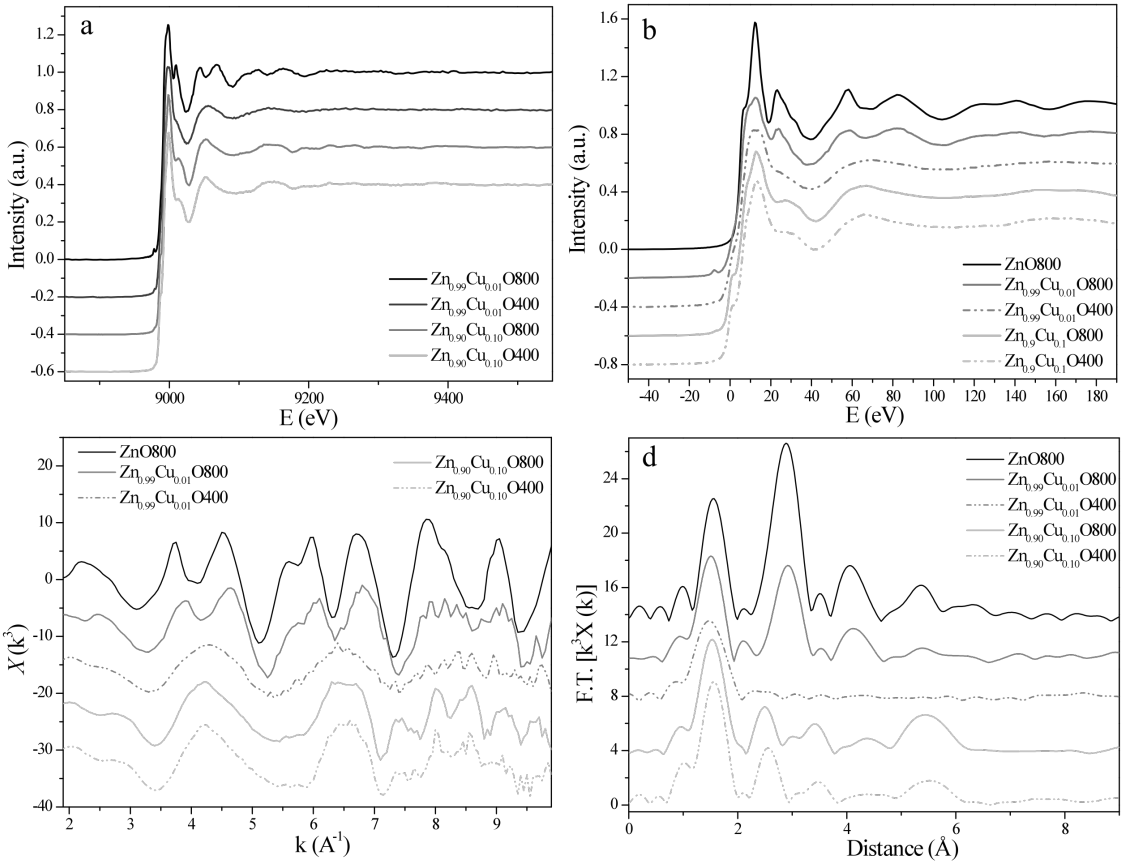

Figure 16: Cu K-edge EXAFS of samples $Zn_{1-x}Cu_xO$ x = 0.01 and 0.1
a) spectra **b)** Zn and Mn K-edge spectra at E_o=0 **c)** *k*-space **d)** and *R*-space.

As seen in figure 16b in $Zn_{0.99}Cu_{0.01}O$_800 the copper exists in the same local environment as the zinc in the undoped ZnO indicating the substitutional incorporation of Cu as $Cu_{Zn}O$. The similarity of both the Cu_{Zn} and Zn can be best seen in identical spectral features of both the *k*-space (Figure 16c) and *R*-space spectra (Figure 16d). For $Zn_{0.99}Cu_{0.01}O$ treated at low processing temperatures, as well as for the series with higher copper content, the Cu exists in a different environment as CuO.

The *R*-space spectrum has not, however, been corrected for phase shift, once this is taken into account, these results are consistent with previous studies on copper doped ZnO systems[32,33]. The lack of long-range order seen in the *R*-space spectrum of $Zn_{0.99}Cu_{0.01}O$_400 is both due to the small amount of the dopant in the system and the very small particle size.

3.5.4 Cu $L_{3,2}$-edge

In figure 17 the Cu $L_{3,2}$-edge spectra of the $Zn_{1-x}Cu_xO$ series in both TEY (sections a and c) and FLY (sections b and d) are reported.

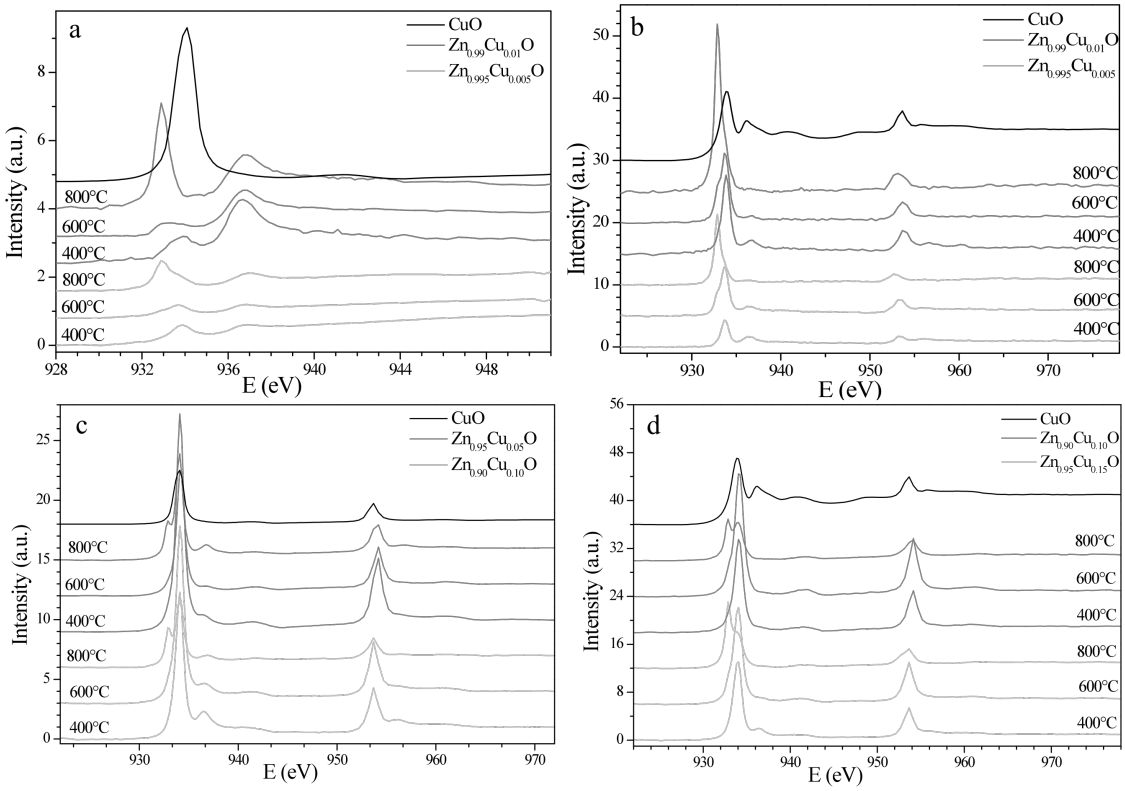

Figure 17: Cu $L_{3,2}$-edge of $Zn_{1-x}Cu_xO$ series of compounds **a)** TEY spectra, x = 0.005 and 0.01 **b)** FLY spectra, x = 0.005 and 0.01 **c)** TEY spectra, x = 0.05 and 0.10 **d)** FLY spectra x = 0.05 and 0.10.

The Cu $L_{3,2}$-edge spectra show the Cu $2p_{3/2} \rightarrow 4s,3d$ dipole transitions: the intense peaks at ~933 eV and ~934 eV can be attributed to the $2p_{3/2} \rightarrow 3e_g$ transition for two different divalent Cu environments[34]. The $3e_g$ orbital results from the hybridisation of the *O2p–Cu3d* states and resulting crystal field splitting into t_{2g} and e_g[28]. The d^9 configuration of Cu^{2+} means the t_{2g} level is completely filled and the e_g is only partially filled allowing a single transition and only one peak is observed for both Cu^{2+} environments.

The peak at ~934 eV is due to the divalent copper in CuO, whereas the peak at 933 eV is due to divalent copper in $Cu_{Zn}O$. The peak at 933 eV only appears in the samples processed at 800ºC indicating that the CuO becomes incorporated into the ZnO matrix where Cu substitutes for Zn (Cu_{Zn}) in the ZnO lattice forming $Cu_{Zn}O$. Evidence of this is seen in the Cu *K*-edge EXAFS. Comparing the TEY to the FLY at 800ºC the branching ratios between the 933 eV and 934 eV peaks differ in intensity. These results

indicate that more of the CuO converts to $Cu_{Zn}O$ in the bulk than at the surface. The conversion of CuO into $Cu_{Zn}O$ is almost complete for samples of composition $Zn_{0.995}Cu_{0.005}O$ (spectra not shown) and $Zn_{0.99}Cu_{0.01}O$ treated at 800ºC.

3.6 Summary and Conclusion

X-ray Absorption Spectroscopy is a very powerful tool to provide information on oxidation state, coordination, and symmetry of a system. In this chapter, the XAFS data of the three different $Zn_{1-x}TM_xO$ (TM = Mn, Co, Cu) are reported.

It is very important to better understand the structure of these samples, to well characterise how the system evolves with changing synthesis condition (nature and concentration of the dopant and the processing temperature). This turns out to be fundamental for a deep understanding first and secondly for a precisely design of the optical, magnetic and catalytic properties described later on in the thesis.

$Zn_{1-x}Mn_xO$ nanoparticles prepared at various concentrations and temperatures were analysed: manganese is first incorporated into the ZnO wurtzite matrix as $Mn_{Zn}O$ as clearly seen in O *K*-edge and Mn *K*-edge. With increasing both dopant concentration and processing temperature, the manganese is oxidised, as revealed by both Mn *K*-edge and $L_{3,2}$-edge; the second phase also contains zinc in the form of a ZnMnO complex, most likely $ZnMnO_3$, as shown in the Zn $L_{3,2}$-edge. The Mn *K*-edge and O *K*-edge are very sensitive to secondary phase formation yet the pre-edge feature in the O *K*-edge may provide more quantitative information as to the amount of secondary phase formed. Although further tests are needed to determine the composition of the secondary phase, these results clearly show that both low dopant concentration and low temperature processing are essential if secondary phase formation is to be avoided.

It was shown that Co solubility in $Zn_{1-x}Co_xO$ nanoparticles grown by *Sol gel* methods changes with increasing cobalt concentration. At low cobalt content (x = 0.01 and 0.03) the metal exists as Co^{2+} and is located in a Zn vacancy in the wurtzite ZnO lattice in the form of $Co_{Zn}O$, shown clearly in the O *K*-edge and both Co *K*-edge and $L_{3,2}$-edge. At a higher dopant concentration (x = 0.10) the cobalt begins to aggregate inside the ZnO and forms clusters of a secondary phase, the spinel Co_3O_4. The fraction of secondary phase increases with increasing processing temperature. The amount of

Co_3O_4 formation, observed also in the Co *K*-edge and $L_{3,2}$-edge, can be quantitatively determined by examining the pre-edge feature in the O *K*-edge XANES spectra.

The XANES and EXAFS spectra have shown that the copper, in contrast to the others dopants, is initially present as CuO in $Zn_{1-x}Cu_xO$ system. Only upon increasing the processing temperature up to 800°C is it possible to convert CuO into $Cu_{Zn}O$ as can be seen in the O *K*-edge and the Cu *K*- and $L_{3,2}$-edges spectra. Furthermore, at low copper ($x \leq 0.01$) concentration the conversion to Cu_{Zn} at 800ºC is almost complete but the conversion efficiency decreases as Cu concentration increases. Comparing the TEY and FLY spectra at the Cu $L_{3,2}$-edge indicates that there is more CuO in the bulk than on the surface of the nanoparticles and more of the CuO converts to $Cu_{Zn}O$ at 800ºC in the bulk than on the surface.

PART 2. Electron Paramagnetic Resonance (EPR)

3.7 Introduction

Optical, electrical and magnetic properties of ZnO are believed to be heavily influenced by native defects, though the origin of the involved defects is still under debate.

A detailed understanding of the electronic structure of these defects and their impact on material properties requires positive identification of their origin by using appropriate experimental approaches, such as *Electron Paramagnetic Resonance* (EPR) or *Optically Detected Magnetic Resonance* (ODMR). Magnetic resonance signatures of the intrinsic defects, including oxygen vacancies (V_O) and zinc vacancies (V_{Zn}), are now well documented from the EPR studies[1-5].

Concerning the transition metal ion doped systems, $Zn_{1-x}TM_xO$, the local environment of the TM ion can be easily probed by EPR techniques.

3.7.1 Technique

Electrons and nuclei with odd mass number or even mass number but odd charge possess a non-zero spin. The spin is a fundamental characteristic of electrons and nuclei that derives from the quantum mechanical description of matter.

The spin, as a physical quantity, can be described using the spin angular momentum **I** or **S** for nuclei and electrons, respectively (these are vector quantities, and will be expressed in bold in the text)[6].

A charged particle with a non-zero spin can be associated with a spin magnetic moment $\boldsymbol{\mu}$; for an electron, it can be expressed as:

$$\vec{\mu}_e = -g_e \beta_e \vec{S}$$

where g_e is the electron *g* factor, $\beta_e = e\hbar/2m_e c$ is the electronic Bohr magneton, $-e$ is the electron charge, m_e is the electron mass and *c* is the light speed.

In the case of a nucleus, instead, it is:

$$\vec{\mu}_N = g_N \beta_N \vec{I}$$

where g_N is the nucleus *g* factor, $\beta_N = e\hbar/2m_N c$ is the nucleus Bohr magneton, *e* is the nucleus charge and m_N is the nucleus mass. Usual convention is to express the nuclear magnetic moment in this alternative way:

$$\vec{\mu}_N = \gamma_N \hbar \vec{I}$$

where γ_N is the nuclear gyromagnetic ratio expressed in $rad \cdot s^{-1} \cdot G^{-1}$.

It is possible to uniquely characterise a particle by defining its *g* factor (which is a dimensionless quantity) and its spin angular momentum. For example, the free electron has a *g* value equal to 2.002322 and $S = 1/2$.

Electrons or nuclei with a non-zero spin can also interact with an external magnetic field. If we consider a magnetic moment $\boldsymbol{\mu}$ in a magnetic field $\boldsymbol{B_0}$ the interaction's energy can be written as follow:

$$E = -\vec{\mu}_i \cdot \vec{B}_0$$

where $i = e$ or N, if the magnetic moment is referred to an electron or a nucleus, respectively.

The energy difference between spin states, characterised by a different spin momentum's orientation with respect to the external field, will be:

$$\Delta E = -g_e \beta_e B_0 (m_{S,1} - m_{S,2})$$

where the quantum number m_S labels different orientations of the angular spin momentum S (for a nucleus it is sufficient to substitute g_e, β_e and m_S with g_N, β_N and m_N and to change the sign in the right-hand side of the equation).

Increasing the external magnetic field's intensity, the energy difference between spin states increases (figure 18 shows the situation of an electron). In the absence of an external magnetic field – also excluding the presence of eventual fields due to the presence of magnetic moments nearby the particle under examination – spin states of a particle with a magnetic moment have the same energy.

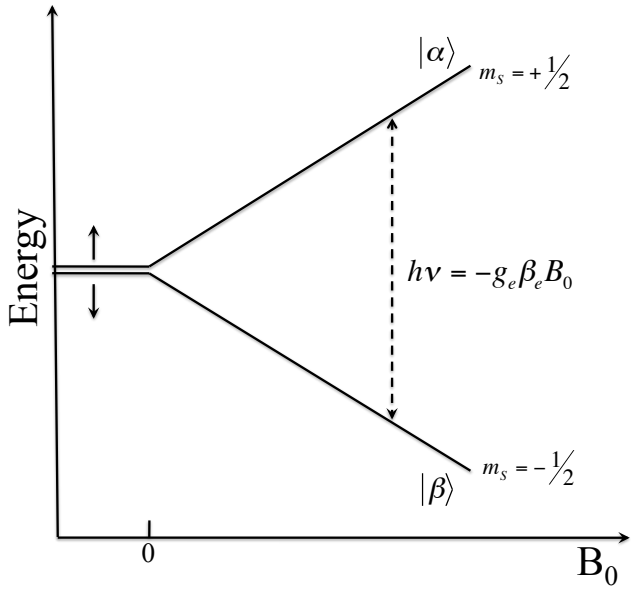

Figure 18: Scheme of spin state's energy of an electron in the presence of an external magnetic field $\boldsymbol{B_0}$.

In a macroscopic set of spins in thermal equilibrium, the population of each spin state is independent of its energy level. Taking into account a particle with a spin momentum of ½, like in the case of an electron, there are two different spin states that at thermal equilibrium will have a population ratio, according to a Boltzman's distribution, of

$$\frac{N_2}{N_1} = \exp\left(\Delta E / K_B T\right)$$

where $\Delta E = E_2 - E_1$ with $E_2 > E_1$, K_B is the Boltzman's constant, T is the absolute temperature of the system and N_J is the population of the J^{th} state (J =1, 2). If the temperature is sufficiently high, so that $\Delta E/K_B T \rightarrow 0$, it is possible to approximate

$$\frac{N_2}{N_1} = \exp\left(\Delta E / K_B T\right) \approx 1 + g_i \beta_i B_0 / K_B T$$

In the presence of a magnetic field $\boldsymbol{B_1}$ perpendicular to $\boldsymbol{B_0}$, which oscillates to a frequency ν, it is possible to induce a transition 1→2 from spin state 1 to spin state 2, or vice versa. The condition to satisfy for the resonance is

$$h\nu = \Delta E_{1,2} = g_i \beta_i B_0$$

If, before the interaction with $\boldsymbol{B_1}$, $N_1 > N_2$ there will be an energy transfer from the oscillating field to the spin system; vice versa if $N_2 > N_1$. The first case is commonly called absorption, the latter stimulated emission.

It is possible to satisfy the condition for resonance with two different configurations: keeping the static field, $\boldsymbol{B_0}$, constant and perform a scan of the intensity of the oscillating field, $\boldsymbol{B_1}$, or keeping the frequency, ν, constant and varying the intensity of the static field. The latter is the most simple experiment of *Electron Spin Resonance* (ESR or EPR).

So far we have considered the spins as independent entities but different types of magnetic interactions can exist in a system formed by a collection of spins.

Speaking of electrons, the first interaction to consider is due to the presence of a nucleus that shields the static field $\boldsymbol{B_0}$. For that reason, an electron of an atom or a molecule will be resonant at a lower frequency with respect to a free electron in the same static field. In EPR, it is common to relate this variation in the transition frequency to a different value of the *g* factor assigned to electrons in different environments.

The presence of anisotropy is introduced by taking into consideration *g* as a tensor quantity:

$$g = \begin{pmatrix} g_x & 0 & 0 \\ 0 & g_y & 0 \\ 0 & 0 & g_z \end{pmatrix}$$

where g_i ($i = x, y, z$) are the principle value of the tensor. This consideration comes from the presence of an interaction between the static field $\boldsymbol{B_0}$ and the magnetic moment which derives from the total angular momentum – i.e. the spin-orbit coupling.

Finally, there is an interaction, defined as hyperfine interaction, between electronic or nuclear spins: the mechanisms associated with this interaction are defined as Fermi's contact or dipolar coupling.

Fermi's contact interaction derives from the finite probability to find an electron on the nucleus: in the presence of a non-zero nuclear spin, the anti-parallel – rather than the parallel – alignment of the electron spin is the favoured configuration. The spin energy states are then affected from the coupling with nuclear spins.

Dipolar interaction, on the other side, is a function of the orientation and the distance between the electron and the nucleus that are interacting: each nuclear magnetic dipole generates a magnetic field that affects the surrounding electrons.

Hyperfine interaction can be expressed in terms of a tensor ***A*** (called the hyperfine tensor) that takes into account the Fermi's contact and the dipolar contribution. It is worth noting that the anisotropy of tensor ***A*** comes exclusively from the dipolar interaction.

3.7.2 Experimental

Continuous wave EPR spectra were recorded using an Elexsys E500 Bruker spectrometer operating at X-band equipped with a SHQ cavity and a continuous flow 4He cryostat (CF935, Oxford Instruments) for variable temperature measurements.

3.8 Undoped ZnO

In this section *Electron Paramagnetic Resonance* data on undoped zinc oxide will be presented. Results will be discussed in terms of the synthetic condition to understand the evolution of the system upon increasing the annealing temperature. In particular to understand the presence of native defects which will influence the catalytic, optical and magnetic properties reported in the next chapters.

3.8.1 Literature

Most of the experimental investigations of oxygen vacancies and other types of defects in ZnO to date have relied on EPR measurements[7-19].

Many of these studies fall into two categories, depending on the value of the *g*-factor: one set reports oxygen vacancies with a *g* value of ~1.96[8,9,13-17,19], the other with g ~ 1.99[10,11,13,18,19].

There is, however, overwhelming evidence that oxygen vacancies are actually associated with the g ~ 1.99 line. For example, the g ~ 1.99 signal, which is related to a native defect, shows[18] hyperfine interactions with the ^{67}Zn neighbours of the vacancy; whereas no hyperfine interactions have been reported for the g ~ 1.96 line.

The latter is likely to be associated with electrons in the conduction band or in a donor band[12,16,19]. The g ~ 1.96 signal has also been reported to be enhanced under UV

illumination[14,16,17,19]. UV light can indeed promote electrons into the conduction-band states in ZnO, consistent with the g ~ 1.96 line corresponding to electrons in delocalised states (shallow donors).

3.8.2 Experimental Spectra

EPR spectra of ZnO nanoparticles annealed at different temperatures have been measured at a range of temperatures between 5 K and room temperature. Figure 19 shows the evolution of the system as a function of both synthetic condition (i.e. annealing temperature) and working temperature.

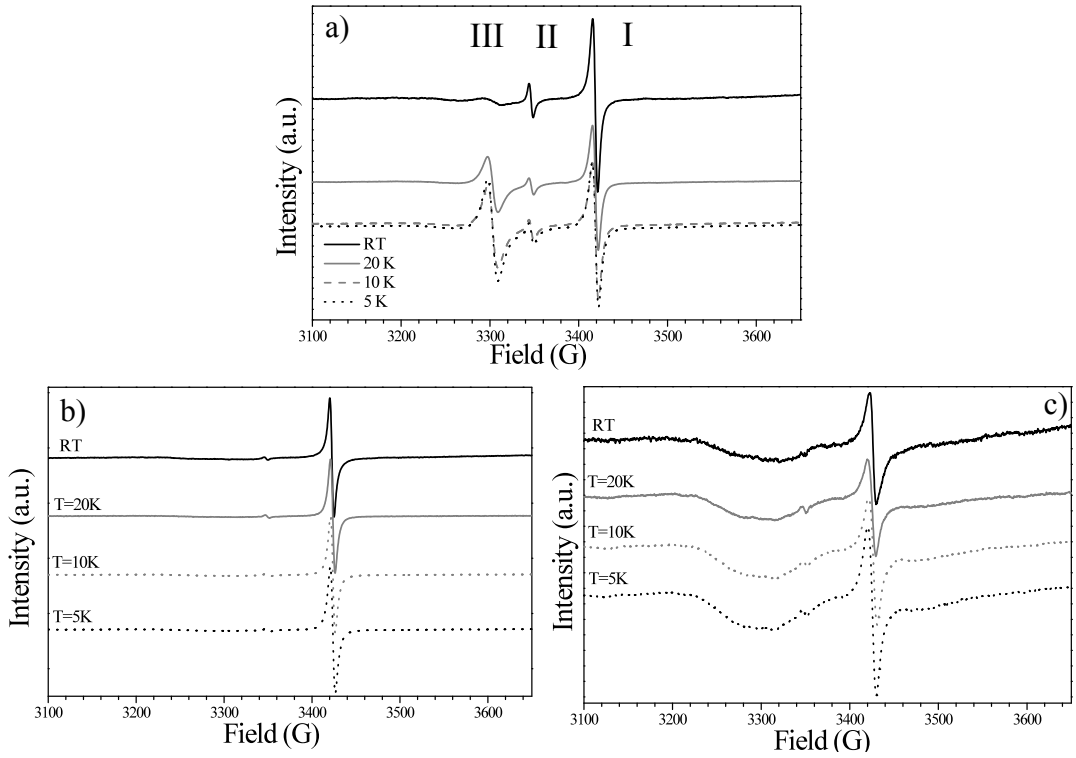

Figure 19: EPR spectra of ZnO nanoparticles measured at different temperatures for samples: **a)** ZnO_400, **b)** ZnO_600 and **c)** ZnO_800.

The spectra are quite rich in features, and three main signals can be identified. Sample ZnO_400 (figure 19a) presents signals at g = 1.96 (signal I), g = 2.006 (signal II) and an additional isotropic signal at g 2.03 (signal III). Increasing the annealing temperature to those of sample ZnO_600 (figure 19b) and ZnO_800 (figure 19c), the EPR spectra show only the presence of signals I and II. Furthermore, a broad hill characterised signal with $g > 2.1$ is observed for samples treated at 800°C.

Signal I occurring at g ca. 1.96 is easily attributed to shallow donor, as well reported in literature[7,12,16,19]. Furthermore, its position is strongly dependent on the nanoparticles'

dimensions (i.e annealing temperature) rather than on the measurement temperature. Figure 20a shows, as an example, the position dependence of signal I as a function of the working temperature for sample ZnO_400. Panels reported in figure 20b and 20c, instead report its position dependence as a function of the nanoparticles main size.

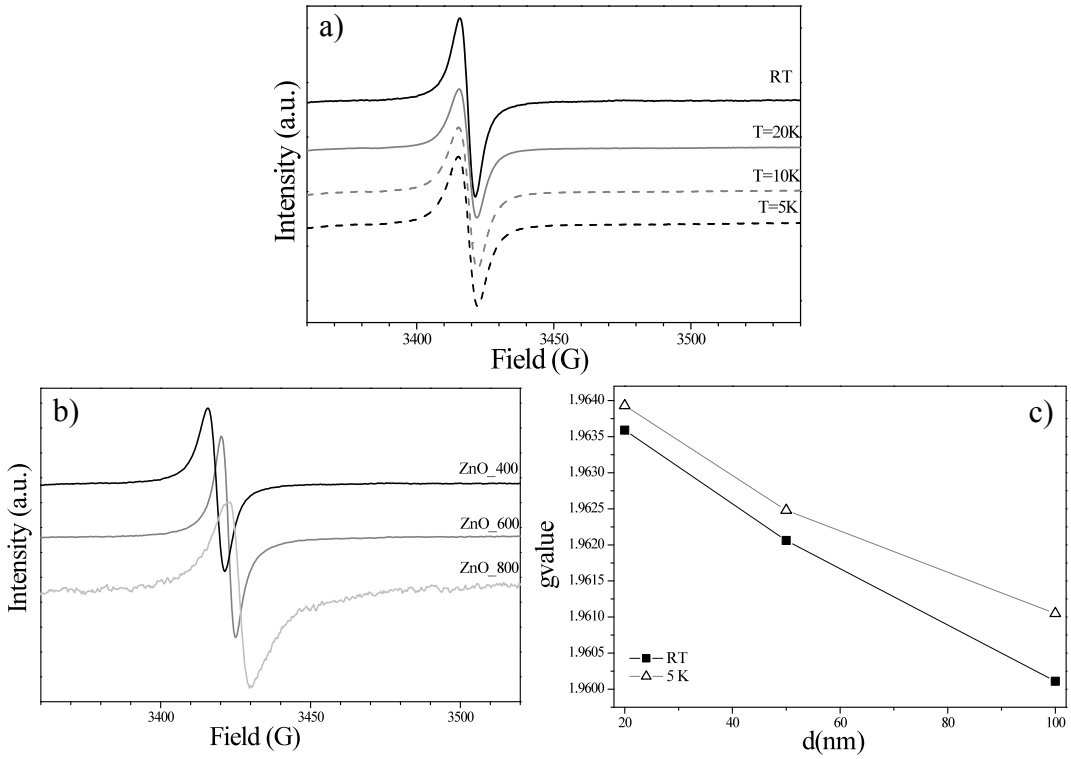

Figure 20: Panels that show the g shift of the line centred at g = 1.96 **a)** ZnO_400 as a function of temperature **b)** spectra at RT for different annealing temperatures **c)** dependence of line centred at g =1.96 as function of nanoparticles main size for spectra taken at RT and T = 5K.

On the other hand, signal II that occurs at a *g* value of ca. 2.00, on the basis of several different literature reports[7-19] is related to the presence of surface oxygen vacancies. Its relative intensity compared to signal I is significantly dependent on the measurement temperature, while it is clearly reduced on increasing annealing temperature (figure 19).

Finally, a third signal (signal III) is observed, for low temperature annealed ZnO nanoparticles, which gains much intensity at low measurement temperature. To the best of our knowledge, this signal has not been previously reported for ZnO systems in literature. Its peculiar temperature dependent behaviour, as well as its absence for systems annealed at T < 400°C seems to indicate that it might be due to interstitial substitution.

3.9 $Zn_{1-x}Cu_xO$

In this section EPR data on copper doped zinc oxide, $Zn_{1-x}Cu_xO$, will be presented. Results will be discussed in terms of synthetic condition to understand the evolution of the system with increasing dopant concentration and annealing temperature. It is important to understand the local environment of the transition metal ion to better characterise the system and detect the eventual formation of secondary phases instead of uniform dispersion of the copper inside the ZnO matrix.

3.9.1 Literature

Copper ions with oxidation state of +2 (Cu^{2+}) have only one unpaired electron and so their EPR spectra are very simple. The presence of ^{63}Cu and ^{65}Cu nuclei, having nuclear spins $I = 3/2$, generates a characteristic pattern consisting of four lines each due to the coupling between the electron and nuclear spins (hyperfine interaction). The spin Hamiltonian parameters are highly sensitive to the local geometry, so that the EPR technique allows differentiation of Cu in different environments and the investigation of short-range order.

EPR studies of a divalent copper ion Cu^{2+} in a zinc lattice site of ZnO has been reported ($g_{||} = 0.7383 \pm 0.0003$, $g_{\perp} = 1.5237 \pm 0.003$)[20]. In this configuration the copper ions have been found to occupy distorted tetrahedral sites as substitution of the zinc in the wurtzite crystal structure.

A similar system, Cu doped ZrO_2 nanoparticles prepared by *Sol gel* synthesis has been studied[21]. As far as the local environment and the location of Cu in the oxide matrix are concerned, four types of paramagnetic Cu species, viz. isolated, substitutional ions (species I), extra-lattice/interstitial ions (species II), dispersed surface bound ions (species III) and CuO clusters (species IV), have been identified by EPR spectroscopy and spectral simulations, depending on the concentration of copper in zirconia.

3.9.2 Experimental Spectra

EPR spectra of $Zn_{1-x}Cu_xO$ nanoparticles annealed at different temperatures and with different copper concentrations have been measured at 10K. Figure 21 shows the evolution of the system as a function of the synthetic conditions, i.e. annealing temperature and dopant content.

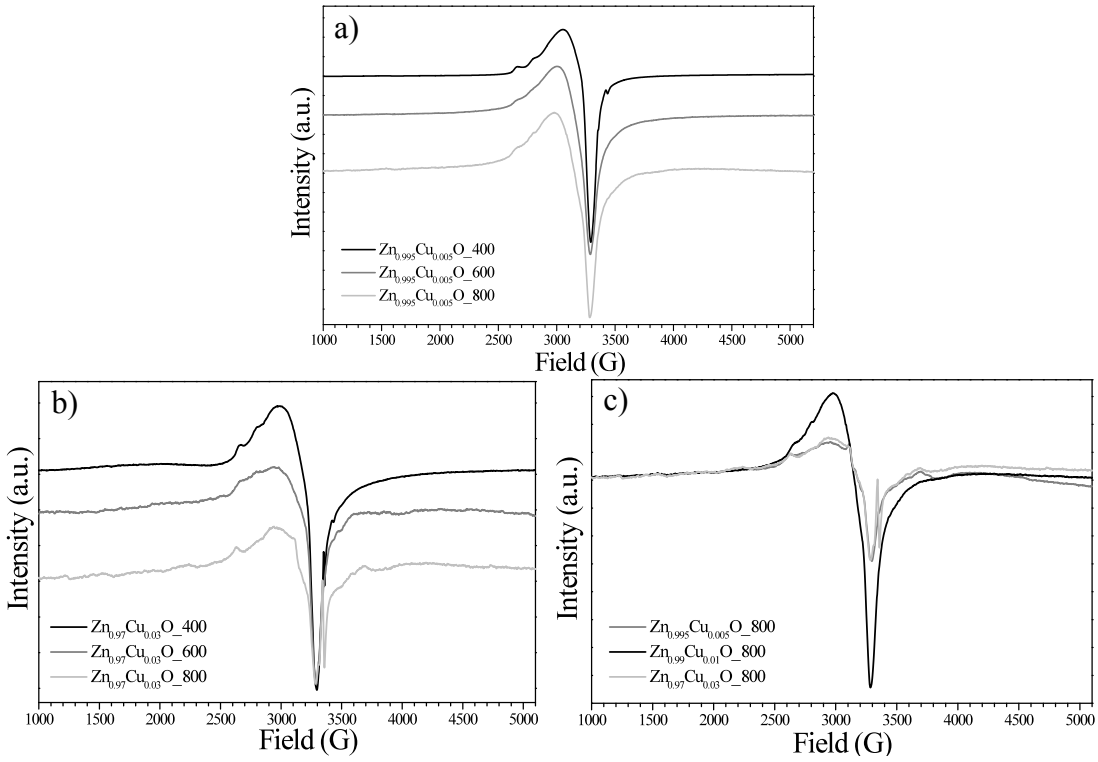

Figure 21: 10K EPR spectra of **a)** $Zn_{0.995}Cu_{0.005}O$ at different annealing temperature **b)** $Zn_{0.97}Cu_{0.03}O$ at different annealing temperature **c)** $Zn_{1-x}Cu_xO\_800$ samples at different doping levels.

EPR spectra recorded at 10K of low concentration copper doped ZnO, $Zn_{0.995}Cu_{0.005}O$, are reported in figure 21a for different annealing temperatures. No signal attributable to tetrahedral distorted Cu(II), earlier reported[20] as substitutional Zn impurity of ZnO, could be detected, even by investigating a broader range field.

It is clear that the spectra are the result of the convolution of at least two different signals, an axial one with $g_{//} = 2.34$ and $g_{perp} = 2.065$ and a broad, unstructured one, centred around $g = 2.15$, whose relative intensity increases with the annealing temperature, leading to an apparent broadening of the convoluted signal. The sharp signal observed in the $Zn_{0.995}Cu_{0.005}O\_400$ spectrum at $g = 1.96$ is attributed to shallow donors from the ZnO lattice[7,12,16,19].

The observation of the pattern $g_{//} > g_{perp} > g = 2.000$ as well as a hyperfine parallel component $A_{//} = 1.47 \times 10^{-2}$ cm^{-1} suggest that the axial signal should be attributed to

copper(II) species, as also clearly indicated by the hyperfine splitting in four lines, due to ^{63}Cu and ^{65}Cu, both with *I= 3/2* and very similar gyromagnetic ratios. Furthermore, it is possible to assign it to a tetragonally distorted octahedral site, thus favouring an assignment of this signal to isolated Cu(II) on the surface[21,22].

The broad signal centred at g = 2.1 can be attributed to small clusters of closely lying copper centres, which result in an increase in both dipolar and exchange interactions among them[21,22]. The formation of exchange coupled species is clearly shown by the increase in the relative intensity of the half field transition (formally Δm_s = ±2) observed around g = 4.3, compared to the main signal.

In figure 21c the concentration dependence of the EPR signal of T = 800°C annealed samples is reported. The spectra clearly show a strong decrease of the intensity of the signal attributable to Cu(II) on increasing concentration: this phenomenon can be seen if compared with the signal at g = 2.006 due to oxygen vacancies on the surface of the ZnO lattice (see above). This clearly indicates the formation of EPR-silent copper containing clusters whose fraction is increasing with increasing temperature, suggesting that segregation is occurring at high annealing temperatures and high concentration.

3.10 Summary and Conclusion

In these sections *Electron Paramagnetic Resonance* data on undoped ZnO and copper doped zinc oxide, $Zn_{1-x}Cu_xO$, have been presented. Results have been discussed in terms of synthetic condition to understand the evolution of the system with increasing annealing temperature and dopant concentration.

Particular interest has been devoted to understand the presence of native defects that will influence the catalytic, optical and magnetic properties reported in the following chapters. It is also important to understand the local environment of the transition metal ion to better characterise the system and detect the eventual formation of secondary phases instead of a uniform dispersion of the copper inside the ZnO matrix.

The EPR spectra of the nominally pure ZnO show the well known signals at g = 1.96 (signal I) and g = 2.006 (signal II). It seems by now accepted wisdom that signal I, which is a shallow donor, is associated with electrons in the conduction band while signal II corresponds to oxygen vacancies with one trapped electron[7,19]. The reported

temperature dependence of signal II intensity parallels the rate of formation of the ZnO phase; similar behaviour is also observed for ZnO nanoparticles synthesised by *Sol gel*. On the other hand the position of signal I is strongly dependent on the nanoparticles' dimensions.

Contrasting previously reported data, undoped ZnO treated at 400°C reports the presence of an additional isotropic signal at $g = 2.03$, signal III. It is strongly favoured by low treatment temperatures, as EPR spectra of samples annealed in more severe conditions do not show this signal. Furthermore, it also depends on the measurement conditions: at room temperature the signal is broad but it narrows on decreasing temperature. The large orbital contribution suggests a role of spin orbit coupling systems like oxygen and zinc. To the best of our knowledge, this signal has not been previously reported for ZnO systems in literature and further characterisation will be needed to well ascribe its origin.

EPR spectra of $Zn_{1-x}Cu_xO$ nanoparticles annealed at different temperatures and with different copper concentrations have been measured resulting in the detection of two different types of paramagnetic copper.

The observation of the pattern $g_{//} > g_{perp} > g = 2.000$ ($g_{//} = 2.34$ and $g_{perp} = 2.065$) as well as a hyperfine parallel component $A_{//} = 1.47 \times 10^{-2}$ cm^{-1} suggest that the axial signal should be attributed to a tetragonally distorted octahedral site, thus favouring an assignment of this signal to isolated Cu(II) on the surface[21,22]. The broad signal centred at $g = 2.1$ should be attributed to small clusters of closely lying copper centres, which result in an increase in both dipolar and exchange interactions among them[21,22].

Finally, the formation of EPR-silent copper containing clusters whose fraction is increasing with increasing temperature has been detected. This suggests that segregation is occurring at high annealing temperatures and high concentrations.

It will be important to also characterise the other transition metal ion doped systems, $Zn_{1-x}TM_xO$ (TM = Mn and Co) to understand the local environment of the TM ions and detect the eventual formation of secondary phases instead of the uniform dispersion of dopant inside the ZnO matrix.

References:

PART 1

[1] H. Winick, S. Doniach, *Synchrotron Radiation Research*, Plenum Press, New York (1980)

[2] T.K. Sham, *Synchrotron Radiation: Earth, Environmental and Materials Sciences Applications*, edited by G.S. Henderson, D.R. Baker, Minerological Association of Canada, Saskatoon (2002)

[3] J. Stohr, *NEXAFS Spectroscopy*, vol. 25 Springer-Verlag, New York (1992)

[4] D.C. Koningsberg, R. Prins, *X-ray Absorption: Principles, applications techniques of EXAFS, SEXAFS, and XANES,* vol. 92 John Wiley and Sons, Toronto (1988)

[5] B.K. Teo, *EXAFS: Basic principles and data analysis*, Springer, New York (1986)

[6] A. Rogalev, J. Goulon, *Chemical Applications of Synchrotron Radiation, Part II: X-ray Applications, vol. 12B*, edited by T.K. Sham, World Scientific, River Edge, NJ (2002)

[7] R.A. Rosenberg, G.K. Shenoy, L.C. Tien, D. Norton, S. Pearton, X.H. Sun, T. K. Sham, *Appl. Phys. Lett*. **89** (2006) 093118

[8] J.W. Chiou, K.P. Krishna Kumar, J.C. Jan, H.M. Tsai, C.W. Bao, W.F. Pong, F.Z. Chien, M.H. Tsai, I.H. Hong, R. Klauser, J.F. Lee, J.J. Wu, S.C. Liu, *Appl. Phys. Lett*. **85** (2004) 3220

[9] B.L. Henke, E.M. Gullikson, J.C. Davis. *X-ray interactions: photoabsorption, scattering, transmission, and reflection at E=50-30000 eV, Z=1-92*, Atomic Data and Nuclear Data Tables Vol. 54 (no.2), pp. 181-342 (July 1993)

[10] W. Yan, Z. Sun, Q. Liu, Z. Li, Z. Pan, J. Wang, S. Wei, D. Wang, Y. Zhou, and X. Zhang, *Appl. Phys. Lett.* **91** (2007) 062113

[11] N. Smolentsev, A.V. Soldatov, G. Smolentsev, S.Q. Wei, *Solid State Commun.* **149** (2009) 1803

[12] X. Zhang, Y. Zhang, Z.L. Wang, W. Mai, Y. Gu, W. Chu, Z. Wu, *Appl. Phys. Lett.* **92** (2008) 162102

[13] J. Pellicer-Porrer, A. Segura, J.F. Sanchez-Royo, J.A. Sans, J.P. Itie, A.M. Flank, P. Lagarde, A. Polian, *Superlattices and Microstructures* **42** (2007) 251

[14] I. Tanaka, F. Oba, *J. Phys.: Condens. Matter* **20** (2008) 064215

[15] P. Sharma A. Gupta, K.V. Rao, F.J. Owens, R. Sharma, R. Ahuja, J.M.O. Guillen, B. Johansson, G.A. Gehring, *Nat. Mater.* **2** (2003) 673

[16] R.K. Singhal, M. Dhawan, S. Kumar, S.N. Dolia, Y.T. Xing, E. Saitovitch, *Physica B* **404** (2009) 3275

[17] Y. Wang, J. Zou, Y.J. Li, B. Zhang, W. Lu, *Acta Materialia* **57** (2009) 2291

[18] A.R. Han, S.J. Hwang, Y. Zhao, Y. U. Kwon, *J. Magn. Magn. Mater.* **320** (2008) 1591

[19] T.C. Kaspar, T. Droubay, Y. Li, S.M. Heald, P. Nachimuthu, C.M. Wang, V. Shutthanandan, C.A. Johnson, D.R. Gamelin, S.A. Chambers, *New J. Phys.* **10** (2008) 055010

[20] J.D. Bryan, S.M. Heald, S.A. Chambers, D.R. Gamelin, *J. Am. Chem. Soc.* **126** (2004) 11640

[21] S.A. Chambers, S.M. Heald, T. Droubay, *Phys. Rev. B* **67** (2003) 100401

[22] K.A. Griffin, A.B. Pakhomov, C.M. Wang, S.M. Heald, K.M. Krishman, *Phys. Rev. Lett.* **94** (2005) 157204

[23] D.H. Kim, J.S. Yang, Y.S. Kim, T.W. Noh, S.D. Bu, S.I. Baik, Y.W. Kim, Y.D. Park, S.J. Pearton, J.Y. Kim, J.H. Park, H.J. Lin, C.T. Chen, Y. J. Song, *Phys. Rev. B* **71** (2005) 014440

[24] G. Martinez-Criado, A. Segura, J.A. Sans, A. Homs, J. Pellicer-Porres, J. Susini, *Appl. Phys. Lett.* **89** (2006) 061906

[25] M. Murakami, Y. Matsumoto, T. Hasegawa, P. Ahmet, K. Nakajima, T. Chikyow, H. Ofuchi, I. Nakai, H. Koinuma, *J. Appl. Phys.* **95** (2004) 5330

[26] J. G. Chen, *Surf. Sci. Rep.* **30** (1997) 1

[27] T. Yao, W. Yan, Z. Sun, Z. Pan, Y. Xie, Y. Jiang, J. Ye, F. Hu, S. Wei, *J. Phys. Chem C* **113** (2009) 14114

[28] A.B. Gurevich, B.E. Bent, A.V. Teplyakov, J.G. Chen, *Surf. Sci.* **442** (1999) L971

[29] F.M.F. de Groot, M. Grioni, J.C. Fuggle, J. Ghijsen, G.A. Sawatzky, H. Petersen, *Phys. Rev. B* **40** (1989) 5715

[30] S. Bocharov, Th. Kirchner, G. Drager, O. Sipr, A. Simunek, *Phys. Rev. B* **63** (2001) 045104

[31] J. Chaboy, A. Munoz-Paez, E. S. Marcos, *J. Sync. Rad.* **13** (2006) 471

[32] D. Grandjean, H.L. Castricum, J.C. van den Heuvel, B.M. Weckhuysen, *J. Phys. Chem. B* **110** (2006) 16892

[33] M.M. Gunter, B. Bems, R. Schlogl, T. Ressler, *J. Sync. Rad*. **8** (2001) 619

[34] D.J. Keavney, D.B. Buchholz, Q. Ma, R.P.H. Chang, *Appl. Phys. Lett.* **91** (2007) 012501

PART 2

[1] J.M. Smith, W.E. Vehse, *Phys. Lett. A* **31** (1970) 147

[2] D.R. Locker, J.M. Meese, *IEEE Trans. Nucl. Sci.***19** (1972) 237

[3] A.L. Taylor, G. Filipovich, G.K. Lindeberg, *Solid State Commun.* **8** (1970) 1359

[4] K. Tarkepa, A. Ots, V.A. Nikitenko, *J. Phys. Chem. Solids* **55** (1994) 1353

[5] L.S. Vlasenko, G.D. Watkins, *Phys. Rev. B* **72** (2005) 035203

[6] P. Atkins, J. De Paula, *Atkins' Physical Chemistry*, 8th Ed. Oxford University Press (2006)

[7] F.H. Leiter, H.R. Alves, A. Hofstaetter, D.M. Hoffmann, B.K. Meyer, *Phys. Stat. Sol. B* **226** (2001) R4

[8] A. Hausmann, *Z. Phys.* **237** (1970) 86

[9] K. Hoffmann, D. Hahn, *Phys. Status Solidi* A (1974) 24637

[10] L.S. Vlasenko, G.D. Watkins, *Phys. Rev. B* **71** (2005) 125210

[11] S.M. Evans, N.C. Giles, L.E. Halliburton, L.A. Kappers, *J. Appl. Phys.* **103** (2008) 043710

[12] N.Y. Garces, N.C. Giles, L.E. Halliburton, G. Cantwell, D.B. Eason, D.C. Reynolds, D.C. Look, *Appl. Phys. Lett.* **80** (2002) 1334

[13] K. Tarkpea, A. Ots, V. Nikitenko, *J. Phys. Chem. Solids* **55** (1994) 1353

[14] A. Poppl, G. Volkel, P*hys. Status Solidi* A **121** (1990) 195

[15] P.H. Kasai, *Phys. Rev.* **130** (1963) 989

[16] K.A. Muller, J. Schneider, *Phys. Lett.* **4** (1963) 288

[17] C.H. Geisler, G.L. Simmons, *Phys.Lett.* (1964) 11111

[18] J.M. Smith, W.E. Vehse, *Phys. Lett. A* **31** (1970) 147

[19] D.M. Hofmann, A. Hofstaetter, F. Leiter, H. Zhou, F. Henecker, B.K. Meyer, S.B. Orlinskii, J. Schmidt, P.G. Baranov, *Phys. Rev. Lett.* **88** (2002) 045504

[20] R.E. Dietz, H. Kamimura, M.D. Sturge, A. Yariv, *Phys. Rev.* **132** (1963) 1559

[21] V. Ramaswamy, M. Bhagwat, D. Srinivas, A.V. Ramaswamy, *Catalysis Today* **97** (2004) 63

[22] F. Ciorcas, S.K. Mendiratta, I. Ardelean, M.A. Valente, *Eur. Phys. J. B* **20** (2001) 235

Chapter 4

Catalytic activity: Methanol Steam Reforming Structure-Property Relationship

In this chapter functional characterisation of ZnO based material for catalytic applications, both undoped and copper-doped ($Zn_{1-x}Cu_xO$), will be presented. In particular, the ability of these materials to convert, in a sustainable manner, methanol to hydrogen via a *Steam Reforming* reaction ($CH_3OH + H_2O \rightarrow CO_2 + 3H_2$) has been investigated.

The primary goal of this research is surely to understand the process not only in terms of activity and selectivity, but especially to unravel and clarify the reaction mechanism and the actual role of the catalyst. Our aim is to contribute to the knowledge required for the *a priori design* of new materials with predictable and improved catalytic performance.

4.1 Introduction

Nowadays hydrogen production via catalytic *Steam Reforming* of alcohols is one of the most promising and suitable technologies. Even though methane is currently the main fuel in industrial hydrogen production, other hydrogen carriers can also be used for this reaction. As a matter of fact both methanol (CH_3OH) and ethanol (CH_3CH_2OH) are excellent candidates as H_2 vectors due to their high hydrogen-to-carbon ratio and their ready supply. Additionally they can be obtained from renewable biomass: methanol trough gasification and synthesis and ethanol trough fermentations[1-14].

Methanol[1-10], in particular, contains no carbon–carbon bonds, thus reducing the risk for coke formation and catalyst fouling. The absence of a strong C–C bond also facilitates the reformation at low temperatures (200–300°C). This range of temperatures is very low when compared to other common fuels such as methane, which is reformed above 500°C[15], and ethanol, with a reforming temperature around 400°C[16]. Although methanol is highly toxic and miscible in water, it has the advantage of being biodegradable, liquid at atmospheric conditions and it has a high hydrogen to carbon ratio[17]. There is a high capacity for production of methanol worldwide, mainly from natural gas, but methanol can also be produced from renewable sources, such as biomass, causing no net addition of carbon dioxide to the atmosphere.

One of the main drawbacks of *Methanol Steam Reforming* is the formation of CO as a by-product to the major products hydrogen and carbon dioxide. Carbon monoxide is spread mainly due to secondary reactions that compete with the primary process of reformation (R1), such as the direct decomposition (R2) or the partial oxidation (R3)[6-10]. Without oxygen it is possible to reach a high level of selectivity towards the reforming reaction only if decomposition does not occur or, if it does, through the conversion of CO produced by the water gas shift reaction (R4).

$$CH_3OH + H_2O \rightarrow CO_2 + 3H_2 \quad \text{(R1)}$$

$$CH_3OH \rightarrow CO + 2H_2 \quad \text{(R2)}$$

$$CH_3OH + ½\ O_2 \rightarrow CO_2 + 2H_2 \quad \text{(R3)}$$

$$CO + H_2O \rightarrow CO_2 + H_2 \quad \text{(R4)}$$

Even though the purpose of the *Methanol Steam Reforming* reaction is the production of hydrogen, there are other products formed that must be taken into consideration. Besides the non-reacted water and methanol, the reaction mixture comprises hydrogen, carbon dioxide and small amounts of carbon monoxide. As the hydrogen produced is for PEM (*Polymer Electrolyte Membrane*) fuel cell applications, it is clear that the formation of carbon monoxide must be minimised as it is known that CO poisons the anodic catalyst of these low temperature fuel cells[22]. This highlights the importance of the catalytic performance in the reaction. Ideally, the catalyst should not only be highly active in order to produce large amounts of hydrogen but also highly selective so that the carbon monoxide produced is negligible; finally it should present long-term stability.

Several catalysts based on semiconducting oxides capable of converting methanol satisfactorily have been proposed in literature: i.e. ZnO[4-10], ZrO_2[18], ZnO/ZrO_2[19] unaltered or doped with different metal such as Cu[4-10], Pd[20], Ni and Co[21] both in their metallic or oxidised states.

One of the biggest controversies of these types of system is the proper attribution of the role of the individual components of the catalyst and the mechanism that underlies the functioning of these materials. In fact, it is not clear from the literature[5-20] if the role of the semiconductor is purely passive or whether it may be able to participate actively in the catalytic process. Regarding the dopant, there is conflicting evidence of the state of oxidation that is actually active in the process[6-20].

4.1.1 Activity of ZnO Doped Cu Catalyst

Copper-based catalysts are the most commonly used for the *Methanol Steam Reforming* reaction (MSR) due to their high activity and selectivity[4-10,23-26]. However, these catalysts are known for their pyrophoric characteristics and deactivation by thermal sintering[23-24].

In order to improve their stability and catalytic activity, several approaches are reported in the literature, for example trying to focus on the effects of the preparation method[4-10,23,25-26]. In fact, similar catalysts prepared by different methods can present distinct catalytic properties. This turns out to be one of the main reasons for the lack of agreement about the active role of different components in the catalytic process.

There is general agreement about the central role played by the reduced copper, while ZnO is considered to primarily act as catalytic promoter influencing the reducibility of CuO and helping to prevent the deactivation, increasing the stability of the system[27,28].

A detailed knowledge of the relationships between catalytic activity and surface and bulk structure is desirable to prepare new and improved catalysts according to a knowledge-based (rational) catalyst design. Unfortunately for the majority of heterogeneous catalysts the required structure–activity relationship is not sufficiently understood. Micro-structural characteristics and chemical composition of the catalysts can be tailored directly during the preparation, and this can strongly affect the activity.

4.1.2 Activity of Undoped ZnO

Zinc oxide is used as a catalyst or a catalyst support in heterogeneous catalysis, and is a major component of all industrial catalysts for methanol synthesis. The first catalysts for methanol synthesis, first used in 1923 by BASF, consisted of ZnO/Cr_2O_3, in which ZnO was the primary active component[29-30]. In the ternary $Cu/ZnO/Al_2O_3$ catalysts, used since the 1960s, Cu is the main active component[30,31], but it is assumed that the strong interaction between Cu and ZnO creates highly active sites[30].

As mentioned previously, there is little agreement in the scientific community[5-20] over the ascription of function for each individual component of the catalyst. In fact, it is not yet clear if the role of the semiconductor is purely passive or whether it may be able to participate actively in the catalytic process.

More recent literature[32-33] has proven that the role of ZnO is not solely to support the catalyst and prevent the sintering of copper nanoparticles, but it also has an active role in the catalytic process. Defects in the semiconductor, and more precisely oxygen vacancies, act as active sites.

4.1.3 Experimental

The catalytic tests were carried out by loading roughly 40 mg of the sample in a "U" shaped glass reactor, the temperature was checked by means of a thermocouple inserted into the reactor. In each test, the reactor was fed with vapours of aqueous solutions (1M) of methanol, carried by a pure argon flow; a mass flow controller (MKS instruments) was used to adjust the flux of the incoming gas. The effluent gases from the reactor reached the FTIR (*Fourier Transform Infrared Spectroscope*) and the QMS (*Quadrupole Mass Spectrometer*) for analysis. The feed reservoir was kept at 19°C throughout. Taking into account this physical parameter, a series of thermodynamic calculations were made to obtain the quantity of evaporated alcohol per minute. The thermodynamic calculations were performed using AspenPlus software utilising a "gamma-fi"-type model and employing the Redlich–Kwong equation for the determination of the fugacity coefficients, and the NRTL (*Non-Random Two Liquid*) for the activity coefficients. The obtained values were also experimentally verified by means of repeated control tests. Based on this, the *Weight Hourly Space Velocity* (WHSV, weight of alcohol per gram of catalyst per hour) for the investigated condition

is 1 h^{-1}. The tests were performed for 25 min at several temperatures between RT and 400°C; during this time, the system always reaches a steady state. The experimental setup was also tested in the absence of catalyst with respect to steam reforming conditions in order to verify that no spurious conversion of alcohols occurs. The experimental results confirm the absence of alcohol conversion due to the test conditions.

The IR spectra were collected in a Bruker Tensor 27 spectrophotometer (32 scans at a resolution of 1 cm^{-1}) employing a flow chamber for gas analysis, fitted with NaCl windows (the spectrum of the chamber in argon flow was used as background).

Mass data was obtained by means of a System Genesys I 200D by European Spectrometry Systems. The obtained mass spectra were corrected for the multi-contributions taking into account the fragmentation patterns for each investigated compound. The mass spectra library was produced by individually analysing the reactants and the obtained products.

4.2 Catalytic Activity

The activity of different samples, appropriately selected, for the MSR reaction was tested to determine which synthetic parameters are able to influence the catalytic performances.

As demonstrated in previous chapters, one of the variables that certainly plays a key role on the composition, structure and morphology of ZnO powders is the annealing temperature, it was therefore decided to investigate two different sets of samples processed at 400°C and 800°C, respectively. A second parameter is the concentration of dopant: as noted earlier, depending on the dopant's content it is possible to obtain a solid solution (Zn,Cu)O or partial segregation of CuO. Testing the performance of copper doped ($Zn_{1-x}Cu_xO$) samples, with x= 0.01 and 0.10, should allow a better understanding of the role of dopant that is somewhat controversial in the literature[4-10]. Similarly, the study of undoped samples should elucidate the actual role of the neat semiconductor in the catalytic process.

A final parameter, which could influence the activity of these systems, is the surface area (*Specific Surface Area*, SSA) of the nanopowders: an increase in contact area

between catalyst and analyte leads to an increase in activity. Table 1 shows the SSA values obtained by measuring the BET with nitrogen.

Table 1: BET of $Zn_{1-x}Cu_xO$ powders.

Samples	BET Specific surface area (m^2/g)
ZnO_400	27.0
$Zn_{0.99}Cu_{0.01}$_400	21.3
$Zn_{0.90}Cu_{0.10}$_400	27.2
ZnO_800	10.4
$Zn_{0.99}Cu_{0.01}$_800	7.1
$Zn_{0.90}Cu_{0.10}$_800	6.2

Looking at the data it is possible to state that the heat treatment markedly influences the surface area of powders, while the presence of copper does not substantially affect it.

Before relating the experimental results it is useful to consider the system used to identify the reaction products. Detecting the production of hydrogen in a quantitative way, using a *Quadrupole Mass Spectrometer*, is quite problematic given its low sensitivity to such a small mass value. However, exploiting the high sensitivity of FTIR spectroscopy it is possible to monitor the presence, even in trace quantities, of any by-products that might be formed during the catalytic process. Therefore, the combination of the two techniques provides a means of detection sufficiently reliable to determine directly and indirectly the production of hydrogen as a result of the *Methanol Steam Reforming* reaction.

Finally, it is worth noting that the catalytic tests were carried out on the samples as prepared, avoiding any activation or cleaning treatment. Furthermore, no significant catalyst deactivation is observed in the methanol conversion during subsequent follow-up experiments.

4.2.1 Methanol Conversion

The evolution of methanol conversion as a function of operating temperature is summarised in figure 1. The first experimental evidence is the activity of nanopowders as a function of the annealing conditions. Samples annealed at 400°C are characterised by a higher activity than the samples processed at 800°C, no matter the copper content.

In fact, catalysts of this series reach a methanol conversion higher than 80% when the reactor is kept at 400°C.

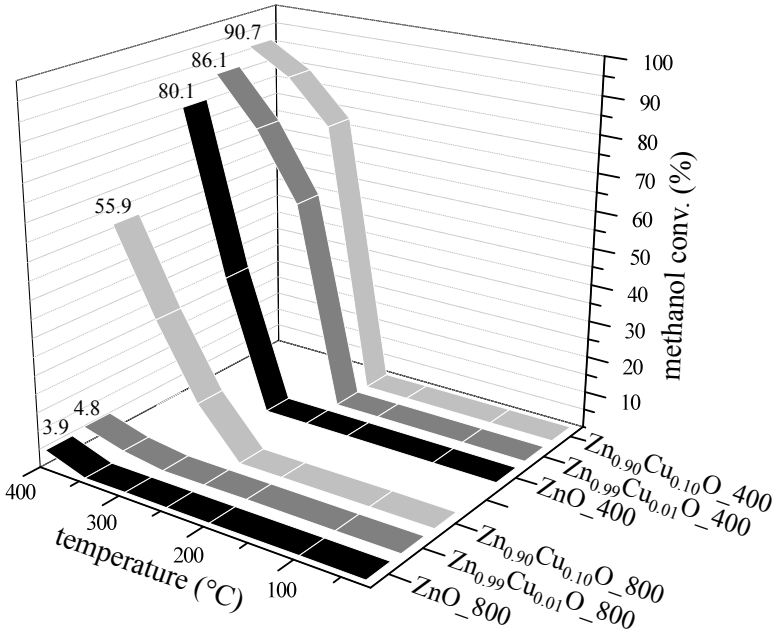

Figure 1: Methanol conversion plotted vs. the reaction temperature during MSR.

It is interesting to note that the ZnO_400 shows unexpected activity towards methanol steam reforming above 300°C. Moreover, its activity is enhanced by the temperature increase.

The introduction of copper enhances the catalytic performance, not only in terms of methanol conversion but also decreasing the temperature at which the reaction starts to take place. In fact, both the Cu-doped ZnO samples annealing at 400°C show a significant methanol conversion above 250°C which increases with temperature. Consistent with the beginning of catalyst activity a powder colour change is observed: sample $Zn_{0.99}Cu_{0.01}O$_400 changed from green to light grey, while $Zn_{0.90}Cu_{0.10}O$_400 turned from brown to black. This colour alteration is symptomatic of a change in copper oxidation state, as will be confirmed later on in the chapter, with characterisation of the exhaust catalysts. Peculiar behaviour can be observed for sample $Zn_{0.9}Cu_{0.1}O$_800 which shows much higher activity when compared with the other powder synthesised with the same heat treatment.

This experimental evidence clearly shows that there is an active involvement not only of copper but also of the zinc oxide, in the catalytic process. A detailed analysis of the reaction products will help to produce some interesting considerations about the selectivity of these catalytic systems.

4.2.2 Selectivity of Process

The presence of undoped ZnO, independent of its synthetic treatment, drives the catalytic reaction to the exclusive formation of hydrogen and CO_2. Figure 2 shows the catalytic profiles of samples ZnO_400 and ZnO_800, respectively.

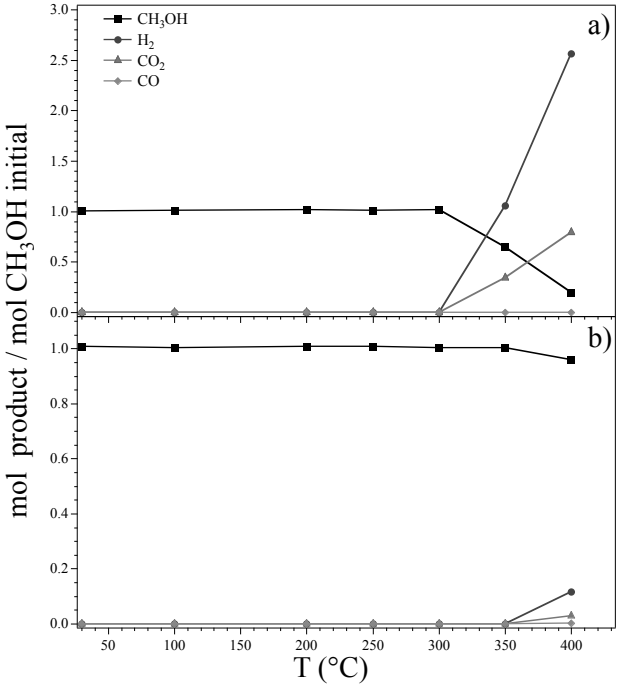

Figure 2: Catalytic activity profiles of the undoped samples **a)** ZnO_400 **b)** ZnO_800.

In the reactor containing ZnO_400 (figure 2a), the evolution of H_2 and CO_2 starts when the working temperature reaches 300°C and the catalytic activity increases with increasing temperature. A good selectivity over the whole range is maintained, indicating that steam reforming is the primary reaction. The FTIR spectra, not reported here, underline the absence of any by-products, and in particular no carbon monoxide is detected.

Sample ZnO_800 (figure 2b) shows similar behaviour even if the total methanol conversion is almost negligible (< 5%). As in the previous case, the system evolves only hydrogen and CO_2 and no by-products are detectable in the FTIR spectra.

From these considerations, it can be inferred that the synthetic conditions of the catalyst, in particular the heat treatment which has a large influence on the structure and morphology, are key factors in achieving catalysts with different activity without affecting the reaction mechanism. In fact, ZnO_800 shows a very low, almost negligible, catalytic activity when compared to the analogous ZnO_400, but no by-products are detected in both cases.

The presence of copper in the ZnO matrix, as noted above, leads to a general increase in catalytic activity. However, it is necessary to examine the behaviour of samples with different copper content separately: the presence of phase segregation, as observed in some of the samples, could involve different changes in the catalytic process.

In figure 3 the catalytic profiles of samples with low dopant content, $Zn_{0.99}Cu_{0.01}O$_400 and $Zn_{0.99}Cu_{0.01}O$_800 respectively, are reported. The sample annealed at 400°C shows a significant methanol conversion above 250°C which increases with temperature. As in the case of the undoped samples, powder treated at 800°C is less active in the catalytic process.

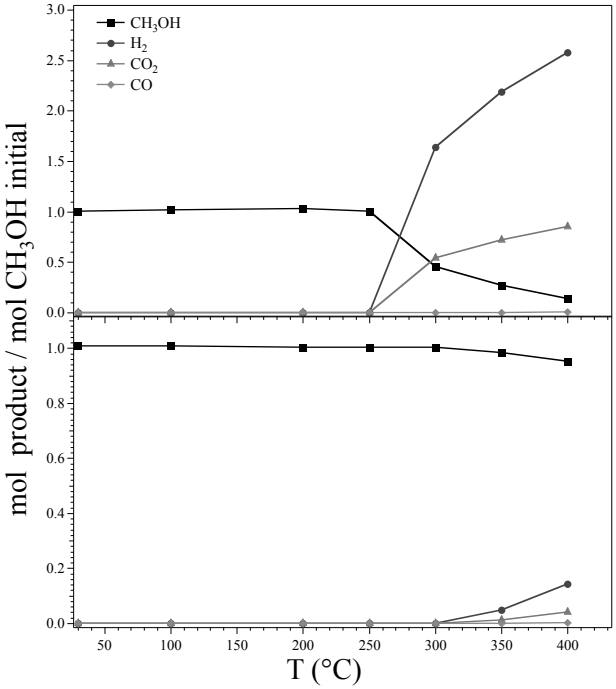

Figure 3: Catalytic activity profiles of the samples **a)** $Zn_{0.99}Cu_{0.01}O$_400 **b)** $Zn_{0.99}Cu_{0.01}O$_800.

As in the case of the pure ZnO, hydrogen and carbon dioxide are the main products, but small traces of CO are detected in the FTIR spectra (not shown here) when the reactor reaches 400°C. This suggests that the presence of a secondary reaction cannot be excluded: methanol decomposition is, in fact, favoured at high temperature.

This experimental data makes it clear that the presence of copper, even in low concentrations, plays an active role in the catalytic process. In terms of methanol conversion, which increases several percentage points, and also operating temperature, as the evolution of H_2 is detected above the low reactor temperature of 250°C. However, the presence at high operating temperature of traces of CO, as a by-product, indicates that the process may follow a secondary path, such as methanol decomposition. Its limited formation, detected only with the FTIR, suggests that the loss

of catalytic selectivity is minimal. The trend, observed for the undoped catalyst, in function of the synthetic treatment, fully corroborates the key role of the micro-structural properties of the material, stated above.

Nanopowders with higher copper concentration, $Zn_{0.90}Cu_{0.10}O$, showed a slightly different catalytic behaviour compared with the previous ones. In figure 4 the catalytic profiles of samples with high dopant content are reported.

Again, the trend in function of the synthetic treatment is confirmed, but sample $Zn_{0.90}Cu_{0.10}O\_800$ displays significant activity towards methanol conversion above 250°C which increases with temperature: the maximum value reached is 55.8% at a reaction temperature of 400°C.

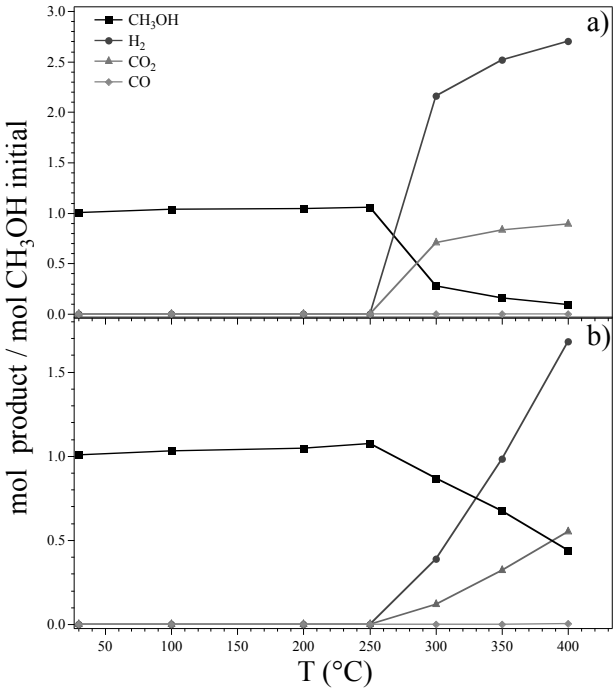

Figure 4: Catalytic activity profiles of the samples **a)** $Zn_{0.90}Cu_{0.10}O\_400$ **b)** $Zn_{0.90}Cu_{0.10}O\_800$.

As well as hydrogen and carbon dioxide, looking at FTIR spectra (not shown here), it is possible to detect the presence of additional by-products, although merely in trace amounts. As in the case of both $Zn_{0.99}Cu_{0.01}O$ samples with lower copper content, $Zn_{0.90}Cu_{0.10}O\_400$ leads to the production of trace quantities of CO when the operating temperature reaches 400°C, this is consistent with the presence of a competitive reaction of methanol decomposition. When $Zn_{0.90}Cu_{0.10}O\_800$ catalyst is used, evolution of small traces of formaldehyde is observed at operating temperatures of roughly 350°C - 400°C. The presence of formaldehyde is consistent with the methanol dehydrogenation reaction: $CH_3OH \rightarrow CH_2O + H_2$. The limited formation of by-products, detected only with the FTIR, suggests that, in both cases, the loss of catalytic selectivity is minimal.

4.2.3 Post Reaction Characterisation

For a better comprehension of the active sites involved in the MSR, structural and compositional characterisations were performed on all the exhaust catalysts. This should, in principal, provide important information about the micro-structural and compositional changes that occur in the catalyst during activity.

Figure 5 reports a comparison between XRD patterns before and after the catalytic activity of undoped ZnO and $Zn_{0.99}Cu_{0.01}O$ series, respectively. No significant changes are detectable for all nanopowders displayed, indicating that there are no evident structural distortions and the average crystallinity and particle size are maintained.

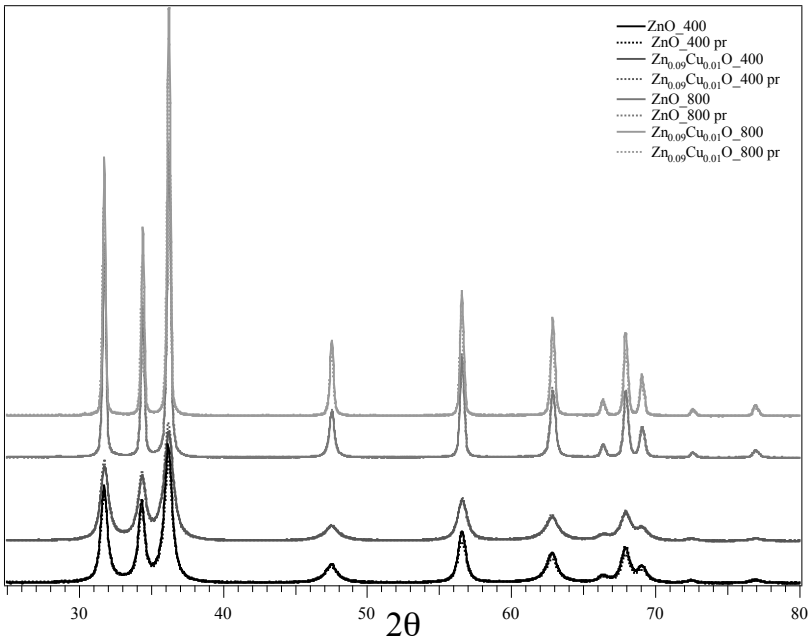

Figure 5: XRD patterns obtained for samples before (solid lines) and after MSR reaction (dashed lines).

As it can be well observed in figure 6, the most significant structural changes are observed in the samples of the series $Zn_{0.90}Cu_{0.10}O$, after their catalytic activity. These as-prepared compounds, upon characterisation, showed the presence of two different crystalline phases, ZnO and CuO. In the exhaust powders, the reflections due to copper oxide disappear while new small reflections reveal the presence of cubic metallic copper. During the catalytic activity, the copper undergoes a reduction from Cu(II) to Cu(0), probably due to the reducing environment that is created by evolution of hydrogen when the steam reforming reaction takes place. In fact, the beginning of catalyst activity consistently also saw a change in powder colour. Vice versa, regarding the zinc oxide phase (figure 5), no significant changes are observed and the average crystallinity of the system is maintained as well as the average particle size.

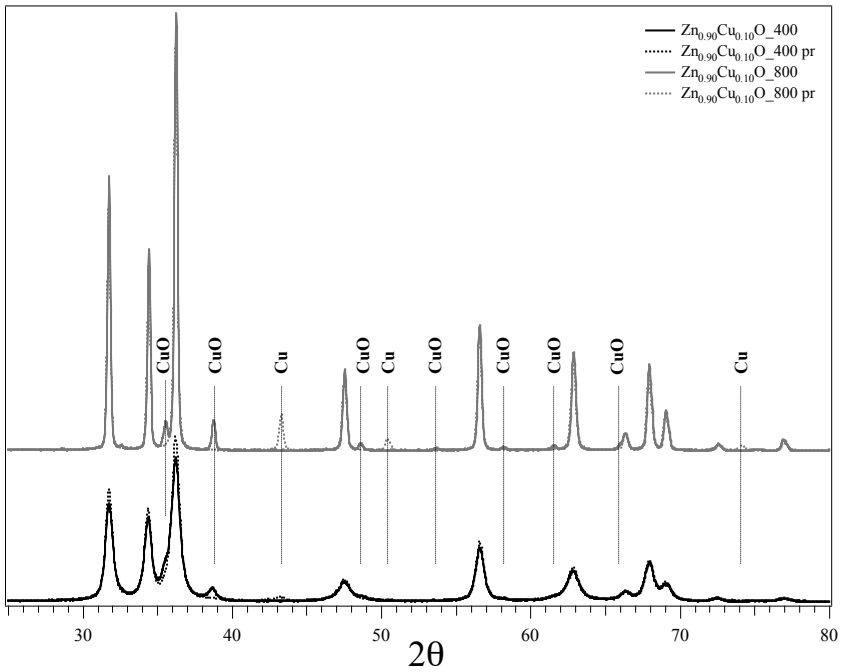

Figure 6: XRD patterns obtained for samples before (solid lines) and after MSR reaction (dashed lines).

The copper reduction during the catalytic reaction is also confirmed by XPS on the exhaust powders. Figure 7 shows a comparison between *Cu2p* peaks of the two series of $Zn_{1-x}Cu_xO$ compounds before and after the catalytic experiments.

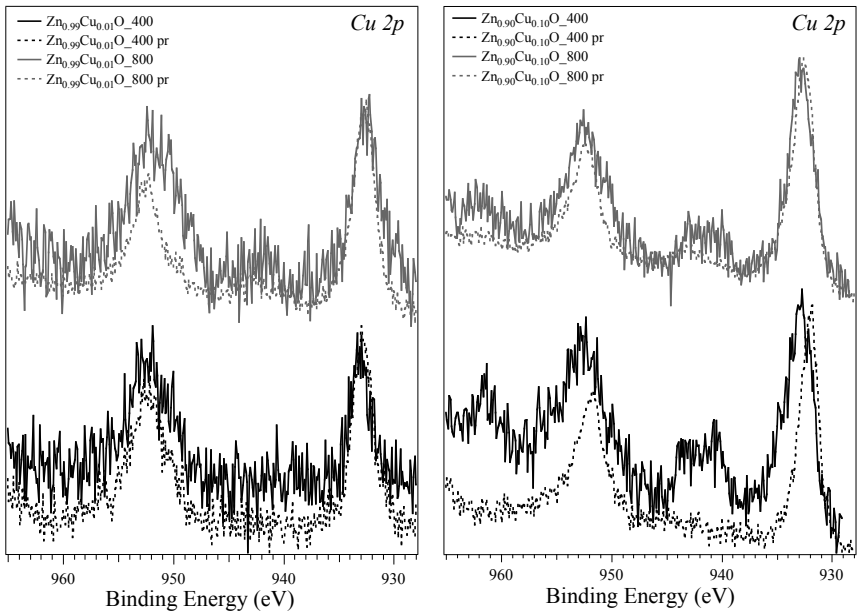

Figure 7: *Cu2p* XP spectra of the as prepared samples (solid line) and after MSR reaction (dotted line).

As an example, in $Zn_{0.90}Cu_{0.10}O$_400 the shift towards lower BE of the *Cu2p* peak as well as the disappearance of the shake-up contributions is due to the presence of metallic copper, Cu(0), in the exhaust powder surface. In the analogous sample treated at 800°C, $Zn_{0.90}Cu_{0.10}O$_800, it is instead possible to state that the Cu(II) is not

completely reduced after the catalytic activity. The higher FWHM of the *Cu2p* doublet as well as the small shake-up peaks, in fact, suggest the presence of several different types of copper, in particular, Cu(II) and Cu(0), on the surface of the catalyst.

The analysis of samples with lower copper concentration ($Zn_{0.99}Cu_{0.01}O$) is somewhat more complex. In fact, the *Cu2p* peak position and shape for the exhaust powders undergo less evident changes. It's quite clear that a reduction of the copper took place but not possible to state if it has been complete or only partial. Unfortunately, the *Cu2p* signal intensity is not very high, due to the low copper concentration, and it is therefore more difficult to determine unequivocally that small changes in the peak are due to compositional changes.

Table 2 reports the calculated XP atomic composition, in particular the ratio between copper and zinc, of the catalysts before and after their activity. Looking at the exhaust samples, the increase of the Cu/Zn atomic ratio suggests copper segregation to the surface. This effect is more marked for samples with high copper concentration, where the segregation of reduced copper was also detected by XRD.

Table 2: XPS composition, in particular the ratio between Cu/Zn, of different catalyst before and after MSR reaction.

Samples	**nominal Cu/Zn**	**XPS Cu/Zn**
ZnO_400	--	--
ZnO_400 pr	--	--
$Zn_{0.09}Cu_{0.01}O$ _400	0.01	0.03
$Zn_{0.09}Cu_{0.01}O$ _400 pr	0.01	0.06
$Zn_{0.90}Cu_{0.10}O$ _400	0.10	0.08
$Zn_{0.90}Cu_{0.10}O$ _400 pr	0.10	0.09
ZnO_800	--	--
ZnO_800 pr	--	--
$Zn_{0.99}Cu_{0.01}O$ _800	0.01	0.04
$Zn_{0.99}Cu_{0.01}O$ _800 pr	0.01	0.14
$Zn_{0.90}Cu_{0.10}O$ _800	0.10	0.08
$Zn_{0.90}Cu_{0.10}O$ _800 pr	0.10	0.22

Figure 8 reports the XP spectra relative to the *O1s* and $Zn2p_{3/2}$ for all catalysts before and after their catalytic activity.

ZnO undoped powders do not undergo any particular compositional changes during catalytic activity and both signals related to the presence, on the surface, of oxygen (*O1s* peak) and zinc ($Zn2p_{3/2}$) remain almost unaltered.

The reduction of Cu(II) to metallic copper is also confirmed by the analysis of the *O1s* peaks. In fact, the contribution at ~529.6 eV, characteristic of reticular oxygen in CuO, disappears in both Cu-doped samples treated at 800°C.

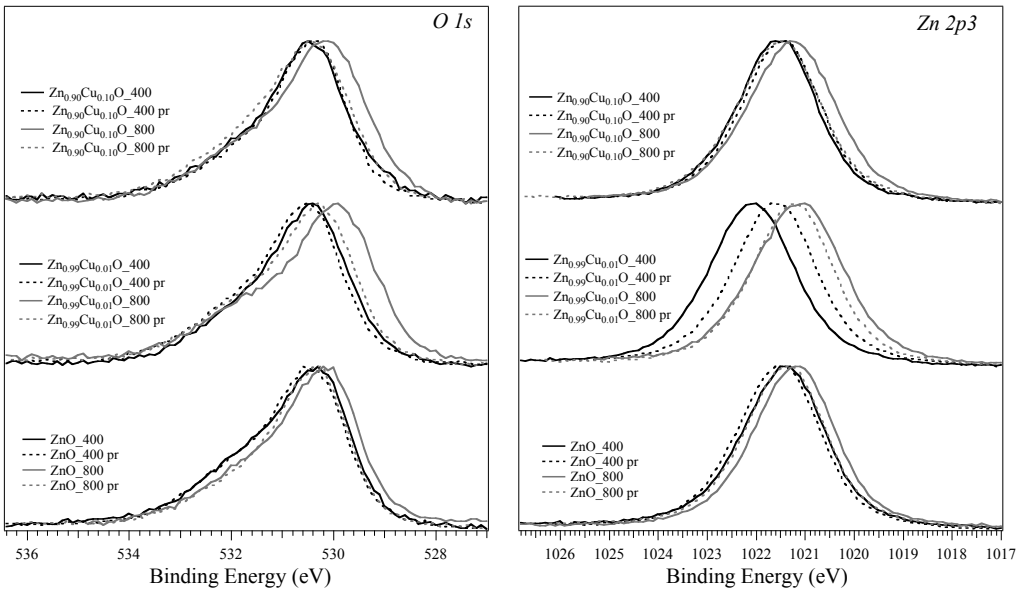

Figure 8: *O1s* XP spectra of the as prepared samples (solid line) and after MSR reaction (dotted line) *Zn2p3/2* XP spectra of the as prepared samples (solid line) and after MSR reaction (dotted line).

Concerning the *Zn2p3/2* peak it is of note that in the $Zn_{0.99}Cu_{0.01}O$_400 exhaust sample a significant shift towards lower binding energy is quite evident. It is worth recalling that in the as-prepared powder, the position of zinc signal at higher binding energy was related to the more intimate interaction with the copper ions. Charge transfer between the zinc and copper ions could be responsible for the unusual position. During the catalytic activity, when the copper(II) is reduced, the chemical environment changes and this could explain the shift in zinc signal.

Table 3: XPS peak positions (Binding Energy, eV) of *Zn2p3/2*, *Cu2p3/2*, *O1s* (reported all the components) related to the different catalysts before and after MSR reaction.

Samples	*Zn2p3/2*	*Cu2p3/2*	*O1s*
ZnO_400	1021.4		530.3 / 531.7
ZnO_400 pr	1021.5		530.4 / 531.8
$Zn_{0.09}Cu_{0.01}O$ _400	1022.1	933.1	530.4 / 531.9
$Zn_{0.09}Cu_{0.01}O$ _400 pr	1021.6	932.9	530.5 / 532.1
$Zn_{0.90}Cu_{0.10}O$ _400	1021.5	932.9	530.4 / 532.0
$Zn_{0.90}Cu_{0.10}O$ _400 pr	1021.5	931.8	530.4 / 531.8
ZnO_800	1021.1		530.1 / 531.6
ZnO_800 pr	1021.4		530.4 / 531.8
$Zn_{0.99}Cu_{0.01}O$ _800	1021.2	932.5	529.6 / 530.2 / 531.9
$Zn_{0.99}Cu_{0.01}O$ _800 pr	1021.2	932.5	530.3 / 531.9
$Zn_{0.90}Cu_{0.10}O$ _800	1021.2	932.8	529.7 / 530.3 / 532.0
$Zn_{0.90}Cu_{0.10}O$ _800 pr	1021.5	932.4	530.3 / 531.8

Finally, the binding energies of the XPS peaks measured for all catalysts are summarised in table 3; samples are reported before and after their catalytic activity. In the case of the oxygen signal (*O1s*) the position of the different components, obtained after deconvolution, are quoted.

4.3 Summary and Conclusion

In this chapter, the catalytic performances of zinc oxide based nanopowders towards the *Methanol Steam Reforming* reaction (MRS) have been reported.

Catalysts based on ZnO doped with copper are the most industrially used for hydrogen production from steam reforming of methanol. As a consequence of their success these systems have prompted a great deal of fundamental work devoted to elucidating the role played by each component and the nature of the active sites.

There is general agreement about the central role played by the copper, even though there is not yet a full consensus regarding the metal oxidation state actually active in the process. On the other hand, ZnO is believed, as other semiconductors used to disperse copper particles, to primarily act as catalytic promoter influencing the reducibility of CuO and to improve the stability of the catalyst preventing the sintering of the copper which is one of the primary causes of deactivation of the catalyst.

The results obtained in this study demonstrate, on the contrary, that ZnO also plays a prominent role in steam reforming of methanol. In fact, ZnO calcined at 400°C shows unexpected catalytic activity above reactor temperatures of 300°C that increases with the temperature: the methanol conversion is about 80% when the reaction is driven at 400°C. The only products detected in the effluent gas are H_2 and CO_2 indicating that steam reforming is the main reaction. Furthermore, the good selectivity is maintained over the whole range of temperatures, and no secondary reactions have taken place. Conversely, the activity of ZnO_800 decreases drastically and the methanol conversion barely reaches 5% when the reactor is heated to 400°C.

These results, in line with some very recent literature[32,33], show that defects in the semiconductor, and more precisely oxygen vacancies, act as active sites. ZnO nanopowders synthesised via *Sol gel* synthesis, as seen in previous chapters, present different dimensionality and microstructure when treated at different temperatures. As

revealed by EPR spectroscopy (chapter 3), ZnO_400 presents different structural defects, in particular oxygen vacancies and shallow donors. When the semiconductor undergoes more severe heat treatment, above 800°C, the crystallinity of nanoparticles increases and consequently structural defects, such as oxygen vacancies, decrease.

The introduction of copper enhances the catalytic performance, not only in terms of methanol conversion rate but also decreasing the temperature at which the reaction starts to take place. Taking into consideration the Cu-doped ZnO nanopowders synthesised at 400°C, previous characterisations had revealed that the copper is mainly segregated to the surface. The higher catalytic performance of these samples is, besides the higher specific surface area, due to highly dispersed copper nanoparticles that are more accessible to methanol and steam. Concerning the samples annealed at 800°C, high activity is observed only in samples with a higher concentration of copper, $Zn_{0.90}Cu_{0.10}O$_800. When copper is present in low quantities the high thermal treatment favours its diffusion into the ZnO matrix as demonstrated previously. Consequently a lower number of active copper species exist on the surface.

Samples with different copper content show slightly different behaviour, in particular in terms of selectivity and reaction path. In fact, in contrast with the case of the undoped zinc oxide, catalysts containing copper enable the evolution of by-products. The loss of selectivity, in both cases, is not significant and only traces of by-products are detected with FTIR spectroscopy.

In particular, the evolution of carbon monoxide was detected during high temperature activity, when the reactor is heated to about 400°C, of the $Zn_{0.99}Cu_{0.01}O$ series of compounds. This is compatible with the presence of a competitive reaction, such as methanol decomposition, which is activated at high temperature. Additionally, looking at catalysts with higher dopant concentration, in particular sample $Zn_{0.90}Cu_{0.10}O$_800, evolution of small traces of formaldehyde is observed at operating temperatures of about 350°C - 400°C. The presence of formaldehyde as by-product is consistent with the initiation of a competitive pathway, specifically the methanol dehydrogenation reaction: $CH_3OH \rightarrow CH_2O + H_2$.

The structure–activity relationship of ZnO and copper-doped ZnO catalysts described in this chapter, and the possibility to tailor the “real structure” of a catalyst during preparation, are a step towards a rational design of improved catalysts.

References:

[1] D.R. Palo, R.A. Dangle, J.D. Holladay, *Chem. Re*v. **107** (2007) 3992

[2] L.F. Brown, *Int. J. Hydrogen Energy* **26** (2001) 381

[3] N. Hickey, P. Fornasiero, M. Graziani, *Hydrogen* Based Technologies for Mobile Applications. In *Renewable Resources and Renewable Energy: A Global Challenge*; M. Graziani, P. Fornasiero, Eds.; Taylor & Francis: New York. (2006); Chapter 11, pp 225–272

[4] S. Sá, H. Silva, L. Brandão, J.M. Sousa, A. Mendes, *Applied Catalysis B: Environmental* **99** (2010) 43

[5] J. Papavasiliou, G. Avgouropoulos, T. Ioannides, *Appl. Catal. B* **88** (2009) 490

[6] P.H. Matter, D.J. Braden, U.S. Ozkan *Journal of Catalysis* **223** (2004) 340

[7] J. Agrell, M. Boutonnet, J.L.G. Fierro, *Appl. Catal. A* **253** (2003) 213

[8] S.D. Jones, L.M. Neal, H.E. Hagelin-Weaver, *Appl. Catal. B* **84** (2008) 631

[9] H. Purnama, T. Ressler, R.E. Jentoft, H. Soerijanto, R. Schlogl, R. Schomacker, *Appl. Catal. A* **259** (2004) 83

[10] T. Valdes-Solis, G. Marban, A.B. Fuertes, *Catalysis Today* **116** (2006) 354

[11] M. Ni, D.Y.C. Leung, M.K.H. Leung, *International Journal of Hydrogen Energy* **32** (2007) 3238

[12] S. Velu, K. Suzuki, M. Vijayaraj, S. Barman, C.S. Gopinath, *Appl. Catal. B* **55** (2005) 287

[13] N. Homs, J. Llorca, P. Ramirez de la Piscina, *Catal. Today* **116** (2006) 361

[14] J. Llorca, P. Ramirez de la Piscina, J.A. Dalmon, J. Sales, N. Holms, *Appl. Catal. B* **43** (2003) 355

[15] Y. Chen, Y. Wang, H. Xu, G. Xiong, *J. Membr. Sci.* **322** (2008) 453

[16] D.L. Hoang, S.H. Chan, O.L. Ding, *J. Power Sources* **159** (2006) 1248

[17] G.A. Olah, A. Goeppert, G.K.S. Prakash, *Beyond Oil and Gas: The Methanol Economy*, 2nd ed., WILEY-VCH Verlag GmbH & Co. KGaA, Weinheim (2006)

[18] H. Purnama, F. Girgsdies, T. Ressler, J.H. Schattka, R.A. Caruso, R. Schomacker, R. Schlogl, *Catal. Lett.* **94** (2004) 61

[19] P.H. Matter, D.J. Braden, U.S. Ozkan, *J. Catal.* **223** (2004) 340

[20] C.S. Cao, G. Xia, J. Holladay, E. Jones, Y. Wang, *Appl. Catal. A* **267** (2004) 9

[21] Y. Choi, H.G. Stenger, *Appl. Catal. B* **38** (2002) 259

[22] H.P. Dhar, L.G. Christner, A.K. Kush, *J. Electrochem. Soc.* **134** (1987) 3021

[23] C.Z. Yao, L.C. Wang, Y.M. Liu, G.S. Wu, Y. Cao, W.L. Dai, H.Y. He, K.N. Fan, *Appl. Catal. A* **297** (2006) 151

[24] A.M. Karim, T. Conant, A.K. Datye, *Phys. Chem. Chem. Phys.* **10** (2008) 5584

[25] T. Shishido, Y. Yamamoto, H. Morioka, K. Takaki, K. Takehira*, Appl. Catal. A* **263** (2004) 249

[26] G. Águila, J. Jiménez, S. Guerrero, F. Gracia, B. Chornik, S. Quinteros, P. Araya, *Appl. Catal. A* **360** (2009) 98

[27] G. Fierro, M. Lo Jacono, M. Inversi, P. Porta, F. Cioci, R. Lavecchia, *Appl. Catal. A,* **137** (1996) 327

[28] M.M. Gunter, T. Ressler, R.E. Jentoft, B. Bems, *J. Catal.* **203** (2001) 133

[29] G. Natta, *Synthesis of Methanol in Catalysis Vol. 3*, Reinhold Publishing Corporation, New York, (1955) pp 349

[30] J. Strunk, K. Kähler, X. Xia, M. Muhler, *Surf. Sci.* **603** (2009) 1776

[31] G.C. Chinchen, P.J. Denny, J.R. Jennings, M.S. Spencer, K.C. Waugh, *Appl. Catal.* **36** (1988) 1

[32] J. Strunk, K. Kähler, X. Xia, M. Comotti, F. Schüth, T. Reinecke, M. Muhler, *Appl. Catal. A* **359** (2009) 121

[33] K. Kähler, M.C. Holz, M. Rohe, J. Strunk, M. Muhler, *Chem. Phys. Chem.* **11** (12) (2010) 2521

Chapter 5

Optical Properties of $Zn_{1-x}TM_xO$ *(TM = Mn, Co, Cu)*

PART 1. UV-Vis Absorption Spectroscopy

5.1 Introduction

Optical properties of a semiconductor are products of both intrinsic and extrinsic effects. Intrinsic optical transitions take place between the electrons in the conduction band and holes in the valence band, including excitonic effects due to coulombic interaction. Extrinsic properties are related to the presence of dopants or defects, which usually create electronic states in the band-gap and therefore influence both optical absorption and emission processes.

For a semiconductor to be useful, particularly with regard to optoelectronic devices, band gap engineering is a crucial step in device development. By doping the initial semiconductor with another material, the band gap of the resultant alloy can be fine tuned, thus affecting the wavelength of exciton emissions. On the other hand, doping with transition metal ions could create localised electronic states in the band-gap of the semiconductor, influencing the properties of the final material.

5.1.1 ZnO Band-gap

The electronic band structure of ZnO has been calculated by a number of groups[1-4]. This semiconductor has a direct band gap (E_g), in which the conduction bands correspond to Zn*3d* levels and the valence bands correspond, primarily, to O*2p* bonding states. The first two conduction band states are strongly zinc localised and correspond to empty Zn*3s* levels. The band-gap determined from calculations[1-4] is 3.77 eV; this correlates reasonably well with the experimental value of 3.4 eV.

As mentioned above, the optical properties of ZnO are heavily influenced by the energy band structure and lattice dynamics. For a comprehensive review of the optical properties refer, e.g., to the work of B.K. Meyer et al[5].

The most obvious optical effect occurring in semiconductors is the transition from the optical transparency for photons with energies $h\nu < E_g$ to the strong absorption of photons with $h\nu > E_g$. Two types of transition can occur: direct or indirect. In a direct transition, an electron is promoted vertically on an energy band diagram from the valence band to the conduction band, and hence there is little change in the electron's wave vector. The energy of the initial and final state are related by $E' = E + h\nu$. In an indirect transition phonon emission or absorption (of a thermally activated phonon) occurs; thus $E' = E + h\nu \pm h\Omega(\vec{q}_{ph})$ and $\vec{k}' = \vec{k} \pm \vec{q}_{ph}$. Since a phonon perturbation is involved, indirect transitions are weaker than direct transitions.

5.1.2 Transition Metal Ions Doped ZnO

The presence of a dopant in the semiconductor, which usually creates electronic states in the band-gap, influences the optical properties of the final materials. In particular, doping with 3d transition-metal (TM) ions offers an effective method to adjust the electrical, magnetic and optical properties of zinc oxide.

The spectral characteristics of the $3d^n \rightarrow 3d^{n*}$ transition in transition metal ions can be interpreted based on crystal field theory (ligand field theory)[6]. The *d* orbitals are fivefold degenerate in the free ion state. If a crystal field of cubic symmetry is applied, the orbitals are split into threefold degenerate t_{2g} orbitals (composed of $d_{(xy)}$, $d_{(yz)}$, and $d_{(xz)}$ orbitals) and twofold e_g orbitals ($d_{(x^2-y^2)}$ and $d_{(z^2)}$ orbitals). In the case of octahedral symmetry, t_{2g} is lower in energy than e_g, while the opposite is true in the case of

tetrahedral symmetry. The energy difference between split e_g and t_{2g} levels is expressed by 10 *Dq*, a parameter showing the strength of the crystal field, which is given approximately by $10Dq \approx 5eqa4/3r5$ where *q* is the charge of the ligand, *a* is the radius of the *d* orbit, and *r* is the distance between the metallic ion and the ligand. The presence of inter-electronic repulsion, further removes the degeneracy of the orbitals in different terms[8].

Transitions between states with the same parity, such as $d \rightarrow d$ transitions, are forbidden (Laporte rule). However, this symmetry selection rule can be "relaxed" through coupling between vibrational and orbital functions[6]. One broadening effect of the $d \rightarrow d$ absorption bands is due to the vibrational motion of the ligands varying the M-L distance and essentially sweeping a range of *Dq*.

In the case of manganese, the Mn^{2+} ion has d^5 configuration, there are no spin-allowed transitions as there is only one sextet $^6A_{1g}$. It is possible to observe some weak spin-forbidden transitions, involving quartet states.

Cobalt(II) ions, d^7 in the high spin state, are expected to show three spin-allowed bands corresponding to transition between quartet states. In the case of tetrahedral complexes, transitions involve the ground state $^4A_2$ and one of the other quartet terms.

Finally, for d^9 copper(II), a single absorption band is expected. The six-coordinate Cu^{2+} complexes are usually distorted from regular octahedrons and four-coordinate complexes tend to be distorted from regular tetrahedrons. The distortion and spin-orbit coupling can contribute to the broadening of visible bands.

5.1.3 Experimental

Optical measurements (absorption/transmission) were made using a CARY 5E (Varian) spectrophotometer. Spectra were collected in diffuse reflectance in the range 200 – 1000 nm with a resolution of 0.5 nm.

5.2 Results: $Zn_{1-x}TM_xO$ (TM = Mn, Co, Cu)

In this section, the absorption properties of the doped $Zn_{1-x}TM_xO$ nanopowders will be presented. The results will be discussed in terms of different synthetic conditions (processing temperature, nature and content of dopant) as well as based on the structural information discussed in the previous chapters. These experiments will help to provide a better understanding of the electronic structure of the system.

First of all, the properties of the undoped ZnO depending on the processing temperature will be described. Different synthetic conditions affect the structural properties of the semiconductor and hence the electronic band structure can be tailored.

Absorption spectra of each of the three $Zn_{1-x}TM_xO$ systems will be described: results will be analysed in terms of dopant content and processing temperature to identify the evolution of the chemical environment of the transition metal ion.

5.2.1 Undoped ZnO

It is possible to derive, indirectly, the value of energy-gap (E_g) of the semiconductor through the analysis of the zinc oxide absorption in the UV-Visible region. Related spectra, for the undoped samples, are reported in figure 1.

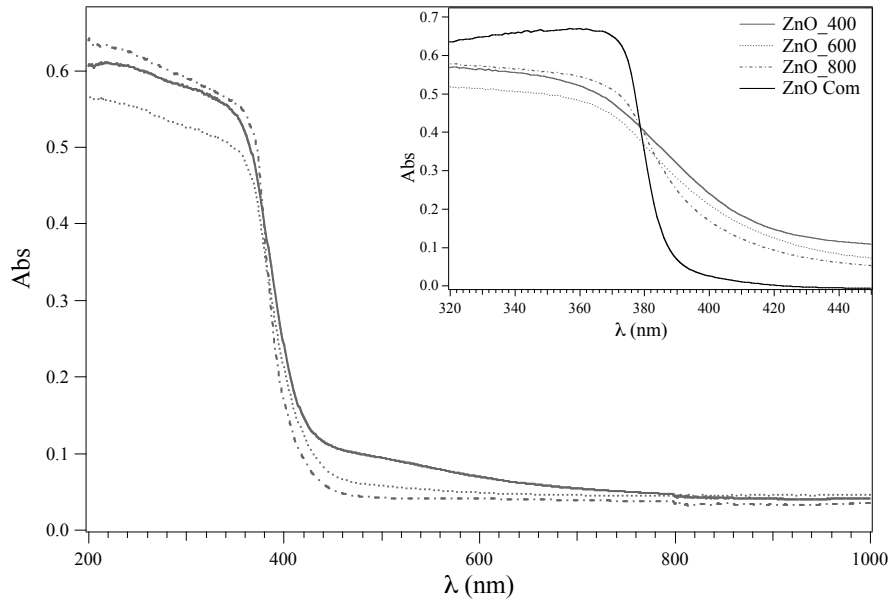

Figure 1: Absorption spectra, collected in diffuse reflectance, of pure ZnO nanopowders.

The ZnO nanopowders synthesised by *Sol gel* show a gap of about 2.9-3 eV, lower than commercial zinc oxide (Eg = 3.2 eV). The plot inset in figure 1 shows the

behaviour of the semiconductors as a function of the heat treatment. Increasing the temperature, there is a progressive shifting towards a higher gap. Further more, the edge of the absorption is less pronounced for the sample treated at lower temperature, ZnO_400, and its absorption is extended towards the visible portion of the spectrum. Consequently, the colour of these powders gradually changes from pale yellow (ZnO_400) to white (ZnO_800) with increasing processing temperature.

The variations from the bulk material used as reference could trace back to the highly defective structure typical of these nanostructured materials. In particular, it is possible to modify the visible fraction of absorbed light and the value of the band-gap by changing the synthetic condition of the powders.

5.2.2 $Zn_{1-x}Mn_xO$

Figure 2 reports absorption spectra of samples $Zn_{1-x}Mn_xO$, x = 0.01, in function of the heat treatment. For comparison also spectrum of ZnO_800 is displayed.

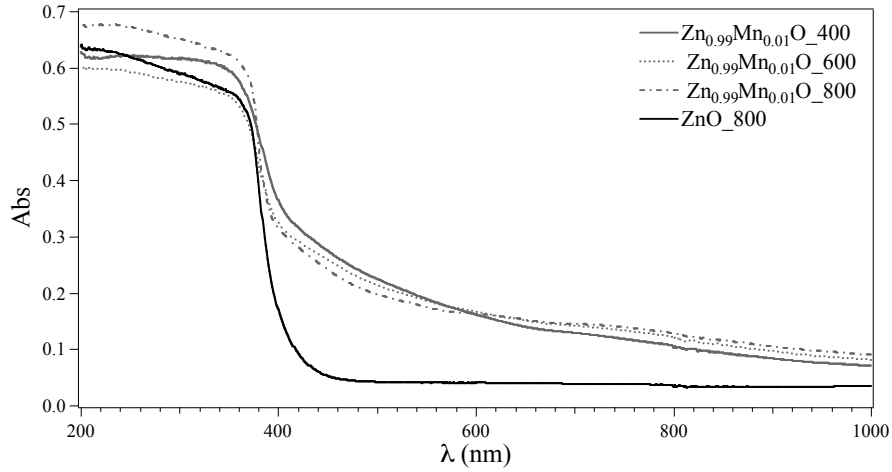

Figure 2: Absorption spectra, collected in diffuse reflectance, of $Zn_{0.99}Mn_{0.01}O$ series and ZnO_800.

As expected for Mn^{2+} (d^5) there are no visible bands due to d-d transition. However, the presence of metal ions influences the electronic spectra of the ZnO: the edge of the absorption is less pronounced and covers almost the entire range analysed. Usually, the optical absorption peak in Mn-doped II–VI compounds[8] is broad and structureless at room temperature owing to the overlap of the intra-d-shell transitions of Mn^{2+} from its ground state $^6A_1(S)$ to $^4T_1(G)$, $^4T_2(G)$, and $^4A_1(G)$, $^4E(G)$. Besides, the presence of manganese does not affect remarkably the position of the band-gap of ZnO. The trend in function of the heat treatment observed for the undoped samples is maintained.

Increasing the content of the manganese (spectra not shown here) there is an overall increase of the absorption in the visible part of the spectrum, but specific features are not detected. Moreover, the position of the ZnO band gap is almost in the same position as for the corresponding undoped samples: the trend in function of the treatment is maintained throughout.

5.2.3 $Zn_{1-x}Co_xO$

Optical absorption measurements were performed on all $Zn_{1-x}Co_xO$ (x = 0.01, 0.03 and 0.10) samples. The doped powders had a slight green tint that became more pronounced at higher cobalt concentrations. Spectra for $Zn_{0.99}Co_{0.01}O$ and $Zn_{0.97}Co_{0.03}O$ are shown in figure 3.

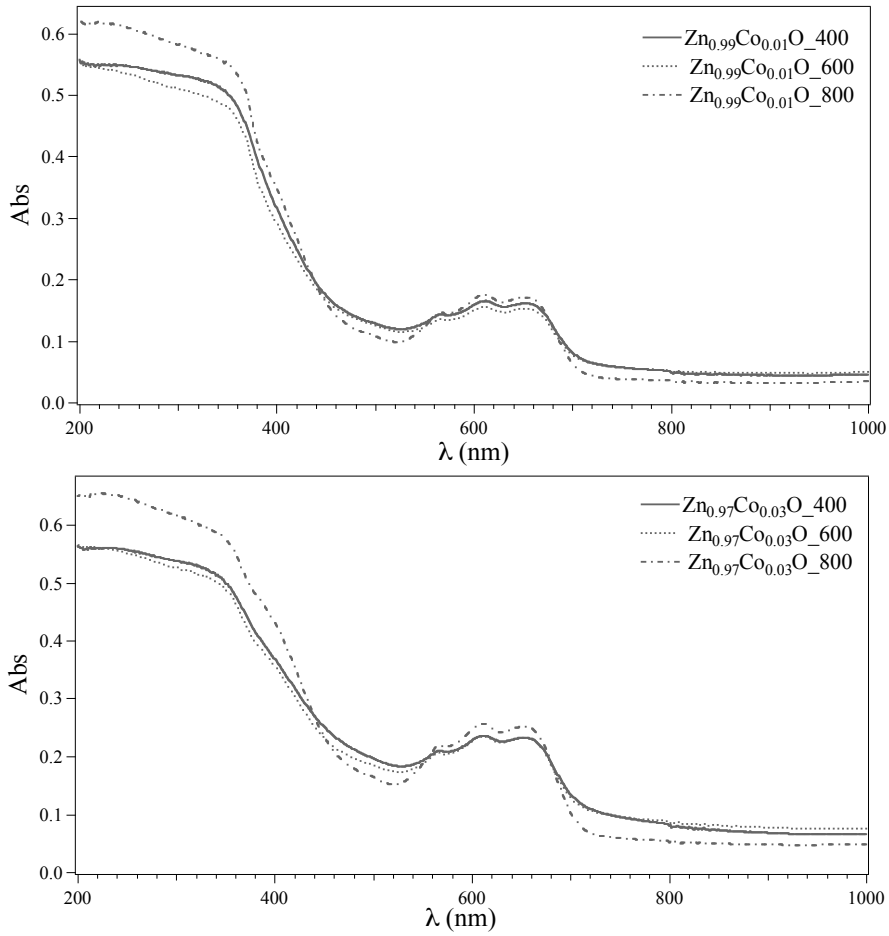

Figure 3: Absorption spectra, collected in diffuse reflectance, of $Zn_{1-x}Co_xO$, x= 0.01 and 0.03 series.

The spectra show characteristic absorption bands of Co^{2+} around 568 nm, 616 nm, and 658 nm, which are consistent with the presence of tetrahedrally coordinated Co^{2+} ions in a ZnO matrix[7]: transition from $^4A_2$ into $^4T_1(P)$ and the terms arising from ^2G lead

to the visible bands observed. Increasing the dopant content there is a general increase of the bands related to the presence of tetrahedral Co^{2+}.

Spectra of samples with higher dopant concentration, $Zn_{0.90}Co_{0.10}O$, not shown here, reveal the presence of another cobalt species, compatible with the mixed oxide Co_3O_4 detected by x-ray diffractions.

The general trends observed for the other systems, undoped and Mn-doped ZnO, regarding the position of the absorption edge of the semiconductors are maintained.

5.2.4 $Zn_{1-x}Cu_xO$

As seen in chapter 3, the solubility of copper in ZnO is lower than other metal ions, such as Mn or Co. Figure 4 reports the absorption spectra of the $Zn_{1-x}Cu_xO$ samples treated at 800°C, samples treated at 400 and 600°C showed similar behaviour.

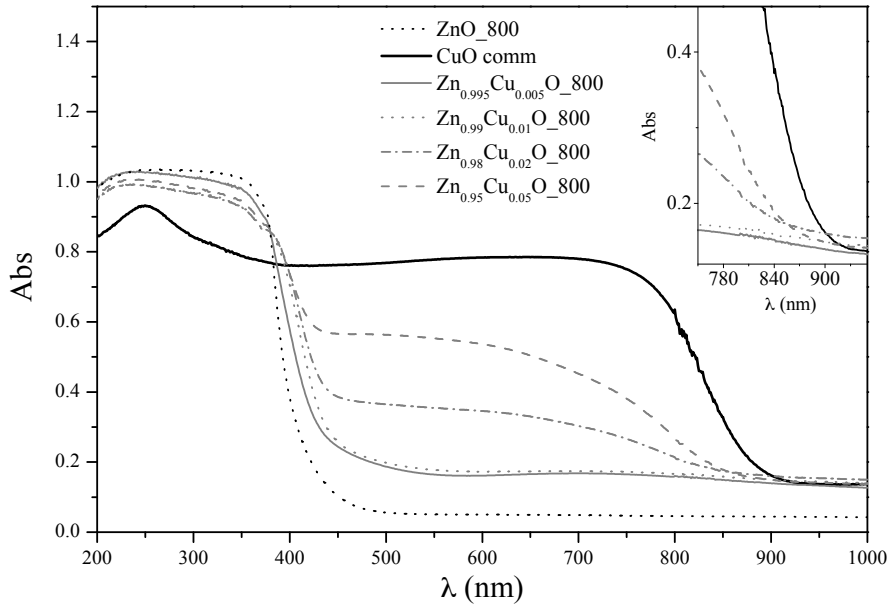

Figure 4: Absorption spectra, collected in diffuse reflectance, of $Zn_{1-x}Cu_xO$ systems treated at 800°C.

The absorption edge of ZnO is observed, as in previous cases, at about 400 nm. The semiconductor band gap is not affected by the presence of the dopant and the trend in function of the heat treatment is maintained.

Upon increasing the level of copper, a second edge centred at 820-860 nm appears indicating the formation of a secondary phase of CuO. The plot inset in figure 4 shows the rise of the onset relative to the copper oxide band edge. The trend is in agreement with results shown previously, such as XRD (chapter 2) or XAS (chapter 3).

5.3 Summary and Conclusion

Optical absorption measurements were performed on $Zn_{1-x}TM_xO$ (TM = Mn, Co and Cu) systems. These measurements could be used to determine, indirectly, the energy-gap (E_g) of the semiconductor. They could also be a useful tool to analyse the effect of the different metal ions on the electronic properties of the doped nanopowders.

ZnO synthesised via *Sol gel* shows a band gap of about 2.9-3 eV, depending on the processing temperature, which is slightly lower than that of commercial powders (E_g = 3.4 eV). The heat treatment does affect the electronic structure of the semiconductor due to the presence of defects. In particular, it is possible to modify the visible fraction of absorbed light and the value of the band gap, by changing the synthetic condition of the powders.

The presence of the various dopants influences the absorption spectrum of the final material in different ways. As in the case of $Zn_{1-x}Mn_xO$ there is an overall increase in absorption in the visible region of the light-spectrum but no specific features are detected, as expected for transition metal with d^5 electronic configuration.

On the other hand, it is possible to confirm the presence of tetrahedrally coordinated Co^{2+} in $Zn_{1-x}Co_xO$ systems where x = 0.01 and 0.03. In fact, the absorption spectra of these samples present features typical of substitutional cobalt in ZnO:Co, as reported in literature[7].

Finally, in the case of copper as dopant, it is possible to follow the evolution of the system $Zn_{1-x}Cu_xO$ in which a second phase of CuO starts to segregate even at very low dopant content. In fact, the absorption spectra of related compounds revealed the presence of two different absorption edges, due to the presence of two different semiconductors ZnO (edge ~ 400 nm) and CuO (edge ~850 nm).

PART 2. *X-ray Excited Optical Luminescence* (XEOL)

5.4 Introduction

The optical properties of pure and doped ZnO nanostructures are greatly dependant on the dopant, the intrinsic defect concentration and the crystallinity. Much attention has been paid to the quasi-free excitonic states, which become sensitive to confinement once the dilatation of the exciton Bohr radius is comparable to the particle size. The critical particle size where confinement in ZnO becomes important is ≤ 5 nm[1-3]. At larger particle sizes confinement effects quickly lose importance, but surface effects may still be significant[2-4]. Doping zinc oxide with transition metal ions (such as manganese, cobalt and copper) also offers an effective method to adjust its electrical and optical, as well as magnetic, properties.

It has been proven that element selective *X-ray Excited Optical Luminescence* (XEOL) of different sample morphologies is a suitable method to study phenomenological optoelectronic and structural correlations[5-7].

5.4.1 ZnO Photoluminescent (PL) Properties

XEOL of ZnO typically exhibits the band gap transition (~380 nm) and defect related transitions, often referred to as green band (~500 nm) and yellow band (~620 nm) [1-5,8].

The UV band has excitonic nature[4,8-9] but quantum confinement effects can be observed only in very small nanostructures (≤ 5 nm) due to the small size of the exciton Bohr radius in zinc oxide. Position of the near-band-edge emission at room temperature can, however, significantly vary due to variations in relative contributions of free exciton emission and phonon replicas, which will be dependent on synthesis conditions[3,9-10].

The green band originates from shallow trapped electrons and deep, trapped holes due to oxygen vacancies or interstitial zinc ions, which may appear together as a double-peak structure in the luminescence spectrum. The yellow tail towards long wavelengths is attributed to oxygen interstitials[3-4,8,11].

It is worth noting that many different hypotheses have been proposed to explain the visible emission of ZnO, but there is still no consensus[3,10]. In some cases, assignment is based on agreement between theoretical calculations and emission band positions, but in general this is not sufficient to conclusively make such a claim, especially as different calculations often give different predictions. Several theoretical studies of defects in ZnO have been reported[12-15]: different studies predict different energy levels for the same type of defect and consequently conclusive identification by a simple comparison of observed peak position and theoretically predicted defect energy level cannot be made.

The most commonly cited hypothesis for the origin of green emission remains singly ionised oxygen vacancies[3,8,16]. This identification was proposed based on the correlation with the EPR signal at g = 1.96, the free carrier concentration and the green PL intensity[3,16]. However, it was proposed that the EPR peak at g = 1.99 corresponds to oxygen vacancies, while g = 1.96 corresponds to shallow donors[17]. It was also shown that green emission does not necessarily coexist with an EPR signal at g = 1.96[18,19] and that this signal can appear in samples exhibiting yellow–orange emission[19].

5.4.2 *X-ray Excited Optical Luminescence*, XEOL

X-ray Excited Optical Luminescence (XEOL) is essentially an energy-transfer event in which the absorption of the X-ray photon produces a large number of energetic electrons (photo- and Auger electron). These electrons in turn cause further ionisation and excitation. The complex mechanism of XEOL involves the decay of super-excited states, but it is generally recognised that the radiative de-excitation channel in the optical region results from the effective coupling of the super-excited-state with the luminescence centre, producing electron-hole pairs that recombine radiatively[7,20]. The incoming energy is transferred to luminescent centres through inelastic processes, which lead to the creation of holes in the valence band and electrons in the conduction band in semiconductor nanostructures. Figure 5 presents a schematic representation of processes involved in XEOL for a semiconductor material.

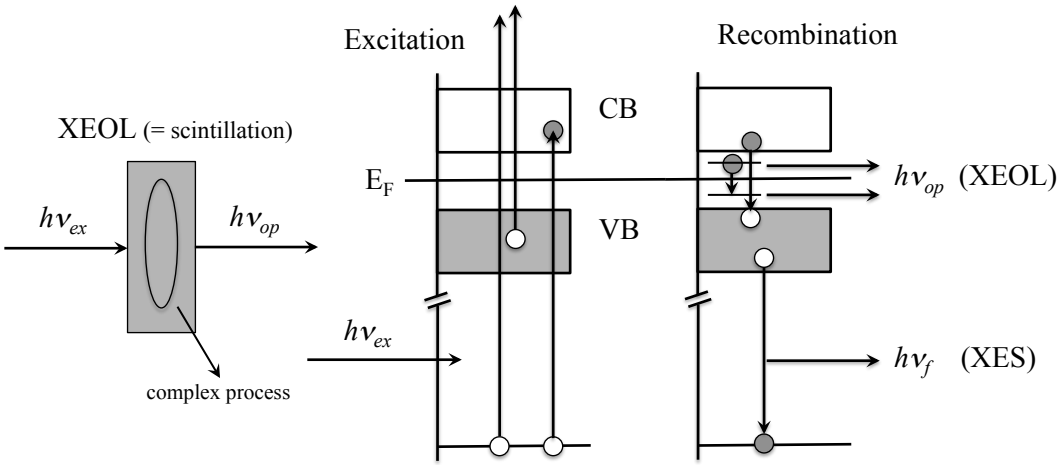

Figure 5: Schematic representation of processes involved in XEOL for a semiconductor.

XEOL is a photon in - photon out technique: using laboratory soft X-rays (20 eV - 3 keV) from a tuneable synchrotron light source, it is often possible to conduct site and sampling depth selective measurements[7,21-22]. The sampling depth selectivity comes from the energy-dependent penetration depth of the photons and the site selectivity, from the tunability of the source.

5.4.3 Experimental

Experiments were performed on the Spherical Grating Monochromator (SGM) 11ID-1 beamline (energy: 200-1900 eV, $\Delta E/E$: $<10^{-4}$) at the Canadian Light Source (CLS), University of Saskatchewan. XEOL spectra were recorded in the range of 200–850 nm with a J-Y H-100 optical monochromator equipped with a Hamamatsu R943–02 photomultiplier tube PMT, which has a monotonic, nearly flat optical response in this wavelength region.

XEOL spectra were recorded, exciting samples around various edges: *O-K* (520-580 eV), *Zn-$L_{3,2}$* (1020-1085 eV), *Co-$L_{3,2}$* (770-810 eV), *Mn-$L_{3,2}$* (635-665 eV), *Cu-$L_{3,2}$* (920-980 eV).

It is worth noting that XEOL spectra of all nanopowders show features that are independent of the photon-energy used to excite them. For that reason, only spectra excited at 540 eV, corresponding to the O *K*-edge, will be reported.

5.5 Results: $Zn_{1-x}TM_xO$ (TM = Mn, Co, Cu)

As described previously, XEOL is a suitable method to study phenomenological optoelectronic and structural correlations of the system under inspection.

In this section, the luminescence properties of the $Zn_{1-x}TM_xO$ nanopowders will be presented. The results will be discussed in terms of synthetic conditions (processing temperature, nature and content of dopant) as well as structural information. These experiments will help to provide a better understanding of the relationship between the electronic structure of the system and its properties.

For a better understanding of different $Zn_{1-x}TM_xO$ systems, it is fundamental to first describe the properties of the undoped ZnO depending on the processing temperature and to understand how the luminescence is affected by the synthesis condition.

XEOL spectra of each of the three $Zn_{1-x}TM_xO$ systems will be described: the emission will be analysed in terms of dopant content and processing temperature to identify the evolution of the system.

Finally, it will be very important to make a comparison between the different dopants to understand the role of each in modifying the optical properties of zinc oxide.

5.5.1 Undoped ZnO

Undoped ZnO exhibits XEOL features typical of this kind of material, as shown in figure 6a: a narrow band around 400 nm and a broad one in the visible region. The processing temperature significantly affects the emission spectrum, changing not only the relative intensity of the two signals but also the energy of the defects involved in the process. Upon increasing the processing temperature, the oxide's structure is modified and the optical properties are altered accordingly.

One of the challenges in identifying the origin of defect bands in ZnO is the fact that the bands are broad and overlapping; the use of Gaussian fitting to deconvolute peaks may lead to inaccurate peak position both due to the fact that emission bands are often asymmetric[23] and due to fitting uncertainties.

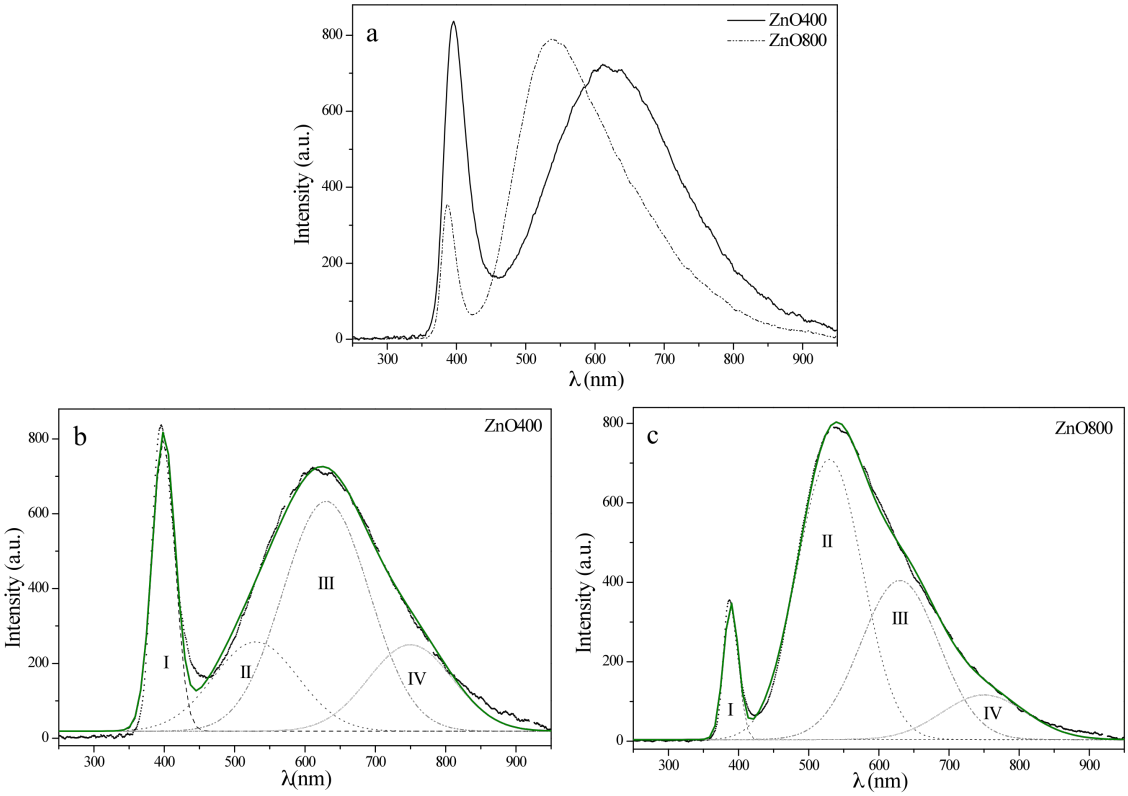

Figure 6: XEOL spectra of ZnO nanopowders excited at 1085 eV: **a)** comparison between different processing temperature **b)** peak fittings of ZnO_400 **c)** peak fitting of ZnO_800.

Figure 6b shows the deconvolution of XEOL spectrum for the samples treated at lower temperature, T = 400°C; peak position and relative intensity are displayed in table 1.

Table 1: Peak fits for sample ZnO_400.

	Peak Position (nm)	**%**
Peak I	~ 399	16
Peak II	~ 530	18
Peak III	~ 630	48
Peak IV	~ 750	18

This fitting shows the presence of several contributions: the band gap transition (peak I) and three defect related transitions in the visible part of the spectrum. The green component around ~ 530 nm (peak II) could be associated with the presence of oxygen vacancies or interstitial zinc ions[3,8-9,23].

The yellow tail towards long wavelengths, peak III, could be attributed to oxygen interstitials[3,8,24]. It is, however, possible to attribute it to the presence of hydroxyl groups[3,25-26]. The presence of -OH groups in ZnO nanoparticles prepared by *Sol gel* synthesis is due, not only to zinc hydroxide shell covering the surface, but also to an incomplete reticulation of metal ions via oxygen bridges.

Finally, the presence of peak IV at around ~ 750 nm can be ascribed to the presence of oxygen-related defects or zinc interstitials[3,27].

Table 2: Peak fits for sample ZnO_800.

	Peak Position (nm)	**%**
Peak I	~ 390	6
Peak II	~ 530	50
Peak III	~ 630	34
Peak IV	~ 750	10

Upon increasing the processing temperature the relative intensity of different contributions changes (sample ZnO_800 reported in figure 6c, table 2 displays peak fitting). The position of the near-band-edge emission is shifted to shorter wavelength and its intensity is considerably decreased. The yellow band (peak III) also decreases: the hydroxyl's contribution becomes significantly less pronounced with increasing processing temperature. For this synthetic condition, the green emission is greatly enhanced and the luminescent spectrum is predominantly characterised by this contribution.

It's worth noting that the emission properties of the undoped ZnO are not site specific, i.e. zinc or oxygen elements in a specific environment, as the XEOL spectra are independent of the excited beam-energy. The mechanism underlying these processes is certainly complicated and involves the electronic band structure of the semiconductor as a whole: the presence of defect complexes need to be considered, rather than just single point defects[28,29]. For example, it was recently proposed that calculations should take into account interaction between individual defects (including donor–donor and not only donor–acceptor interactions)[30]. It was predicted that in oxygen-deficient ZnO there is an attractive interaction between oxygen vacancy and zinc interstitial defects, which lowers their formation energy and can lead to their co-existence in defect complexes[30].

5.5.2 $Zn_{1-x}Mn_xO$

The presence of manganese in $Zn_{1-x}Mn_xO$ nanoparticles alters the XEOL spectra of the systems. Figure 7a shows the evolution of the photoluminescence for samples treated at 800ºC with increasing dopant content: the overall luminescence decreases with increasing manganese concentration. It is possible to notice this quenching effect,

driven by an increase of dopant content, at all processing temperatures (spectra not shown).

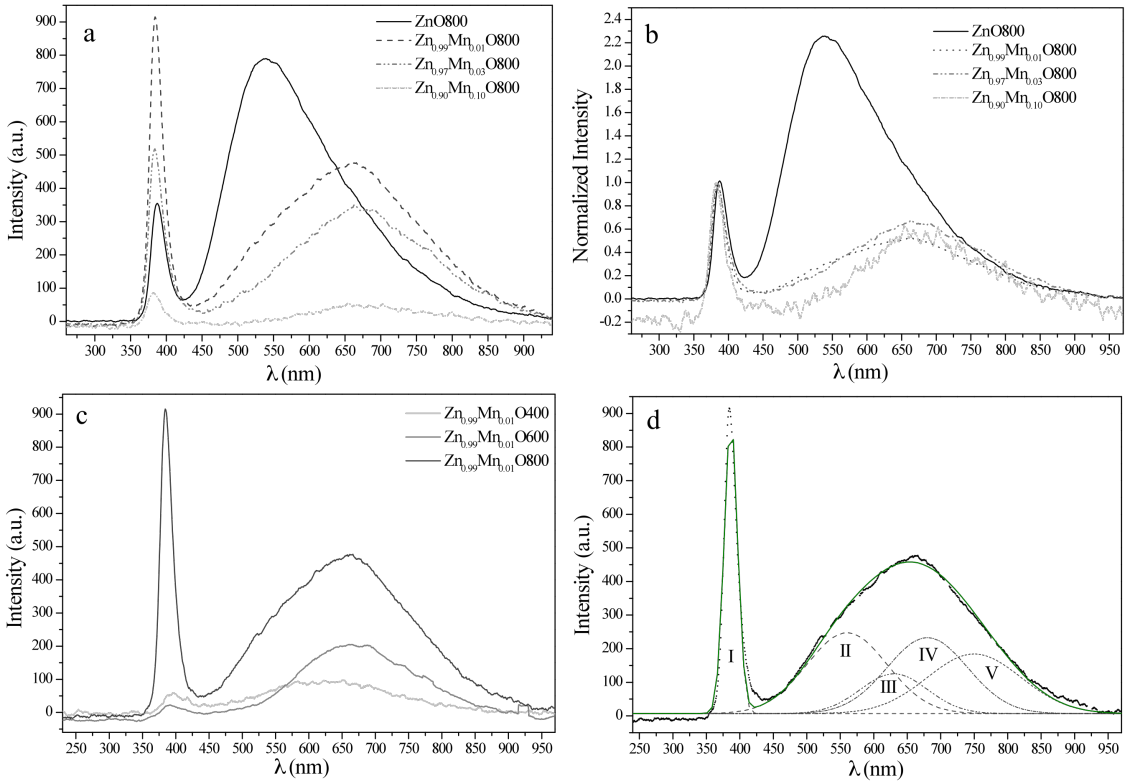

Figure 7: XEOL spectra of $Zn_{1-x}Mn_xO$: **a)** samples treated at 800°C, manganese concentration effects **b)** normalized spectra to the intensity of band-gap emission, manganese concentration effects **c)** $Zn_{0.99}Mn_{0.01}O$ samples, temperature effects **d)** peak fittings of $Zn_{0.99}Mn_{0.01}O$_800.

By normalising the XEOL spectra to the intensity of the band-gap emission (figure 7b) it is clear that there is a change in branching ratio between the defect emission and the band-gap emission upon doping. The addition of manganese increases the ratio of the band-gap emission relative to that of the defect emission.

For its part, the processing temperature affects the process yield (figure 7c shows the case of $Zn_{0.99}Mn_{0.01}O$ series): a rise in temperature leads to a gradual increase in the overall intensity of the XEOL spectrum. Furthermore, as seen in the undoped samples, the shape of the visible band is slightly affected by the processing temperature. Similar enhancement of the luminescence intensity of Mn-doped ZnO systems by annealing at 800ºC has been previously reported[31]. Annealing of ZnO and manganese doped nanoparticles enhances their luminescence due to the removal of vacancies and lattice defects inside the nanoparticles which trap electrons in defect levels and subsequently undergo non-radiative de-excitation.

The major difference between the manganese doped and undoped ZnO systems is the defect emission: the doped system contains defect levels lower in energy than those in

the ZnO. Figure 7d reports, as an example, the peak fitting of the $Zn_{0.99}Mn_{0.01}O$_800 sample; peak positions and their relative intensity are displayed in table 3.

Table 3: Peak fits for sample $Zn_{0.99}Mn_{0.01}O$_800.

	Peak Position (nm)	**%**
Peak I	~ 386	14
Peak II	~ 560	28
Peak III	~ 630	10
Peak IV	~ 680	28
Peak V	~ 750	20

The band-gap transition (peak I) is slightly blue shifted with the presence of manganese when compared with the undoped ZnO seen in the previous section. The manganese defect level at ~ 560 nm (2.2 eV), corresponds to the *d-d* transition from the $^4T_1$ to $^6A_1$ state of Mn^{2+}.[31] The defect level, peak IV, at ~ 680 nm (1.82 eV) most likely corresponds to surface defects on the $Zn_{1-x}Mn_xO$ nanoparticles, such as O vacancies near Mn sites which are lower in energy than the O vacancies near Zn sites, resulting in the red shift of the defect band compared to that of ZnO.

5.5.3 $Zn_{1-x}Co_xO$

The emission properties of the $Zn_{1-x}Co_xO$ series of compounds were investigated: the incorporation of Co^{2+} dopants into the ZnO host matrix results in a dramatic decrease in the ZnO defect emission (420-800 nm) and total quenching of the near band edge emission. Some of the related XEOL spectra are reported in figure 8.

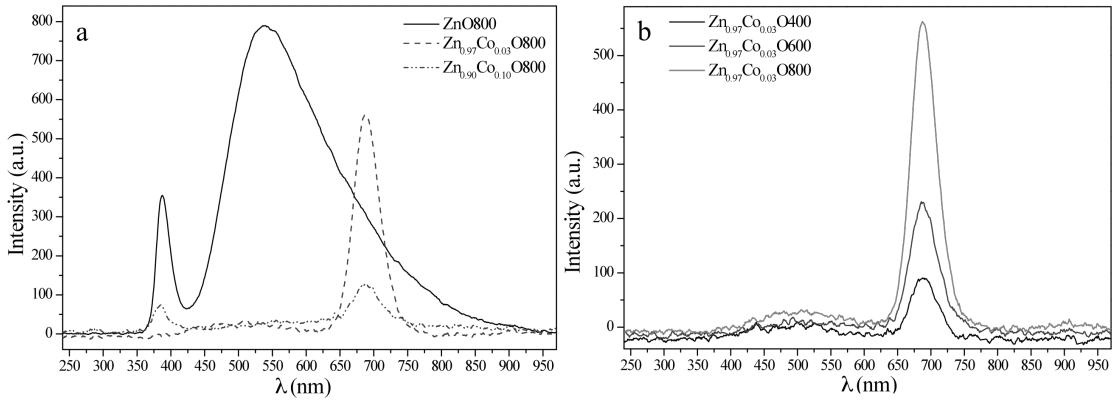

Figure 8: XEOL spectra of $Zn_{1-x}Co_xO$: **a)** samples treated at 800°C, cobalt concentration effects **b)** $Zn_{0.97}Co_{0.03}O$ samples, temperature effects.

All samples, independent of processing temperature and cobalt content, show an intense and narrow peak centred in the red zone of the visible spectrum. The observed

peak at ~687 nm is due to the transition from the $^2E \rightarrow {}^4A_2$ states of Co^{2+} in ZnO[32]. This clearly shows that the absorbed photon energy is transferred from the ZnO host to the cobalt which undergoes radiative recombination to produce the intense emission at ~687 nm.

The intensity of the dopant emission increases with increasing processing temperature, as shown in figure 8b (only $Zn_{0.97}Co_{0.03}O$ samples are reported), revealing that the energy transfer from the host to the dopant is improved by increasing the overall crystallinity of the system.

The concentration of cobalt also affected the emission properties (figure 8a): a rise in the dopant content leads to a gradual quenching of the peak at ~687 nm. In particular, as can be clearly seen in figure 8b, the XEOL spectrum of $Zn_{0.9}Co_{0.1}O$_800 shows a dramatic decrease of the cobalt emission and a re-appearance of the peak at ~390 nm, assigned to the exciton band emission of ZnO. The change in spectral feature intensities is due to the formation of Co_3O_4, as seen in the XRD and XANES data. The presence of this second phase drastically decreases the energy transfer between the zinc oxide matrix and the dopant.

Monitoring of the XEOL intensities can therefore be used to monitor the amount of secondary Co_3O_4 phase formation in ZnO:Co systems.

5.5.4 $Zn_{1-x}Cu_xO$

As described previously for the other systems the incorporation of copper in ZnO leads to drastic modification of the emission of the final material. As an example, XEOL spectra of $Zn_{1-x}Cu_xO$ treated at 800°C are reported in figure 9a.

In this case, unlike with manganese and cobalt, the presence of copper induces a nearly total quench of the luminescence. The effect is detectable even at the lowest concentration, $Zn_{0.99}Cu_{0.01}O$: an increase of the dopant concentration leads to an increase of the quenching (figure 9a). As described previously, the heat treatment influences the yield of the process: a rise in temperature induces an increase of the overall intensity of XEOL features (spectra are not shown).

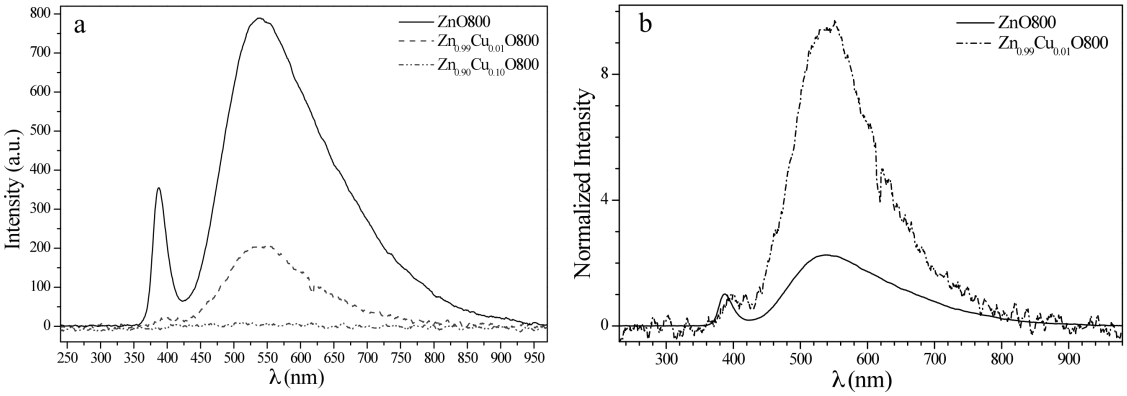

Figure 9: XEOL spectra of $Zn_{1-x}Cu_xO$: **a)** samples treated at 800°C **b)** normalised spectra in respect of the band gap emission.

Notwithstanding the emission's quench, it is possible to consider the effects that the copper induces on the system, looking at the XEOL spectra of samples with low dopant content. Sample $Zn_{0.99}Cu_{0.01}O$_800, figure 9a, show a broad emission band centred ~530 nm and a very low exciton band at ~400 nm.

One of the proposed explanations for green emission in ZnO:Cu doped system is the presence of copper impurities[33-35]. The transition responsible for the broad Cu green band in ZnO involves the $\Gamma_4(^2T_2)$ state of $Cu_{Zn}^{2+}(3d^9)$ and the excited (charge transfer) state in which the Cu centre has the configuration of a deep neutral acceptor (Cu^+,h).[35,36] It should be noted that while there is strong evidence that structured green emission is due to Cu impurities, evidence associating unstructured green emission with the presence of copper[37] is weaker.

To investigate the nature of this green emission figure 9b presents the normalised spectra, at the near band edge emission, of samples ZnO_800 and $Zn_{0.99}Cu_{0.01}O$_800. As determined with XANES, in sample $Zn_{0.99}Cu_{0.01}O$ treated at 800°C the copper is incorporated in the ZnO matrix as Cu_{Zn}^{2+}: the green emission is strongly enhanced due to the presence of the dopant as tetrahedrally substituted in zinc vacancies. There is also a slight shift of a few nm towards lower energy of the band-gap transition.

5.6 Summary and Conclusion

In this chapter, the luminescence properties of the $Zn_{1-x}TM_xO$ nanopowders were reported.

X-ray Excited Optical Luminescence (XEOL) is a suitable method to investigate phenomenological optoelectronic and structural correlations: results were discussed in terms of synthetic conditions (processing temperature, nature and content of dopant) as well as structural information.

Undoped ZnO exhibits expected XEOL features: a narrow band around 400 nm and a broad one in the visible region. The processing temperature significantly affects the emission spectrum, changing not only the relative intensity of the two signals but also the energy of the defects involved in the process. Upon increasing the processing temperature the oxide structure is modified and the optical properties are affected accordingly.

It must be emphasised that ZnO nanopowders synthesised via *Sol gel* show a tuneable visible band due to the presence of hydroxyl groups. Although further tests, such as time-resolved XEOL, are needed to better confirm this hypothesis, what is certain is the capability to obtain a material with different optical properties simply by changing the processing temperature used to anneal the samples.

$Zn_{1-x}Mn_xO$ nanoparticles prepared at various concentrations and temperatures were analysed: the addition of manganese increases the ratio of the band-gap emission relative to that of the defects emission. Furthermore, when the dopant is incorporated into the ZnO wurzite matrix as $Mn_{Zn}O$ (as in the series of compounds with x = 0.01 for all treatment temperatures) the visible band shows different components: new localised defects levels are introduced. When the second phase, $ZnMnO_3$, starts to segregate the overall emission is quenched.

The presence of cobalt in $Zn_{1-x}Co_xO$ leads to drastic modification of the emission spectra of doped zinc oxide. All samples, independent of processing temperature and cobalt content, show an intense and narrow peak centred in the red zone of the visible spectrum: the absorbed photon energy is transferred from the ZnO host to the cobalt which undergoes radiative recombination to produce the intense emission at ~687 nm (assigned to the transition between $^2E \rightarrow {}^4A_2$ states of Co^{2+}). The intensity of the dopant emission increases with increasing processing temperature, revealing that the energy

transfer from the host to the cobalt is improved by increasing the overall crystallinity of the system. It is possible to follow the formation of the second phase of Co_3O_4, detected only in samples with the higher level of dopant (x = 0.10), by monitoring the quenching of this signal.

Finally, unlike in the case of manganese and cobalt, XEOL spectra of $Zn_{1-x}Cu_xO$ nanoparticles show a near total quenching of the luminescence. The presence of copper, as in the previous cases, introduces new localised defect levels in the band gap of ZnO, as detected in samples with the lowest dopant content (x = 0.01) where the quenching effect is reduced.

A general trend regarding optoelectronic and structural correlations could be extrapolated from the results obtained with *X-ray Excited Optical Luminescence*.

Annealing of ZnO and $Zn_{1-x}TM_xO$ nanoparticles enhances their luminescence due to the removal of vacancies and lattice defects inside the nanoparticles which trap electrons in defect levels and subsequently undergo non-radiative de-excitation.

Second phase formation should be avoided to preserve the luminescent properties of $Zn_{1-x}TM_xO$ nanoparticles: independent of the dopant, segregation is always accompanied with a quenching in the emission spectra.

The nature of the transition metal ion could also affect the luminescence of ZnO synthesised by *Sol gel*. New localized defect levels are introduced in the band-gap of the semiconductor: the energy and nature of these levels can be tuned by changing the dopant. As in the case of manganese, these new levels could participate in the emission process, showing new components in the visible band of the spectra. The absorbed energy could be completely transferred from the ZnO host to one of these levels that decay radiatively, as seen with cobalt. Finally, it is possible to trap electrons in these defect levels that subsequently undergo non-radiative de-excitation, as reported for copper.

References:

PART 1

[1] J.E. Jaffe, J.A. Snyder, Z. Lin, A.C. Hess, *Phys. Rev. B* **62** (2000) 1660

[2] J.R. Chelikowsky, *Solid State Commun.* **22** (1977) 351

[3] U. Rossler, *Phys. Rev.***184** (1969) 733

[4] D. Vogel, P. Krüger, J. Pollmann, *Phys. Rev. B* **52** (1995) R14316

[5] B.K. Meyer, H. Alves, D.M. Hofmann, W. Kriegseis, D. Forster, F. Bertram, J. Christen, A. Hoffmann, M. Straßburg, M. Dworzak, U. Haboeck, A.V. Rodina, *Phys. Stat. Sol. B* **241** (2004) 231

[6] C.J. Ballhausen, *Introduction to ligand field theory*, *Mac* Graw-Hill Book Company, INC., New York, San Francisco, Toronto, London (1962)

[7] P.Koidl, *Phys. Rev. B* **15** (1977) 2493

[8] J.K. Furdyna, *J. Appl. Phys.* **64** (1988) R29

PART 2

[1] D.W. Bahnemann, C. Kormann, M.R. Hoffmann, *J. Phys. Chem.* **91** (1987) 3789

[2] A.B. Djurisˇic', Y.H. Leung, *Small* **2** (8–9) (2006) 944

[3] A.B. Djurisˇic', A.M.C. Ng, X.Y. Chen, *Progress in Quantum Electronics* **34** (2010) 491

[4] T. Hirai, Y. Harada, S. Hashimoto, K. Edamatsu, T. Itho, *J. Lumin.* **94-95** (2001) 261

[5] L. Armelao, F. Heigl, A. Jurgensen, R.I.R. Blyth, T. Regier, X.T. Zhou, T.K. Sham, *J. Phys. Chem. C* **111** (2007) 10194

[6] X.H. Sun, S. Lam, T.K. Sham, F. Heigl, A. Jurgensen, N.B. Wong, *J. Phys. Chem. B* **109** (2005) 3120

[7] T.K. Sham, D. Jiang, I. Coulthard, J.W. Lorimer, H.X. Feng, K.H. Tan, S.P. Frigo, R.A. Rosenberg, D.C. Houghton, B. Bryskiewicz, B. *Nature* **363** (1993) 331

[8] M. Anpo, Y.J. Kubokawa, *J. Phys. Chem.* **88** (1984) 5556

[9] M. Ghosh, A.K. Raychaudhuri, *Nanotechnology* **19** (2008) 445704

[10] T. Voss, C. Bekeny, L. Wischmeier, H. Gafsi, S. Borner, W. Schade, A.C. Mofor, A. Bakin, A. Waag , *Appl. Phys. Lett.* **89** (18) (2006) 182107

[11] A. Van Dijken, E.A. Meulenkamp, D. Vanmaeklenbergh, A. Meijerink, *J. Lumin.* **90** (2000) 123

[12] F. Oba, A. Togo, I. Tanaka, J. Paier, G. Kresse, *Phys. Rev. B* **77** (24) (2008) 245202

[13] S.A.M. Lima, F.A. Sigoli, M. Jafelicci Jr., M.R. Davolos, *Int. J. Inorg. Mater.* **3** (7) (2001) 749

[14] N.H. Nickel, E. Terukov, *Zinc Oxide — A Material for Micro- and Optoelectronic Applications*, Springer, Dodrecht, The Netherlands (2005) pp 69

[15] J. Hu, B.C. Pan, *J. Chem. Phys.* **129** (15) (2008) 154706

[16] K. Vanheusden, C.H. Seager, W.L. Warren, D.R. Tallant, J.A. Voigt, *Appl. Phys. Lett.* **68** (3) (1996) 403

[17] N.Y. Garces, L. Wang, L. Bai, N.C. Giles, L.E. Halliburton, G. Cantwell, *Appl. Phys. Lett.* **81** (4) (2002) 622

[18] A.B. Djurisˇic´, W.C.H. Choy, V.A.L. Roy, Y.H. Leung, C.Y. Kwong, K.W. Cheah, T.K. Gundu Rao, W.K. Chan, H.F. Lui, C. Surya, *Adv. Funct. Mater.* **14** (9) (2004) 856

[19] D. Li, Y.H. Leung, A.B. Djurisˇic´, Z.T. Liu, M.H. Xie, S.L. Shi, S.J. Xu, W.K. Chan, *Appl. Phys. Lett.* **85** (9) (2004) 1601

[20] A. Rogalev, J. Goulon, *Chemical Applications of Synchrotron Radiation*, *Part II*: *X-ray Applications*; T.K. Sham Ed.; World Scientific: River Edge, NJ (2002); Vol. 12B, pp 707

[21] D.T. Jiang, I. Coulthard, T.K. Sham, J.W. Lorimer, S.P. Frigo, X.H. Feng, R.A. Rosenberg, *J. Appl. Phys.* **74** (1993) 6335

[22] I. Coulthard, T.K. Sham, *Solid State Commun.* **110** (1999) 203

[23] M.A. Reshchikov, J.Q. Xie, B. Hertog, A. Osinsky, *J. Appl. Phys.* **103** (10) (2008) 103514

[24] X. Liu, X. Wu, H. Cao, R.P.H. Chang, *J. Appl. Phys.* **95** (6) (2004) 3141

[25] J. Qiu, X. Li, W. He, S.J. Park, H.K. Kim, Y.H. Hwang, J.H. Lee, Y.D. Kim, *Nanotechnology* **20** (15) (2009) 155603

[26] K.H. Tam, C.K. Cheung, Y.H. Leung, A.B. Djurisˇic´, C.C. Ling, C.D. Beling, S. Fung, W.M. Kwok, W.K. Chan, D.L. Phillips, L. Ding, W.K. Ge, *J. Phys. Chem. B* **110** (42) (2006) 20865

[27] R.B.M. Cross, M.M. De Souza, E. Sankara Narayanan, *Nanotechnology* **16** (10) (2005) 2188

[28] B. Lin, Z. Fu, Y. Jia, *Appl. Phys. Lett.* **79** (7) (2001) 943

[29] P.S. Xu, Y.M. Sun, C.S. Shi, F.Q. Xu, H.B. Pan, *Nucl. Instrum. Methods Phys. Res., Sect. B* **199** (2003) 286

[30] Y.S. Kim, C.H. Park, *Phys. Rev. Lett.* **102** (8) (2009) 086403

[31] C. Ronning, P.X. Gao, Y. Ding, Z.L. Wang, D. Schwen, *Appl. Phys. Lett.* **84** (2004) 783

[32] P. Koidl, *Phys. Rev. B* **15** (1977) 2493

[33] N.Y. Garces, L. Wang, L. Bai, N.C. Giles, L.E. Halliburton, G. Cantwell, *Appl. Phys. Lett.* **81** (4) (2002) 622

[34] P. Dahan, V. Fleurov, *Phys. Rev. B* **57** (1998) 9690

[35] D.J. Robbins, D.C. Herbert, P.J. Dean, *J. Phys. C: Solid State Phys.* **14** (1981) 2859

[36] R. Dingle *Phys. Rev. Lett.* **23 (**1969) 579

[37] N.Y. Garces, L. Wang, L. Bai, N.C. Giles, L.E. Halliburton, G. Cantwell, *Appl. Phys. Lett.* **81** (4) (2002) 622

Chapter 6

Magnetic Properties of $Zn_{1-x}TM_xO$ (TM=Mn, Co, Cu)

Spin-dependent phenomena in wide band-gap semiconductors, such as ZnO, may lead to the development of devices with new or enhanced functionality: sensitive biological and chemical sensors, polarised solid-state light sources (spin light-emitting diodes) or novel microprocessors, to name but a few.

In order to become a practical technology, semiconductor spintronics demands the discovery and application of ferromagnetic semiconductors that exhibit spin polarisation in the majority carrier band at and above room temperature. Moreover, intrinsic remanent magnetisation would allow spin-polarised currents to propagate in such materials without the need for a continuous magnetic field.

Recent theoretical calculations[1-3] have predicted that transition metal ion doped ZnO is one of the most promising candidates for room-temperature ferromagnetism. Additionally, owing to its outstanding optical transparency, doped ZnO allows the study of magneto-optical properties, which could lead to the development of magneto-optoelectronic devices[4,5].

Preliminary results will be presented on the magnetic properties of $Zn_{1-x}TM_xO$ (TM = Mn, Co, Cu). In particular, developing an understanding of the real nature of the magnetic interactions in such systems, of which there has been considerable debate in the scientific community, is very valuable.

6.1 Introduction

6.1.1 Diluted Magnetic Semiconductor

Currently the development of *Dilute Magnetic Semiconductor* materials (DMS) exhibiting ferromagnetic behaviour for different applications (i.e. spin-based light-emitting diodes, sensors or transistors) has aroused significant interest in the scientific community[1-8].

These materials are formed through the introduction of transition metal (TM) ions or rare earth ions into the host semiconductors. These ions have partially filled *d* and *f* shells, respectively, which give rise to unpaired electrons. The magnetic behaviour of such materials depends upon the concentration of the TM ions in the crystal, the carrier density and the crystal quality.

The term DMS is used to indicate that a fraction of the atoms in a non-magnetic semiconductor host, like ZnO, are substituted by magnetic ions. As a consequence, the electronic structure of the substituted *3d* transition-metal impurities in the semiconductors is influenced by two competing factors: strong 3d-host hybridisation and strong coulomb interactions between *3d-3d* electrons. There are two interacting subsystems in DMS materials, the delocalised conduction band electrons and valence band holes and the random, diluted system of localised magnetic moments associated with the magnetic atoms.

Recent interest in DMSs took off after some theoretical calculations predicted that the T_C for p-type DMSs could exceed room temperature[1-3]. In particular, stable ferromagnetism (FM) in DMSs based on wide band-gap semiconductors, i.e., ZnO, should exist. Using first principle calculations, it was theoretically demonstrated[9] that a ZnO host doped with TM atoms (such as V, Cr, Fe, Co and Ni) exhibited FM ordering, whereas doping with Ti and Cu resulted in a paramagnetic state.

These theoretical predictions started an experimental race which soon revealed that some TM doped ZnO systems exhibited room temperature ferromagnetism although the exact origin and mechanism of the FM ordering is still disputed. In some cases the results concerning the existence of ferromagnetism have been somewhat controversial, partly due to the sensitivity of the resulting magnetic properties to the exact growth conditions and also to incomplete characterisation of the magnetic properties.

A sufficiently detailed overview of experimental results in these systems, which is certainly not exhaustive, can be found in the listed literature: Co doped ZnO[10-23], Mn doped ZnO[24-30] and Cu doped ZnO[31-41].

A key issue in many of the published reports is whether the resulting material is indeed an alloy of transition metal elements within the host material or whether it remains as the matrix material with clusters, precipitates or second phases that are responsible for the observed magnetic properties. A relatively complete characterisation of the DMS would involve a complete magnetic characterisation (hysteresis measurements as well as field-cooled and zero field-cooled magnetisation, magneto-transport) as well as a detailed structural description with, for example, *High Resolution Transmission Electron Microscopy* (HRTEM), chemical bonding information obtained from *X-Ray Photoelectron Spectroscopy* (XPS) and lattice location measurements by *Extended X-ray Absorption Fine Structure* (EXAFS). In most cases, such a detailed characterisation is not carried out. For that reason, the origin of the observed magnetic behaviour still remains controversial, i.e., whether they are intrinsic or extrinsic properties of the material.

6.1.2 *Superconducting Quantum Interference Device* (SQUID)

The *Superconducting Quantum Interference Device* (SQUID) *Magnetometer-Susceptometer* (MS) is one of the most sensitive instruments for measuring magnetic moments of small samples. SQUID magnetometers are able to measure changes in the magnetic moment of the sample with sensitivities down to 10^{-11} Am^2 (10^{-8} emu), in a wide range of applied magnetic field and sample temperature.

SQUID-MS instruments are induction-based systems where the sample is moved along the direction of the applied field through a set of pick up loops, called a gradiometer. The variable magnetic flux inside the coils caused by the moving sample induces a current in the gradiometer, according to Faraday's Law of induction. The gradiometer is inductively coupled to a SQUID, which converts the magnetic flux to a voltage signal with high gain and low noise. The SQUID is made of a superconducting loop interrupted by thin tunnel barriers (Josephson junctions) and its functionality relies on the Josephson effect. The signal measured on the SQUID is fitted to a model function in order to calculate the magnetic moment of the sample. A complete overview of these techniques can be found, for example, in *The Squid Handbook*[42].

The instrument used here is a MPMS-7 system manufactured by Quantum Design. A schematic cross section of the instrument is provided in figure 1.

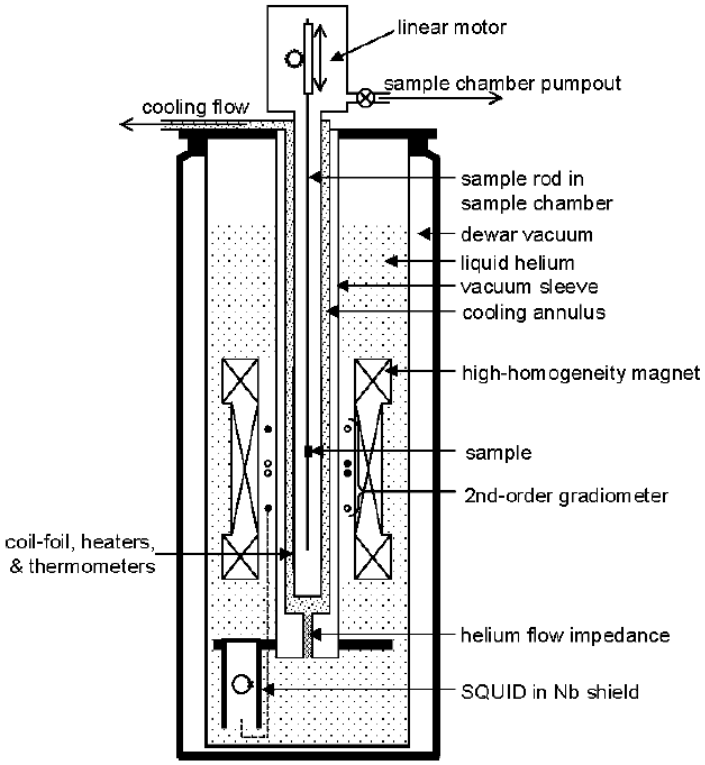

Figure 1: Schematic cross section of the SQUID, Quantum Design manufacturer.

The instrument allows measurement of magnetic moments in a magnetic field up to $B = \pm 7$ Tesla, in a temperature range of 2 K to 400 K. The instrument sensitivity depends on the magnetic field which is typically ranged from $\pm 1x10^{-7}$ emu @ 1 Tesla to $\pm 1x10^{-6}$ emu @ 7 Tesla (absolute sensitivity).

The SQUID, the superconducting gradiometer and magnet only operate at cryogenic temperatures; therefore these parts of the instrument are kept in thermal equilibrium with a bath of liquid helium (4.22 K). The helium Dewar is thermally insulated by a vacuum sleeve and surrounded by a liquid nitrogen Dewar (not shown in figure). The sample chamber is centred inside the magnet and is separated from the liquid helium bath by the vacuum sleeve. The chamber has thermometers for temperature control and can be heated by heaters in the chamber wall or cooled by a flow of cold helium through a gap between the chamber and the vacuum sleeve (cooling annulus). The sample is attached to a rod and located in the middle of the magnet; a linear motor drives the oscillation of the sample inside the gradiometer.

The MPMS-7 makes use of a second order gradiometer, formed by three sets of coils equally spaced and connected in series; the first and last coil have the same

number of loops and are wound in the same direction, while the middle coil is wound in the opposite direction and has twice the number of loops (figure 2).

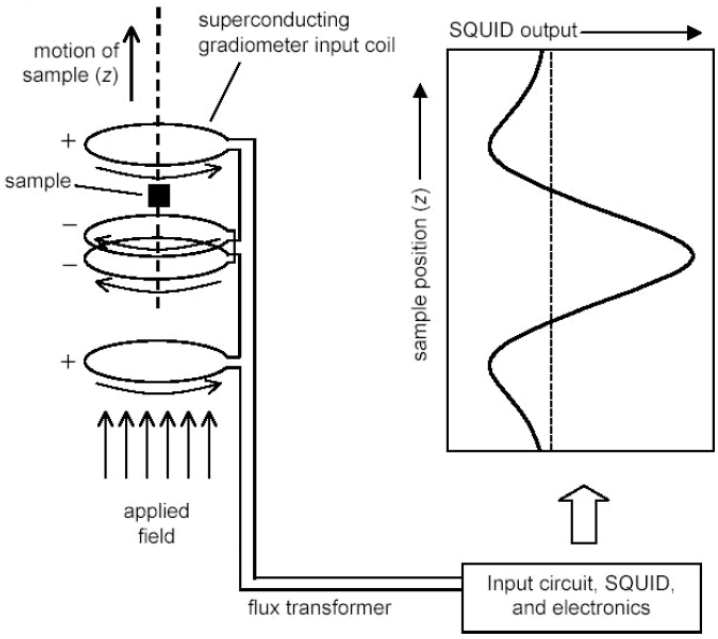

Figure 2: Scheme of the MPMS7 gradiometer.

This arrangement of coils ideally allows complete cancellation of background signals from the sample holder and strongly reduces the effect of field noise in the magnet. The response curve of the SQUID for a magnetic point dipole moving in the centre of the gradiometer can be obtained from the Biot-Savart law. The following equation is used to fit the signal:

$$F(z) = A + Bz + C[g(r,z - D - b) - 2g(r,z - D) + g(r,z - D + b)]$$

where *A, B, C,* and *D* are fitting parameters, *r* is the gradiometer coil radius (0.97 cm), *b* is the inter-coil distance (1.519 cm) and the response function from each coil at an axial offset z' is given by

$$g(r,z') = 1/(r^2 + z'^2)^{3/2}$$

Following calibration with a reference sample of known susceptibility (generally palladium), the magnetic moment of the sample can be calculated from the value of *C*; *A* is a signal offset correction, while *B* corrects any linear drift of the SQUID signal with time and *D* is a sample offset correction.

There are two operating modes for magnetic property measurements in constant magnetic fields; the standard one is called *DC* measurement, where the sample is moved through the coils in discrete steps, while the alternative is called *Reciprocating Sample Option* (*RSO*), where the sample is oscillated over a few centimetres by a servo motor

several times per second (1Hz to 4Hz), and the signal is averaged over several scans. The latter scheme achieves better sensitivity by eliminating low frequency noise and has therefore been used in these experiments.

6.1.3 Experimental

The MPMS-7 is used for measuring $Zn_{1-x}TM_xO$ samples. Sample preparation and mounting varied between powder samples, single crystals and thin films. In the case of powders, the sample is first gently ground in a glass mortar and then a small quantity (about 20 mg) is loaded inside a gelatine capsule. The powder is packed inside the capsule with some cotton wool to avoid displacement and reduce reorientation during the measurement. Finally the capsule is loaded inside a clear plastic drinking straw, of 5 mm diameter, and held in place by transverse stripes cut from the straw and folded inward.

Two different types of experiment are set up to follow the evolution of the magnetisation, scanning the measurement temperature and the applied magnetic field.

6.2 Magnetic Properties of Solids

Magnetism is a property of materials that respond at an atomic or subatomic level to an applied magnetic field. Some are attracted to a magnetic field (paramagnetism); others are repelled by a magnetic field (diamagnetism); others have a much more complex relationship with an applied magnetic field. Some of the magnetic states are shown in figure 3 and described below.

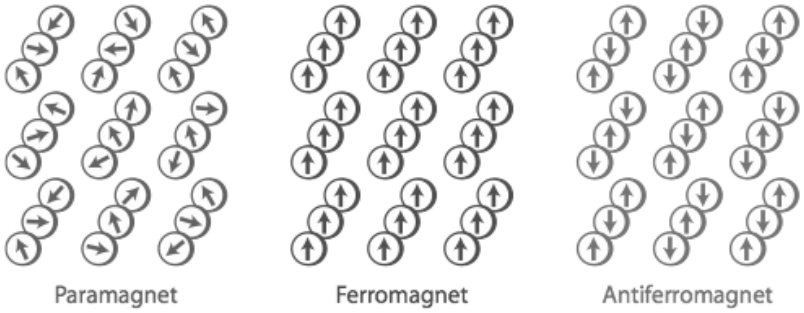

Figure 3: The alignment of magnetic moments for some of the principal classes of magnetism. Random alignment of adjacent magnetic moments is observed for paramagnets. Ferromagnets exhibit parallel alignment of adjacent magnetic moments. Simple antiferromagnets exhibit antiparallel alignment of adjacent magnetic moments.

The magnetic moment of a free atom can be associated with three principal effects: the spin of the electrons, their orbital motion and the spin-orbit coupling.

It is possible to define the magnetisation *M* as the magnetic moment per unit volume. The magnetic susceptibility (χ) per unit volume is defined[43-45] as

$$\chi = \mu_0 M / B$$

where *B* is the macroscopic magnetic field intensity, expressed in SI units (in the CGS system $\chi = M/B$). In both systems of units the susceptibility is dimensionless. Quite frequently χ is defined for a mole of the substance: the molar susceptibility is written as χ_M. Substances with negative susceptibility are called diamagnetic; a positive magnetic χ is characteristic of paramagnetic materials. Ordered arrays of magnetic moments could give rise to ferro- or ferrimagnetism and antiferromagnetism.

Below a short description of the principal types of magnetic material is reported; further information can be found in various texts[43-45].

6.2.1 Paramagnetism

In a paramagnetic material there are unpaired electrons, i.e. partially filled atomic or molecular orbitals. While paired electrons are required by the Pauli exclusion principle to have their intrinsic ('spin') magnetic moments pointing in opposite directions, causing their magnetic moments to cancel out, an unpaired electron is free to align its magnetic moment in any direction. When an external magnetic field is applied, these magnetic moments will tend to align themselves in the same direction as the applied field, thus reinforcing it.

The *Brillouin Function* describes the magnetisation of an ideal paramagnet as a function of the dimensionless ratio $g\mu_B B/k_B T$. In practice this function describes the spin state of a paramagnet as the applied magnetic field is varied at a constant temperature.

The magnetisation is given by

$$M = Ng\mu_B S \cdot \mathrm{B}_s(x)$$

where N is the number of atoms, *g* is the Landé factor, μ_B is the Bohr magneton defined as $e\hbar/2m_N c$ (CGS system); the Brillouin function $B_S(x)$ is defined as

$$B_s(x) = \frac{1}{S}\left[\frac{2S+1}{2}\coth\left(\frac{2S+1}{2}x\right) - \frac{1}{2}\coth\left(\frac{x}{2}\right)\right]$$

$$x \equiv \frac{g\mu_B}{\kappa_B}\frac{B}{T}$$

For x << 1, i.e. when $\mu_B B / k_B T$ is small, the expression of the magnetisation can be approximated by

$$\frac{M}{B} \cong \frac{NS(S+1)g^2\mu_B^2}{3k_BT} = \frac{Np^2\mu_B^2}{3k_BT} = \frac{C}{T}$$

here p is the effective number of Borh magnetons, defined as

$$p \equiv g\left[S(S+1)\right]^{1/2}$$

The high temperature limit is known as the *Curie Law* and the constant C is known as the *Curie constant*.

6.2.2 Ferromagnetism

Ferromagnetic materials exhibit a long-range ordering phenomenon at the atomic level that causes the unpaired electron spins to line up parallel with each other in a region called a domain. On the other hand, in materials that exhibit antiferromagnetism, spins align in a regular pattern with neighbouring spins (on different sub-lattices) pointing in opposite directions.

The largest internal interaction leading to the parallel (or antiparallel) alignment of the magnetic moments to one another is generally the exchange interaction. In *Heisenberg model*, the total energy of the interactions between spins $\{S_i\}$ is

$$E = -2\sum_{i \neq j} J_{i,j} S_i S_j$$

where J is the exchange integral, related to the overlap of the charge distributions of atoms i,j. If $J_{ij} > 0$ the interaction is called ferromagnetic, if $J_{ij} < 0$ the interaction is called antiferromagnetic; finally if $J_{ij} = 0$ the spins are non-interacting.

The orienting effect of the exchange interaction is opposed by thermal agitation, and at elevated temperatures the spin order is destroyed. The *Curie temperature,* T_C, is defined as the temperature above which the spontaneous magnetisation vanishes; it separates the disordered paramagnetic phase at $T > T_C$ from the ordered ferromagnetic state at $T < T_C$.

A modification of the Curie law, known as the *Curie-Weiss law*, describes this deviation observed in interacting systems:

$$\chi = \frac{C}{T - \Theta}$$

where the *Weiss constant* (Θ) is proportional to the strength of the magnetic interactions observed. Positive Weiss constants indicate ferromagnetic interactions, while negative Weiss constants indicate antiferromagnetic interactions.

When a ferromagnetic material is magnetised in one direction, it will not relax back to zero magnetisation when the imposed magnetising field is removed. It must be driven back to zero by a field in the opposite direction. If an alternating magnetic field is applied to the material, its magnetisation will trace out a loop called a hysteresis loop. The lack of retraceability of the magnetisation curve is the property called hysteresis and it is related to the existence of magnetic domains in the material. Once the magnetic domains are reoriented, it takes energy to turn them back again. This property of ferromagnetic materials is useful as a magnetic "memory".

A number of primary magnetic properties of a material can be determined from a hysteresis loop as shown in figure 4.

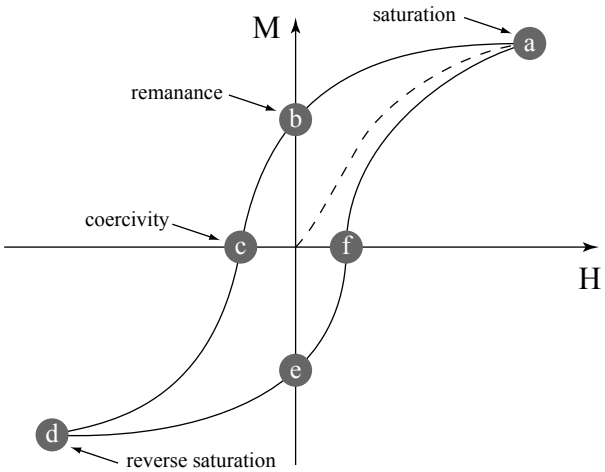

Figure 4: M vs. H curve: hysteresis loop.

The *Saturation* magnetisation (M_S) is the point at which all the magnetic domains are aligned (denoted as “a”, figure 4). *Remanence* (M_R), instead, is defined as the material's ability to retain a certain amount of residual magnetic moment when the magnetising force is removed after achieving saturation (denoted as “b”, figure 4). Finally, *Coercive Field* (H_C) is the amount of reverse magnetic field which must be applied to a magnetic material to return the magnetic flux to zero (point “c”, figure 4).

6.3 Results: $Zn_{1-x}TM_xO$ (TM = Mn, Co, Cu)

The magnetic properties of $Zn_{1-x}TM_xO$ nanoparticles synthesised by *Sol gel* will be presented in this section. This is only a preliminary study and further characterisation will be needed to have a complete overview of the systems.

Taking into account that the magnetisation of TM-doped ZnO is strongly dependent on the preparation parameters and any trace amount of external contamination could lead to a misinterpretation of experimental results, only samples with low dopant content, $Zn_{0.99}TM_{0.01}O$, treated at different temperatures, are examined.

Indeed, extended characterisation, reported in the previous chapters, have revealed that only at very low dopant concentration second phase segregation is prevented and transition metal ions are dispersed uniformly in the ZnO matrix.

Below, preliminary results will be subdivided into sections for each transition metal ion; samples containing cobalt will be also discussed in terms of annealing temperature. Regarding manganese doping, only $Zn_{0.99}Mn_{0.01}O$_400 will be presented.

Finally, among samples doped with copper, $Zn_{0.99}Cu_{0.01}O$_800 has been chosen. This is because previous characterisations, and in particular XAS, have revealed that only high annealing temperature provides the inclusion of the dopant inside the ZnO host.

6.3.1 $Zn_{0.99}Co_{0.01}O$

First of all, data for $Zn_{0.99}Co_{0.01}O$_400 will be presented, in particular the field dependence of the magnetisation measured at different temperatures from 5 K up to room temperature.

Figure 5 shows the evolution of magnetisation (M) as a function of the applied field (H) at T = 5 K. The solid curve in figure 5 is a fit of the data to a parameterised Brillouin function assuming that cobalt is incorporated as Co^{2+} and that for this species, S = 3/2 and g = 2.26 for. The g factor is taken from EPR studies reported in the literature[46,47] for cobalt ions dispersed in ZnO, Co^{2+}_{Zn}.

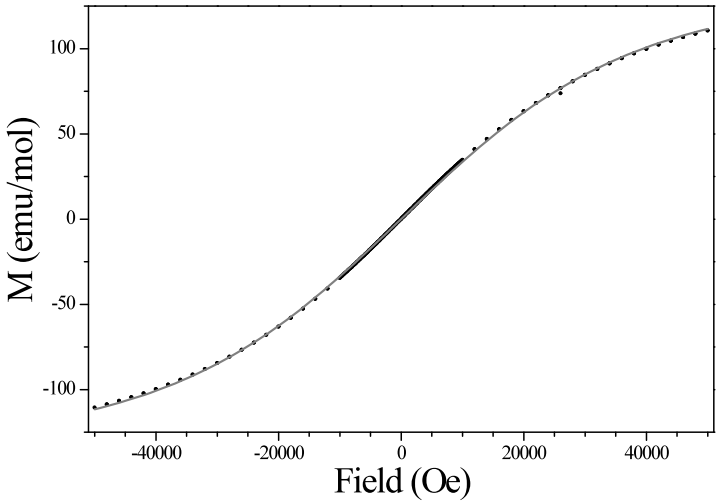

Figure 5: Plot of M vs. H at T = 5 K for $Zn_{0.99}Co_{0.01}O$_400. Data are fitted with a Brillouin function.

$Zn_{0.99}Co_{0.01}O$_400 at T = 5 K displays paramagnetic behaviour and the Brillouin fitting gives rise to a cobalt concentration that contributes about 70% of the nominal content to this magnetic phase. The M vs. H curve shows, however, a small hysteresis contribution with a coercive field (Hc) of about 30 Oe, indicating the presence of a small ferromagnetic phase volume. This contribution is so small that it is not possible to quantitatively discriminate it from the predominant paramagnetic behaviour.

Increasing the operating temperature up to 300 K, the observed M vs. H behaviour in the sample reveals that it is composed of a mixture of ferromagnetic and paramagnetic phases. Figure 6a reports the field scan of $Zn_{0.99}Co_{0.01}O$_400 taken at T = 300 K, as an example.

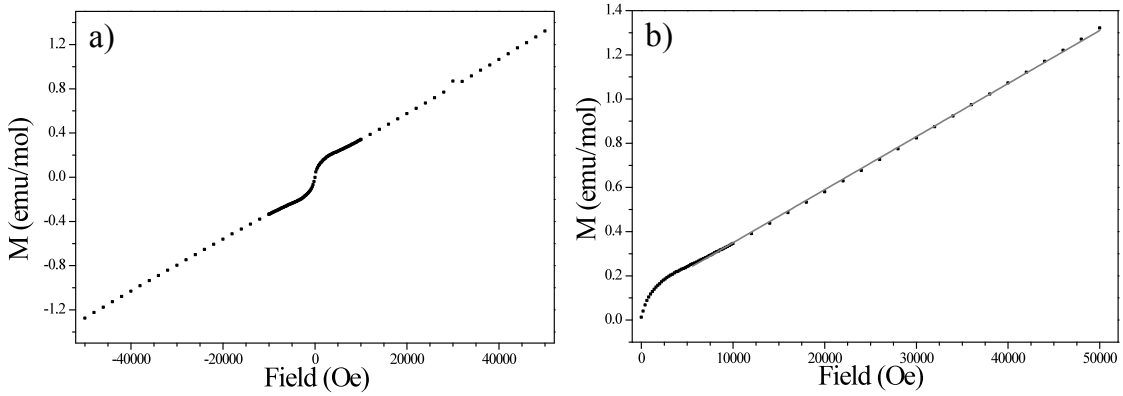

Figure 6: Plot of M vs. H at T = 300 K for $Zn_{0.99}Co_{0.01}O$_400 **a)** complete scan **b)** fitting of experimental data using the equation reported in the text below.

Experimental data are fitted taking into account the presence of these two contributions:

$$M = Ng\mu_B S \cdot B(x) + \gamma \cdot \vartheta(x)$$

$$\vartheta(x) = \begin{cases} 1 & x > 0 \\ -1 & x < 0 \end{cases}$$

where the first term is the Brillouin function while the second addend $\gamma\vartheta(x)$ is a jump used for taking into account the ferromagnetic contribution. This type of fitting gives rise to the presence of a paramagnetic contribution of about 29% of the nominal cobalt content and γ = 0.18 emu/mol. The coercive field (Hc) is about 20 Oe.

Table 1: Fitting parameters of data taken at different temperature regarding $Zn_{0.99}Co_{0.01}O$_400.

T (K)	%para	γ (emu/mol)	H_C (Oe)
5	69.5±0.5	-	30±2
20	79.5±0.5	-	40±2
50	85.5±0.5	-	50±2
100	69.0±0.5	0.02±0.01	35±2
150	60.0±0.5	0.04±0.01	30±2
200	59.0±0.5	0.06±0.01	30±2
250	17±0.5	0.22±0.01	30±2
300	29.0±0.5	0.18±0.01	20±2

All fitting parameters obtained with changing operating temperature are listed in table 1; figure 7 plots the variation of the paramagnetic and ferromagnetic contributions in $Zn_{0.99}Co_{0.01}O$_400.

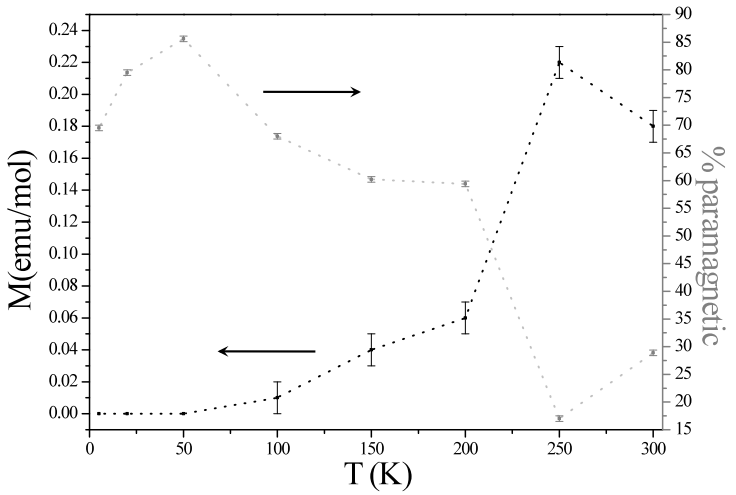

Figure 7: Graph which summarises the evolution of paramagnetic and ferromagnetic contributions as a function of the working temperature for sample $Zn_{0.99}Co_{0.01}O$_400.

The peculiarity in behaviour of this sample is the temperature dependence of the magnetic properties. Changing the measuring temperature results in a change in both the paramagnetic and ferromagnetic contributions: the fraction of the sample that shows paramagnetic behaviour is temperature dependent and the measured magnetization in the ferromagnetic state increases as the temperature is raised instead of decreasing. In addition, the paramagnetic and ferromagnetic contributions alone do not account for the nominal concentration of cobalt ions in the sample. Another interaction should be taken into account that contributes to the decrease in saturation magnetisation: an

antiferromagnetic contribution, which tends to align spins antiparallel, thus cancelling their contribution to the net magnetisation.

The coexistence of different contributions in such a system has been reported previously[48]. It seems that the cobalt ions are not simply divided into three different categories, exhibiting dissimilar magnetic interactions between spins but the domains are interacting with each other. One plausible explanation could be the presence of competing interactions between spins, where randomness in the sign of the exchange interaction gives rise to transitions between ordered and disordered magnetic phases[49-58]. By changing the temperature it is possible to favour the presence of different magnetic states due to entropic factors. These behaviours have been observed in concentrated spin systems, including diluted magnetic semiconductors such as $Eu_xSr_{1-x}S$[50-52], polycrystalline metals[49] or amorphous alloys[53-55]; other systems exhibiting such magnetic behaviour are metallic ferromagnets diluted with non-magnetic or weakly magnetic atoms[56-57]. These are systems where the randomness in the sign of the exchange interaction is brought about by random distribution of the spins. Figure 8 show, as an example, the magnetic phase diagrams for the diluted magnetic semiconductor $Eu_xSr_{1-x}S$[50] (figure 8a) and the amorphous alloy $(Fe_{1-x}Mn_x)_{75}P_{16}B_6Al_3$[58] (figure 8b), respectively. The breakdown in the ferromagnetism in these systems is an intrinsic property, based upon the competition between ferromagnetic and antiferromagnetic exchange interactions.

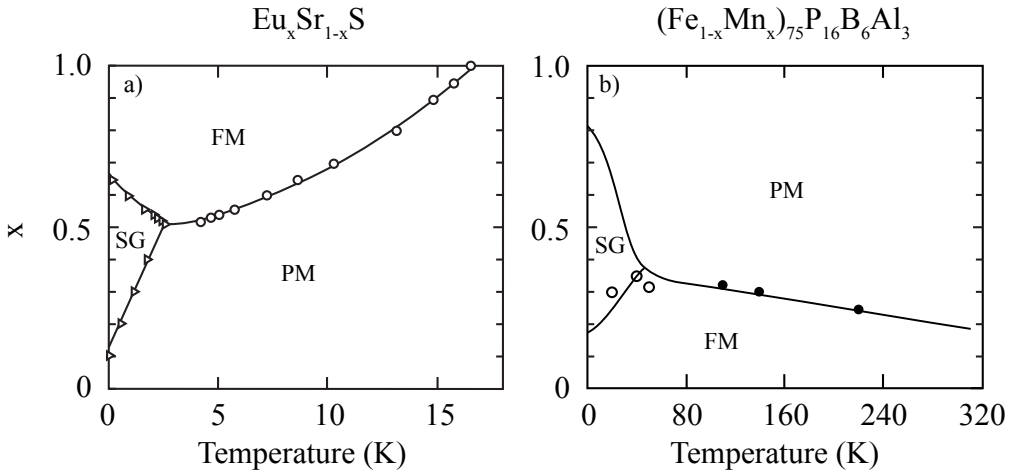

Figure 8: Magnetic phase diagram of **a)** $Eu_xSr_{1-x}S$[50] and **b)** $(Fe_{1-x}Mn_x)_{75}P_{16}B_6Al_3$[58].

To the best of our knowledge, this kind of competing interaction between spins for doped ZnO has never been reported before. Further characterisation should be

performed to confirm that this is the case for cobalt-doped nanoparticles, $Zn_{0.99}Co_{0.01}O$_400, synthesised by *Sol gel*.

The temperature dependence of the susceptibility, χ, has been studied, applying a range of fields from 1 T down to 500 Oe. Independent of the applied field, consistent behaviour is observed: the susceptibility of the samples decreases with increasing temperature. As an example, data taken at H = 1000 Oe are reported in figure 9.

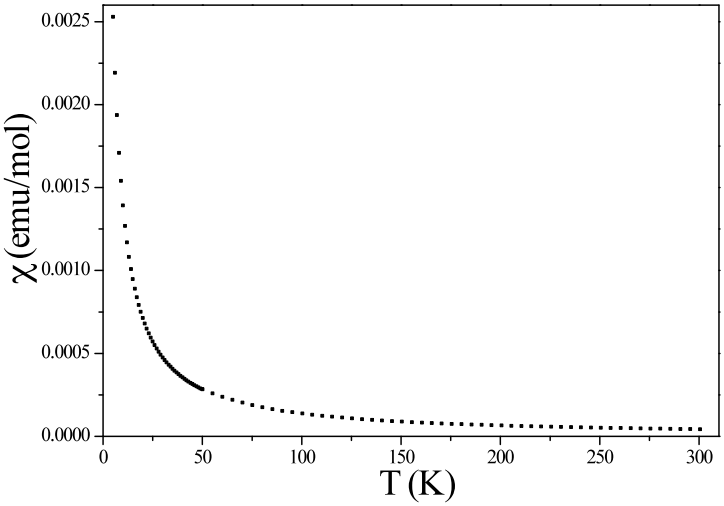

Figure 9: Plots of χ vs. T in $Zn_{0.99}Co_{0.01}O$_400 at H = 1000 Oe.

In all cases, even at low applied fields, the paramagnetic behaviour is predominant and no transition due to the ferromagnetic contribution is observed. In general, it can be difficult to determine the type of magnetic interactions occurring in a sample from the plot of susceptibility as a function of temperature.

Samples treated at higher temperature, $Zn_{0.99}Co_{0.01}O$_600 and $Zn_{0.99}Co_{0.01}O$_800, have also been characterised. As in the previous case, the field dependence of the magnetisation is measured at a range of temperatures from 5 K up to room temperature. In analogy with nanoparticles treated at low temperature, T = 400°C, similar behaviours are observed in both cases.

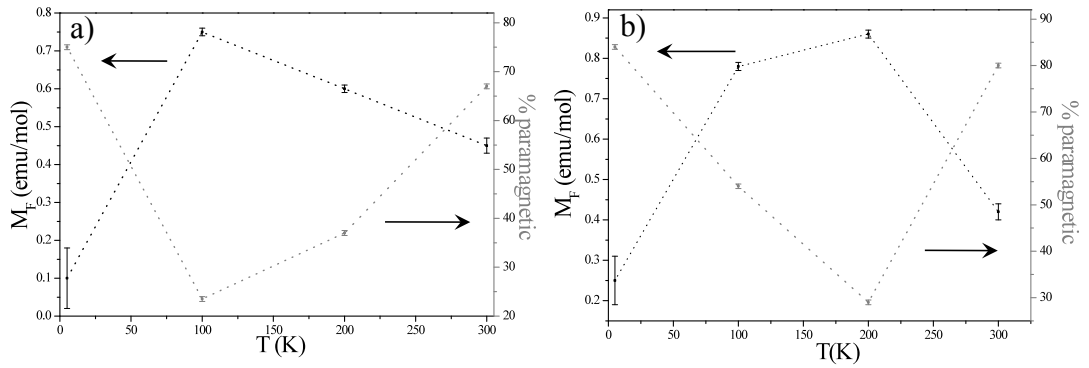

Figure 10: Graph which summarises the evolution of paramagnetic and ferromagnetic contributions as a function of the working temperature for sample **a)** $Zn_{0.99}Co_{0.01}O$_600 **b)** $Zn_{0.99}Co_{0.01}O$_800 .

All the fitting parameters for $Zn_{0.99}Co_{0.01}O$_600 and $Zn_{0.99}Co_{0.01}O$_800, obtained for varied temperatures are listed in table 2 and 3, respectively. The variation of the paramagnetic and ferromagnetic contributions in $Zn_{0.99}Co_{0.01}O$_600 and $Zn_{0.99}Co_{0.01}O$_800 are also plotted in figures 10a and 10b, respectively.

Table 2: Fitting parameters of data taken at different temperatures for $Zn_{0.99}Co_{0.01}O$_600.

T (K)	%para	γ (emu/mol)	H_C (Oe)
5	75.0±0.5	0.01±0.06	20±2
100	23.5±0.5	0.75±0.01	60±2
200	37.0±0.5	0.60±0.01	60±2
300	67.0±0.5	0.45±0.01	60±2

Table 3: Fitting parameters of data taken at different temperatures for $Zn_{0.99}Co_{0.01}O$_800.

T (K)	%para	γ (emu/mol)	H_C (Oe)
5	84.0±0.5	0.25±0.06	10±2
100	54.0±0.5	0.78±0.01	25±2
200	29.0±0.5	0.86±0.01	20±2
300	80.0±0.5	0.42±0.01	20±2

Like the first sample, the coexistence of different contributions is observed. The temperature dependence of the magnetic properties is maintained even in samples annealed at higher temperature: while increasing the measuring temperature, in fact, both the paramagnetic and ferromagnetic contributions change. Comparing figure 7, 10a and 10b it is possible to make some observations about the influence of synthesis condition. Samples with different annealing temperatures possess different proportions of ferromagnetic phase. In particular, the value of saturation magnetisation related to the ferromagnetic state increases in samples treated at higher temperature. Furthermore, looking at the bumps reported in figures 7 and 10, the inflection point appears to be at different temperatures.

The temperature dependence of the susceptibility, χ, of $Zn_{0.99}Co_{0.01}O$_600 and $Zn_{0.99}Co_{0.01}O$_800 has also been studied by applying a range of fields from 1 T down to 500 Oe. Independent of the applied field, the same behaviour is observed: the susceptibility of the samples decreases on increasing the temperature. In all cases, even at low applied field, the paramagnetic behaviour is predominant and no transition due to the ferromagnetic contribution is observed: it seems that the Curie temperature, T_C, for the $Zn_{0.99}Co_{0.01}O$ samples annealed at different temperatures always exceed 300 K. This result is in good agreement with some of the data reported in the literature for the

cobalt-doped ZnO[10-11,14,19-21,23]. Data for $Zn_{0.99}Co_{0.01}O$_800 taken at H = 1000 Oe are reported in figure 11, as an example.

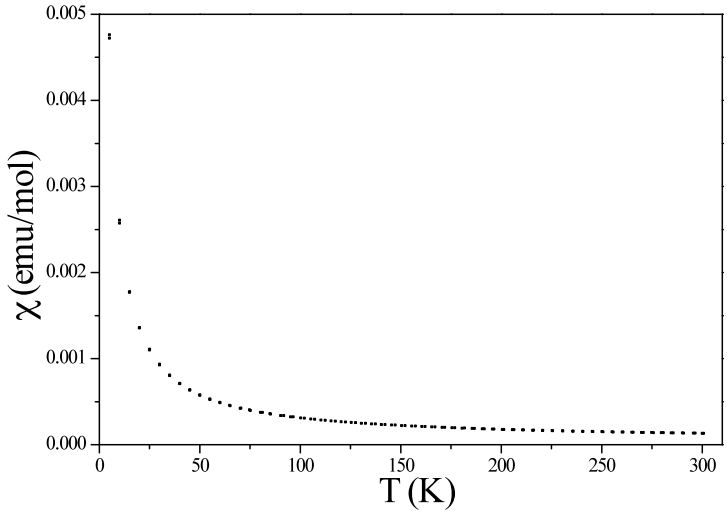

Figure 11: Plots of χ vs. T in $Zn_{0.99}Co_{0.01}O$_400 at H = 1000 Oe.

The results seem to confirm the presence of competing interactions between spins, where randomness in the sign of the exchange interaction gives rise to transitions between ordered and disordered magnetic phases, although further characterisations are still needed.

It is vital to not only corroborate the hypothesis that this model is truly applicable but also to understand the origin of such interactions between spins and how it would be possible to manipulate those interactions to modify the final properties of the material.

6.3.2 $Zn_{0.99}Mn_{0.01}O$

Results regarding $Zn_{0.99}Mn_{0.01}O$_400 are presented, in particular the field dependence of the magnetisation measured at a range of temperatures from 5 K up to room temperature.

Figure 12 shows the evolution of magnetisation (M) as a function of the applied field (H) at T = 5 K. The solid curve in figure 12 is a fit to a parameterised Brillouin function assuming for Mn^{2+}, S = 5/2 and g = 2. The g factor is taken from an EPR study reported in literature[59] for manganese ions dispersed in ZnO as Mn^{2+}_{Zn}.

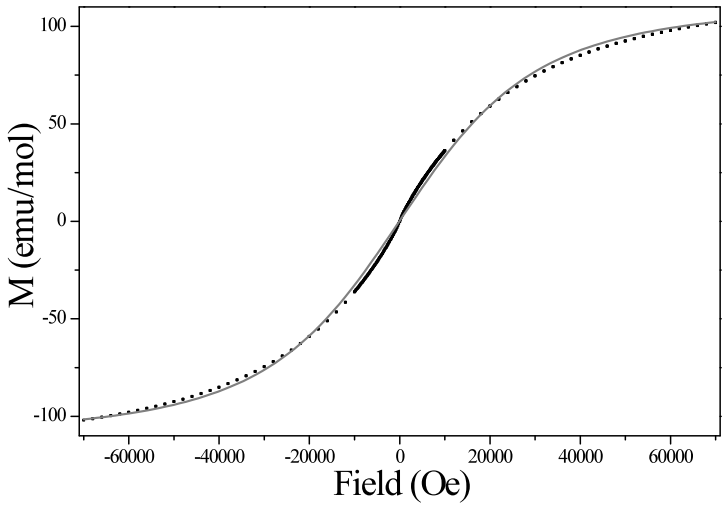

Figure 12: Plot of M vs. H at T = 5 K for $Zn_{0.99}Mn_{0.01}O$_400. Data are fitted with a Brillouin function.

$Zn_{0.99}Mn_{0.01}O$_400 at T = 5 K displays mostly paramagnetic behaviour and the Brillouin fitting gives rise to a manganese concentration that contributes to this magnetic phase of about 38% of the nominal content. Moreover, the M vs. H curve shows a small hysteresis contribution with the coercive field (Hc) of about 15 Oe, indicating the presence of a small ferromagnetic contribution. This contribution is so small that it is not possible to quantitatively discriminate it from the predominant paramagnetic behaviour, even though it can be noted in figure 13 that the fitting curve does not very well reproduce the behaviour at low field. As in the Co-doped system, to account for the nominal concentration of the dopant, it is necessary to take into consideration the presence of an antiferromagnetic coupling between spins.

Increasing the working temperature up to 300 K, all the observed M vs. H behaviours in the sample reveal that it is composed of a mixture of ferromagnetic and paramagnetic phases. Figure 13a reports the field scan of $Zn_{0.99}Mn_{0.01}O$_400 taken at T = 300 K, as an example.

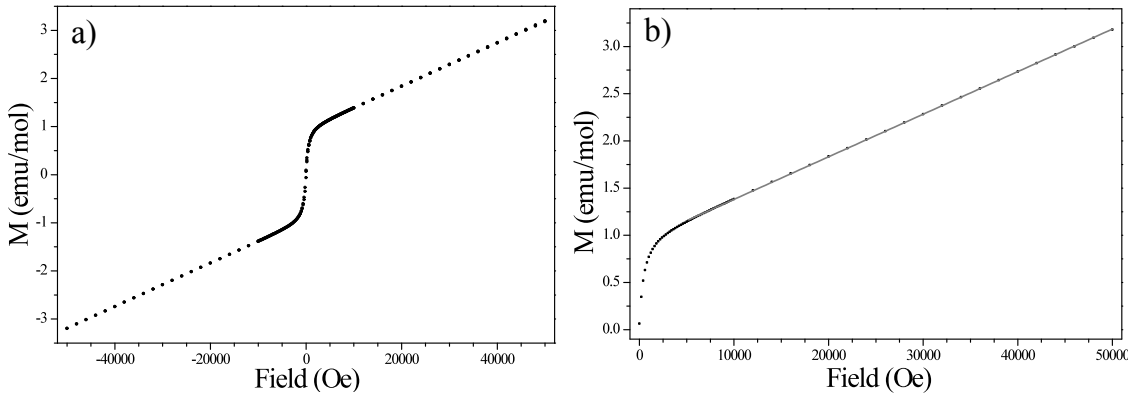

Figure 13: Plot of M vs. H at T = 300 K for $Zn_{0.99}Mn_{0.01}O$_400 **a)** complete scan **b)** fitting of experimental data using the equation reported in the text.

In analogy with the cobalt-doped system, experimental data are fitted taking into account the presence of the two contributions, both paramagnetic and ferromagnetic. Again, the antiferromagnetic phase will contribute, cancelling part of the net magnetisation. This type of fitting gives rise to the presence of a paramagnetic contribution of about 11% of the nominal manganese content and γ = 0.83 emu/mol. The coercive field (Hc) is about 40 Oe.

Figure 14 reports the variation of the paramagnetic and ferromagnetic contributions with changing temperature in $Zn_{0.99}Mn_{0.01}O$_400. All the fitting parameters obtained with changing temperature are listed in table 4.

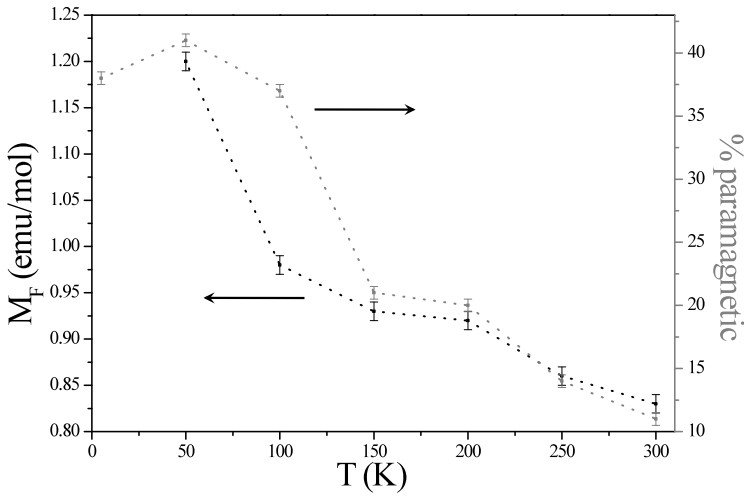

Figure 14: Graph which summarises the evolution of paramagnetic and ferromagnetic contributions as a function of the working temperature for sample $Zn_{0.99}Mn_{0.01}O$_400.

Table 4: Fitting parameters of data taken at different temperature for $Zn_{0.99}Mn_{0.01}O$_400.

T (K)	%para	γ (emu/mol)	H_C (Oe)
5	38.0±0.5	-	30±2
50	41.0±0.5	1.2±0.01	40±2
100	37.0±0.5	0.98±0.01	50±2
150	21.0±0.5	0.93±0.01	35±2
200	20.0±0.5	0.92±0.01	30±2
250	14.0±0.5	0.86±0.01	30±2
300	11.0±0.5	0.83±0.01	30±2

The coexistence of different contributions in manganese-doped ZnO is in good analogy with what has been reported in the previous section regarding cobalt-doped samples. However, in this case the temperature dependence of the magnetic properties is different: upon increasing the temperature both the paramagnetic volume fraction and the magnetisation from the ferromagnetic phase decrease. Further characterisations are needed to understand the origin of this magnetic behaviour in manganese-doped ZnO

and if the competing interaction model proposed for the cobalt-doped system is still be valid.

Finally, the temperature dependence of the susceptibility, χ, of $Zn_{0.99}Mn_{0.01}O$_400 has been studied applying different fields from 1 T down to 500 Oe. Independent of the applied field, the same behaviour is observed: the susceptibility of the samples decreases with increasing temperature. In all cases, even at low applied field, the paramagnetic behaviour is predominant and no transition due to the ferromagnetic contribution is observed. The Curie temperature, T_C, for the $Zn_{0.99}Mn_{0.01}O$_400 nanopowder exceeds 300 K which is in good agreement with some of the data in the literature[26-27,29-30]. Data taken at H = 500 Oe are reported in figure 15, as an example.

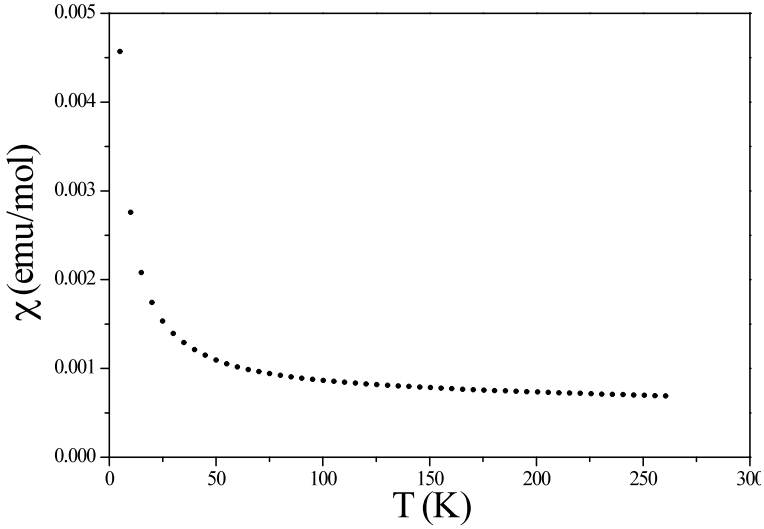

Figure 15: Plots of χ vs. T in $Zn_{0.99}Mn_{0.01}O$_400 at H = 500 Oe.

6.3.3 $Zn_{0.99}Cu_{0.01}O$

As mentioned before, among samples doped with copper, $Zn_{0.99}Cu_{0.01}O$_800 has been chosen to study the magnetic properties of the system. In fact, previous characterisations, and in particular *X-ray Absorption Spectroscopy*, have revealed that only high annealing temperatures cause the inclusion of the dopant inside the ZnO host.

Initially, the field dependence of the magnetization measured at different temperatures from 5 K to room temperature is presented. Figure 16 shows the evolution of magnetisation (M) as a function of the applied field (H) at T = 5 K. The solid curve in figure 16 is a fit to a parameterised Brillouin function assuming $S = 1/2$ and $g = 2.18$ for Cu^{2+}. The g factor is taken from experimental EPR data reported previously, in chapter 3.

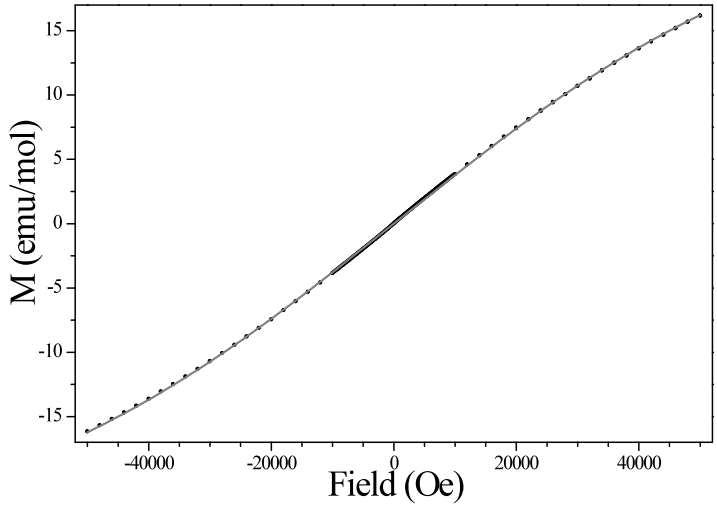

Figure 16: Plot of M vs. H at T = 5 K for $Zn_{0.99}Cu_{0.01}O$_800. Data are fitted with a Brillouin function.

$Zn_{0.99}Cu_{0.01}O$_800 at T = 5 K displays paramagnetic behaviour and the Brillouin fitting gives rise to a copper concentration that contributes to this magnetic phase of about 41.3% of the nominal content. However, the M vs. H curve shows a small hysteresis contribution with the coercive field (Hc) at about 30 Oe, indicating the presence of a small ferromagnetic phase volume. This contribution is so small that it is not possible to quantitatively discriminate it from the predominant paramagnetic behaviour. Finally, similarly to the systems doped with cobalt and manganese, the presence of an antiferromagnetic interaction, seems to be quite possible to account for the discrepancy from the nominal concentration of the dopant.

Upon increasing the working temperature, up to 50 K, the observed M vs. H behaviour in the sample reveals that it is composed of a mixture of ferromagnetic and paramagnetic phases, as shown in figure 17.

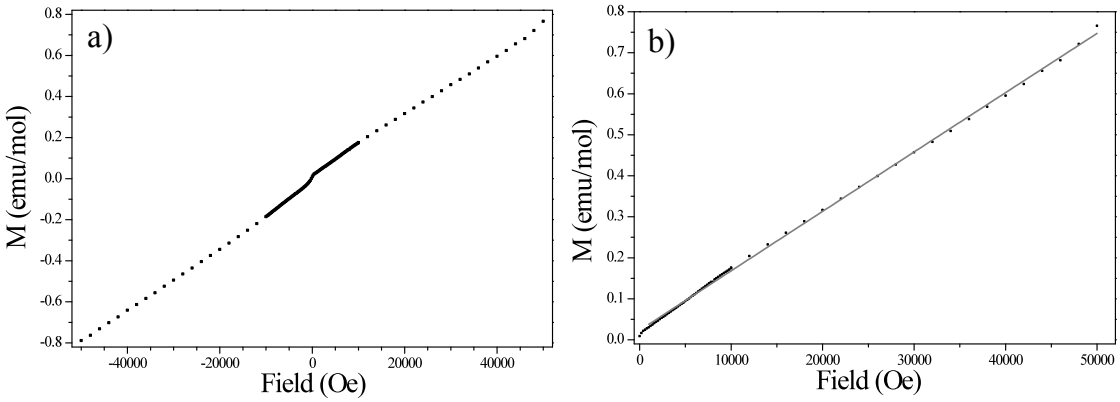

Figure 17: Plot of M vs. H at T = 50 K for $Zn_{0.99}Cu_{0.01}O$_800 **a)** complete scan **b)** fitting of experimental data using the equation reported in the text.

In analogy with the manganese and cobalt-doped systems, experimental data are fitted, taking into account the presence of the two contributions, paramagnetic and ferromagnetic. This type of fitting gives rise to the presence of a paramagnetic

contribution of about 16% of the nominal copper content and γ = 0.03 emu/mol. The coercive field (Hc) increases up to a value of about 200 Oe at 50 K.

A further increase in the working temperature, from 100 K to 300 K, completely alters the field dependence of the magnetisation. Figure 18 reports M vs. H behaviours of $Zn_{0.99}Cu_{0.01}O$_800 in this range of temperatures.

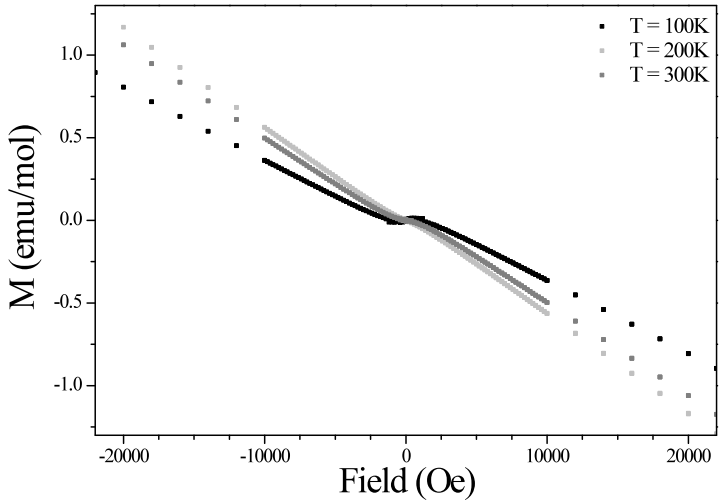

Figure 18: Plots of M vs. H for $Zn_{0.99}Cu_{0.01}O$_800 measured at different temperatures.

These results differ from those before: at these temperatures spins tend to align with each other but in opposite direction with respect to the applied field; this sample shows diamagnetic behaviour. Furthermore there is a sort of plateau at very low fields – i.e. in the range of 1000 Oe ≤ H ≤ 100 Oe – in which the external field seems to not influence the spins and where the net magnetisation is almost zero.

This behaviour is also confirmed by temperature dependence of the susceptibility χ, measured by applying fields from 1 T down to 500 Oe. Figure 19 shows data collected at H = 1 T and H = 500 Oe.

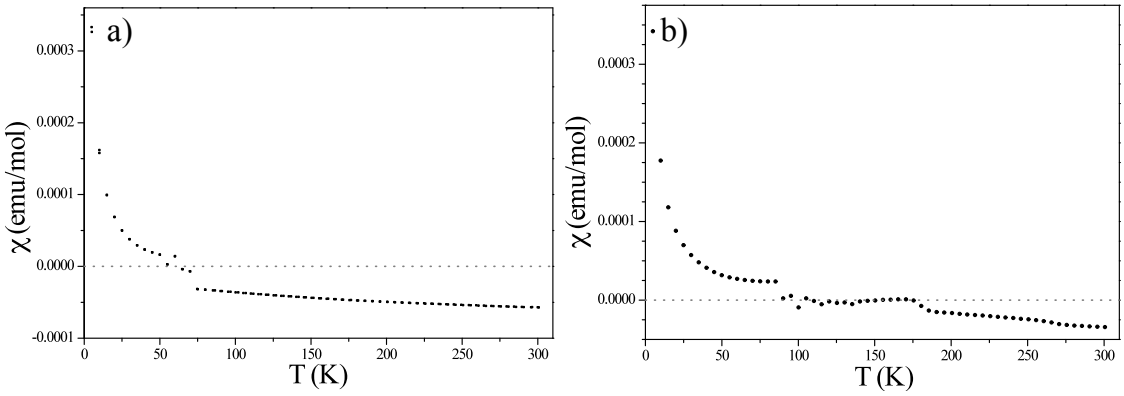

Figure 19: Plots of χ vs. T in $Zn_{0.99}Cu_{0.01}O$_800 **a)** at H = 1T and **b)** at H = 500 Oe.

In both cases, there is an inversion of the sign of the susceptibility, χ, which becomes negative at high temperature, indicating that the system becomes diamagnetic

above a certain temperature. At relatively high field, H = 1 T, this transition occurs between 50 K < T < 75 K in quite a narrow range; decreasing the field down to 500 Oe instead, there is a region, between roughly T = 75 K and T = 175 K, in which the susceptibility is almost zero, before changing sign and becoming negative.

Further characterisation is required to better understand the mechanism behind this behaviour which could give an exhaustive explanation of the experimental data.

6.4 Summary and Conclusion

Development of *Dilute Magnetic Semiconductor* materials (DMS) exhibiting ferromagnetic behaviour for diverse applications (i.e. spin-based light-emitting diodes, sensors or transistors) has aroused lively interest in the scientific community in the last few decades[1-8].

Recent theoretical calculations[1-3] have predicted that transition metal ion (TM) doped ZnO is one of the most promising candidates for room-temperature ferromagnetism. Conflicting theoretical and experimental results have been reported about the magnetic properties of transition metal ion (TM) doped ZnO, including spin-glass behaviour, paramagnetism, antiferromagnetism and ferromagnetism, preventing consensus on the existence and mechanism of intrinsic ferromagnetism.

For spintronic applications the dopant must be homogeneously distributed throughout the system for proper spin detection and manipulation. Many authors[1-41] suggest that the intrinsic ferromagnetism seen in TM doped ZnO systems is dependent on defects, in particular oxygen vacancies and Zn interstitials. The level and nature of the defects differs from one sample to another and depends on the method of preparation, making it difficult to reproduce. Consequently, when determining the magnetic properties of a system the presence of secondary phases must be carefully considered and characterised. Conventional material characterisation techniques do not have the sensitivity to detect trace amounts of secondary phase formation.

In this chapter, preliminary results have been presented on the magnetic properties of $Zn_{1-x}TM_xO$ (TM = Mn, Co, Cu). In particular, it is important to develop an understanding of the real nature of the magnetic interactions in such systems, of which there has been considerable debate in the scientific community. Taking into account that

the magnetisation of TM-doped ZnO is strongly dependent on the preparation parameters and any trace amount of external contamination could lead to a misinterpretation of experimental results only samples with low dopant content, $Zn_{0.99}TM_{0.01}O$, treated at different temperatures were examined here.

The field dependence of the magnetisation measured at temperatures ranging from 5 K up to room temperature (300 K) shows that $Zn_{0.99}Co_{0.01}O$ and $Zn_{0.99}Mn_{0.01}O$ nanoparticles yield different contributions: the coexistence of paramagnetic, ferromagnetic and antiferromagnetic phases are detected in all $Zn_{0.99}Co_{0.01}O$ samples as well as in $Zn_{0.99}Mn_{0.01}O$_400 nanopowders. The coexistence of different contributions in such a system has been reported previously[48]. The peculiarity of these systems is the temperature dependence of such interactions: in fact, by increasing the temperature it is possible to modify those interactions and in particular the fractions of spins in each magnetic phase.

To the best of our knowledge, this kind of behaviour for doped ZnO has never been reported before. One possible explanation could be the presence of competing interactions between spins, where randomness in the sign of the exchange interaction gives rise to transitions between ordered and disordered magnetic phases[49-58]. On changing the temperature it is possible to favour the presence of different magnetic states due to entropic factors.

In the case of the copper doped samples, the magnetic properties of $Zn_{0.99}Cu_{0.01}O$_800 have been investigated. The field dependence of the magnetisation measured at different temperatures shows some similarities with the previous cases: at low temperature, up to 50 K, the system presents the coexistence of paramagnetic, antiferromagnetic and ferromagnetic contribution. A further increase of the working temperature leads to an additional modification: the material undergoes a change in the magnetic behaviour aligning spins in opposite direction with respect to the applied fields.

Further characterisation will be needed to better understand the magnetic behaviour of transition metal ions doped zinc oxide, $Zn_{1-x}TM_xO$ (TM = Mn, Co, Cu): in particular, it will be important to confirm the presence of competing interactions between spins.

References:

[1] T. Dietl, H. Ohno, F. Matsukura, J. Cibert, D. Ferrand, *Science* **287** (2000) 1019

[2] G.A. Prinz *Science* **282** (1998) 1660

[3] H. Dery, P. Dalal, L. Cywinski, L. J. Sham, *Nature* **447** (2007) 573-576

[4] K. Ando, H. Saito, Z. Jin, T. Fukumura, M. Kawasaki, Y. Matsumoto, H. Koinuma, *J. Appl. Phys* **89** (11) (2001) 7284

[5] N. Lebedeva, P. Kuivalainen, *J. Appl. Phys.* **93** (12) (2003) 9845

[6] P. Kacman, *Semicond.Sci.Technol.***16** (2001) R25

[7] J.K. Furdyna, J.Appl.Phys. **64** (1988) R29

[8] S.A. Wolf, D.D. Awschalom, R.A. Buhrman, J.M. Daughton, S. von Molnár, M.L. Roukes, A.Y. Chtchelkanova, D.M. Treger, *Science* **294** (2001) 1488

[9] K. Sato, H. Katayama-Yoshida, *Jpn. J. Appl. Phys.* **39** (2000) L555

[10] I.J. Chen, Y.C. Ou, Z.Y. Wu, F.R. Chen, J.J. Kai, J.J. Lin, W.B. Jian, *J. Phys. Chem. C* **112** (2008) 9168

[11] K.P. Bhatti, S. Kundu, S. Chaudhary, S.C. Kashyap, D.K. Pandya, *J. Phys. D: Appl. Phys.* **39** (2006) 4909

[12] A.R. Han, S.J. Hwang, Y. Zhao, Y.U. Kwon, *J. Magn. Magn. Mater.* **320** (2008) 1591

[13] T.C. Kaspar, T. Droubay, Y. Li, S.M. Heald, P. Nachimuthu, C.M. Wang, V. Shutthanandan, C.A. Johnson, D.R. Gamelin, S.A. Chambers, *New J. Phys.* **10** (2008) 055010

[14] S. Deka, R. Pasricha, P.A. Joy, *Phys. Rev. B* **74** (2006) 033201

[15] T.C. Kaspar, T. Droubay, S.M. Heald, M.H. Engelhard, P. Nachimuthu, S.A. Chambers, *Phys. Rev. B* **77** (2008) 201303

[16] J.H. Park, M.G. Kim, H.M. Jang, S. Ryu, Y M. Kim, *Appl. Phys. Lett.* **84** (2004) 1338

[17] T. Dietl, T. Andrearczyk, A. Lipinska, M. Kiecana, M. Tay, Y.H. Wu, *Phys. Rev. B* **76** (2007) 155312

[18] M.A. White, S.T. Ochsenbein, D.R. Gamelin, *Chem. Mater.* **20** (2008) 7107

[19] C. Song, K.W. Geng, F. Zeng, X.B. Wang, Y.X. Shen, F. Pan, Y.N. Xie, T. Liu, H.T. Zhou, Z. Fan, *Phys. Rev.* B **73** (2006) 024405

[20] M. Venkatesan, C.B. Fitzgerald, J.G. Lunney, J.M.D. Coey, *Phys. Rev. Lett.* **93** (2004) 177206

[21] P. Sati, R. Hayn, R. Kuzian, S. Regnier, S. Schafer, A. Stepanov, C. Morhain, C. Deparis, M. Laugt, M. Goiran, Z. Golacki, *Phys. Rev. Lett.* **96** (2006) 017203

[22] T. Yao, W. Yan, Z. Sun, Z. Pan, Y. Xie, Y. Jiang, J. Ye, F. Hu, S. Wei*, J. Phys. Chem C* **113** (2009) 14114

[23] J.M.D. Coey, M. Venkatesan, C.B. Fitzgerald, *Nature Mater.* **4** (2005) 173

[24] A. Tiwari, C. Jin, A. Kvit, D. Kumar, J.F. Muth, J. Narayan, *Solid State Commun*. **121** (2002) 371

[25] S.W. Jung, S.J. An, G. Yi, C.U. Jung, S. Lee, S. Cho, *Appl. Phys. Lett.* **80** (2002) 4561

[26] P. Sharma, A. Gupta, K.V. Rao, F.J. Owens, R. Sharma, R. Ahuja, J.M.O. Guillen, B. Johansson, G.A. Gehring, *Nat. Mater.* **2** (2003) 673

[27] X. Wei, Y. Zhou, X. Zhan, D. Chen, Y. Xie, T. Liu, W. Yan, S. Wei, *Solid State Commun.* **141** (2007) 374

[28] N.R.S. Farley, K.W. Edmonds, A.A. Freeman, G. van der Laan, C.R. Staddon, D.H. Gregory, B.L. Gallagher, *New J. Phys.* **10** (2008) 055012

[29] S.W. Yoon, S.B. Cho, S.C. We, S. Yoon, B.J. Suh, H.K. Song, Y.J. Shin, *J. Appl. Phys.* **93** (10) (2002) 7879

[30] M. Venkatesan, C.B. Fitzgerald, J.G. Lunney, J.M.D. Coey, *Phys Rev. Lett.* **97** (17) (2004) 177206

[31] K. Ando, H. Saito, Z. Jin, T. Fukumura, M. Kawaski, Y. Matsumoto, H. Koimura, *J. Appl. Phys.* **89** (2001) 7284

[32] H.J. Lee, B.S. Kim, C.R. Cho, S.Y. Jeong, *Phys Status Solidi B* **241** (2004) 1533

[33] D.B. Buchholz, R.P.H. Chang, J.H. Song, J.B. Kettersin, *Appl. Phys Lett.* **87** (2005) 082504

[34] D. Chakraborti, J. Narayan, J.T. Prater, *Appl. Phys Lett* **90** (2007) 062504

[35] X. Wang, J.B. Xu, Y. Cheung, J. An, K. Ne, *Appl. Phys Lett* **90** (2007) 212502

[36] M.S. Seehra, P. Dutta, V. Singh, Y. Zhang, I. Wender *J. Appl. Phys.* **101** (2007) 09H107

[37] A. Tiwari, M. Snure, D. Kamur, J.T. Abiade, *Appl. Phys Lett.* **92** (2008) 062509

[38] C. Sudakar, K. Padmanabhan, R. Kaik, G. Lawers, B.J. Kriby, S. Kamur, V.M. Naik, *Appl. Phys Lett.* **93** (2008) 042502

[39] D.J. Keavney, D.B. Buchholz, Q. Ma, R.P.H Chang. *Appl. Phys Lett* **91** (2007) 012501

[40] Q. Xu, H. Schmidt, S. Zhou, K. Potzger, M. Helm, H. Hochmuth, M. Lorenz, A. Setzer, P. Esquinazi, C. Meinecke, M. Grundmann, *Appl. Phys Lett.* **92** (2008) 082508

[41] M. Ferhat, A. Zaoui, R. Ahuja, *Appl. Phys Lett.* **94** (2009) 142502

[42] John Clarke, Alex I. Braginski, *The SQUID Handbook,* Ed. *WILEY-VCH Verlag GmbH & Co. KGaA, Weinheim* (2006)

[43] P. Atkins, J. De Paula, *Atkins' Physical Chemistry*, 8th Ed. Oxford University Press (2006)

[44] C. Kittel, *Introduction to Solid State Physics 7th ed.,* John Wiley and Sons, Inc., New York, Chichester, Brisbane, Toronto, Singapore (1996)

[45] J.M.D. Coey, *Magnetism and magnetic materials*, Cambridge University Press, Cambridge, (2010)

[46] T.L. Estle, M. de Wit, *Bull. Am. Phys. Soc*. **6** (1961) 445

[47] L. El Mir, Z.B. Ayadi, H. Rahmouni, J. El Ghoul, K. Djessas, H.J. von Bardeleben, *Thin Solid Films* **517** (2009) 6007

[48] K.P. Bhatti, S. Kundu, S. Chaudhary, S.C. Kashyap, D.K. Pandya, *J. Phys. D: Appl. Phys.* **39** (2006) 4909

[49] G.J. Nieuwenhuys, B.H. Verbeek, J.A. Mydosh, *J. Appl. Phys.* **50** (1979) 1685

[50] H. Maletta, *J. Appl. Phys.* **53** (1982) 2185

[51] H. Maletta, W. Felsch, *Z. Phys. B* **37** (1980) 55

[52] H. Maletta, G. Aeplli, S.M. Shapiro, *Phys. Rev. Lett.* **48** (1982) 1490

[53] Y. Yeshurun, M.B. Salamon, K.V. Rao, H.S. Chen, *Phys. Rev. B* **24** (1981) 1536

[54] J.A. Geohegan, S.M. Bhagat, *J. Magn. Magn. Mat.* **25** (1981) 17

[55] G. Aeppli, S.M. Shapiro, R.J. Birgeneau, H.S. Chen, *Phys. Rev. Lett. B* **25** (1982) 4882

[56] S.M. Shapiro, C.R. Fincher, A.C. Palumbo, R.D. Parks, *Phys. Rev. B* **24** (1981) 6661

[57] S.K. Burke, R. Cywinski, J.R. Davis, B.D. Rainford, *J. Phys. F* **13** (1983) 441

[58] G. Aeppli, S.M. Shapiro, R.J. Birgeneau, H.S. Chen, *Phys. Rev. B* **28** (9) (1983) 5160

[59] A. Hausmann, H. Huppertz, *J. Phys. Chem. Solids* **29** (1968) 1369

Chapter 7
Conclusion

7.1 Summary

The key requirements for the development of new functional devices not only include the ability to tailor the physical properties of nano-materials but also, and in particular, the knowledge required to allow an *a priori design* of new materials with predictable properties and improved performances.

In spite of many decades of investigation some of the basic properties of ZnO still remain unclear and there are at least three fields in which scientific debate is particularly lively. In particular there is still no consent about how to enhance the catalytic properties, induce specific magnetic properties or change the optical emission properties of this kind of material through modification of their chemical composition, structure and morphology.

This thesis is focused on the synthesis and characterisation of nanostructures based on ZnO doped with transition metal ions ($Zn_{1-x}TM_xO$, TM = Mn, Co, Cu) with specific interest toward catalytic, optical and magnetic properties and related applications. *Sol gel* synthesis is a method in which the parameters involved are numerous and, if properly controlled, can actually help to obtain materials with desirable characteristics in terms of composition, structure and morphology. Doping with transition metal ions, such as manganese, cobalt and copper, also offers an effective method to adjust the electrical, magnetic, and optical properties of zinc oxide. In order to understand the structure-property relationships a detailed characterisation of the materials was performed with complementary techniques such as *X-ray Diffraction* (XRD), *Scanning*

Electron Microscopy (SEM), *X-ray Photoelectron Spectroscopy* (XPS), UV-Vis Spectroscopy, *X-ray Absorption Spectroscopy* (XAS) and *Electron Paramagnetic Resonance* (EPR).

The annealing conditions have been found (chapter 2) to be a key parameter in controlling the microstructure and the dimensions of the final particles: nanocrystallites with an average size of a few tens of nanometers (20 nm) are obtained at 400°C while at 800°C the average size increases up to ~ 100 nm; the average particle size of samples annealed at 600°C, an intermediate temperature, is roughly 50 nm. Furthermore, the annealing temperature is also capable of influencing the ratio between lattice oxygen and hydroxyl groups of the nanoparticles. Both these effects seem to remain unaffected by the presence of the transition metal ion dopant used. Wet chemical synthesis, such as *Sol gel*, is expected to provide good control over chemical homogeneity and morphology at an atomic level. This seems to be confirmed by the conventional characterisation described in chapter 2: in $Zn_{1-x}TM_xO$ nanopowders with low dopant content the transition metal ions seem to be dispersed in the ZnO matrix occupying substitutional Zn sites, while on increasing the dopant concentration the formation and segregation of secondary phases is detected.

Investigations of the local environment of these nanoparticles through *X-ray Absorption Spectroscopy* (chapter 3) have allowed greater understanding and interpretation of the structure of the $Zn_{1-x}TM_xO$ materials. Results have clearly shown that both low dopant concentration and low processing temperature are essential if secondary phase formation is to be avoided. Furthermore, XAS has proven to be a powerful tool as it is highly sensitive to secondary phase formation and can provide quantitative information as to the amount of secondary phase formed.

In chapter 4, the catalytic performance of undoped ZnO and $Zn_{1-x}Cu_xO$ systems tested with respect to the *Methanol Steam Reforming* reaction were reported. Contrary to what is generally accepted in literature, the results obtained in this study demonstrate that ZnO also plays a prominent role in steam reforming of methanol: ZnO calcined at 400°C shows unexpected catalytic activity with a very good selectivity as the only products detected in the effluent gas are H_2 and CO_2. This activity can be traced back to the presence of defects in the ZnO semiconductor, more precisely oxygen vacancies and shallow donors (EPR results, shown in chapter 3) which act as active sites. The introduction of copper enhances the catalytic performance; however, in contrast with the case of undoped zinc oxide, catalysts containing copper enable the evolution of by-

products. The loss of selectivity, in both cases, is not significant and only traces of by-products are detected with FTIR spectroscopy. The structure–activity relationships of ZnO and copper-doped ZnO catalysts described in this work and the possibility to tailor the "real structure" of a catalyst during preparation are a step towards a rational design of improved catalysts.

In chapter 5 the luminescence properties of the different doped $Zn_{1-x}TM_xO$ nanopowders were reported. *X-ray Excited Optical Luminescence* (XEOL) is a suitable method to study phenomenological optoelectronic and structural correlations: a general trend could be extrapolated from these results. Annealing of ZnO and $Zn_{1-x}TM_xO$ nanoparticles enhances their luminescence due to the removal of vacancies and lattice defects inside the nanoparticles which trap electrons in defect levels and subsequently undergo non-radiative de-excitation. Second phase formation should be avoided to preserve the luminescent properties of $Zn_{1-x}TM_xO$ nanoparticles: independent of the dopant, segregation is always accompanied with a quenching in the emission spectra. Finally, the nature of the transition metal ion could also affect the luminescence of ZnO growth by *sol-gel*. New localized defect levels are introduced in the band-gap of the semiconductor: the energy and the nature of these levels can be tuned by changing the dopant. It is worth highlighting the case of $Zn_{1-x}Co_xO$, where the presence of cobalt leads to drastic modifications in the emission spectra of the system: all samples showed an intense, narrow peak centred in the red zone of the visible spectrum; the absorbed photon energy is transferred from the ZnO host to the cobalt which undergoes radiative recombination to produce the intense emission at ~687 nm (assigned to the transition between $^2E \rightarrow {}^4A_2$ states of Co^{2+}in a tetrahedral coordination).

Finally, in chapter 6, preliminary results have been presented on the magnetic properties of $Zn_{1-x}TM_xO$ (TM = Mn, Co, Cu): the coexistence of different contributions has been detected. The unusual feature of these systems is the temperature dependence of such interactions: on increasing the temperature it is possible to modify these interactions and in particular the fractions of spins in each magnetic phase. To the best of our knowledge, this kind of behaviour for doped ZnO has never been reported before. Further characterisation will be needed to better understand the magnetic behaviour of transition metal doped zinc oxide, $Zn_{1-x}TM_xO$ (TM = Mn, Co, Cu): in particular to confirm the presence of competing interactions between spins. One of the most important goals of this project is to determine the nature of the magnetic interactions in such systems, of which there has been considerable debate in the scientific community.

7.2 Outlook

This thesis represents a contribution towards answering some of the questions that have brought about a lively debate in the scientific community about several interesting properties of ZnO based materials. Of course to attempt to clarify every dispute involving this system is beyond the scope of this thesis. Some of the ideas for future work based on the studies undertaken in this thesis are described below.

First, the *Sol gel* synthesis technique that has been developed could, in principle, be easily extended to doping with other transition metal ions, such as chromium or iron, to name a few, or to other lanthanides. This would provide a larger base of knowledge to allow further tailoring of the properties of ZnO-based semiconducting materials.

Furthermore, it would be interesting to change the heat treatment conditions to anneal samples in a controlled atmosphere – i.e. an inert environment using N_2 or reducing conditions using 5% H_2 balance Ar – in order to increase the number of oxygen vacancies and prevent the further oxidation of the dopants.

The development of an applied technology based on the exploitation of catalytic, optical or magnetic properties is related to the possibility of creating functional devices. For this reason, another interesting perspective would be to prepare other types of nanostructures such as thin-films. *Sol gel* synthesis is a very versatile technique and it should be relatively easy to grow the ZnO based materials as thin layers.

Of course further characterisation will be needed, especially with regards to the optical and magnetic properties. For example, additional tests such as time-resolved XEOL will give the opportunity to better ascribe the nature of the emissions and to give an in-depth picture of the energy transfer pathways to the optical channels. To fully understand the nature of magnetic interaction in TM-doped ZnO, complementary techniques, such as *X-ray Magnetic Circular Dichroism* (XMCD) spectroscopy could be used.

Finally, catalytic tests would be extended to other doped systems to investigate the possibility to develop new materials for the conversion of methanol into hydrogen in a sustainable manner.